

***In-vivo* Digital Volume Correlation  
via Magnetic Resonance Imaging:  
Application to Positional Brain Shift  
and Deep Tissue Injury**

**A thesis submitted in partial fulfilment  
of the requirement for the degree of Doctor of Philosophy**

**Stefano Zappalá**

**July 2022**

**Cardiff University  
School of Computer Science & Informatics  
School of Psychology**



**A mia madre.  
La mia roccia, la mia maestra di vita.**

## Abstract

This thesis aims to investigate the complexity of the physiological mechanical response of soft tissues, providing rich datasets for the verification of clinical systems limiting or preventing tissue injury. A thorough understanding of the sagging of the brain tissue under the effect of gravity (positional brain shift, PBS) is paramount for the design of an effective intra-operative correction of surgical trajectories; rich measurements of the response of the buttock to sitting loads can help the verification of computational models to couple with clinical measures for the prevention and control of pressure ulcers.

Digital volume correlation (DVC) consists in measuring the local differences between scans depicting the deformed and undeformed stages of a sample under load, facilitating the characterisation of the mechanical response of the sample. The use of DVC *in-vivo* is limited, due to the limited quality of the scans constrained by the acquisition setting.

Accuracy of three deformable registration methods was first assessed after optimisation against biomechanically plausible ground truths generated via finite element simulations. Against the simulation of PBS, the best accuracy achieved was of one order of magnitude smaller than the resolution of the images. For the simulation of deformations of the buttock due to sitting, optimal accuracy was around 10% of the average deformation fields applied.

The best performing methods alongside their optimal parameter sets were then used to perform *in-vivo* measurements on real magnetic resonance scans of two separate datasets of healthy subjects. For PBS, the study revealed the need for intervention- and

patient-specific correction of surgical trajectories given the effect of head geometry and orientation on the shift. For the deformation of the buttock due to sitting, the measurements gave a three-dimensional depiction of the local and global pattern of deformation, which results were previously limited to thickness or surface measurements.

## Acknowledgements

First and foremost, I would like to express my thanks to Prof. David Marshall, for his constant guidance and excellent supervision. I would like to extend these thanks also to Prof. Sam Evans, Prof. Derek Jones, Dr. Jing Wu and Dr. Bethany Keenan, for their support throughout the PhD project as well as for the valuable feedbacks. A special thanks to my brainshift companions, Dr. Nick and Dr. Matt, for being excellent colleagues, always looking for a new idiom to teach me. To all my upstairs colleagues from COMSC, thank you for all the long lunches and the unnecessary tea breaks in the common room.

A huge thanks to the staff at Cardiff University Brain Imaging Centre (CUBRIC), for giving me the opportunity to get to know and operate MR scanners. A special thanks to Ian Driver, for his constant help from the very beginning of the project until the end; to John Evans and Peter Hobden, for their supervision and to Slawek Kusmia for his support during the thick of the scanning. A thanks to Rob Harrison, Paul Skinner and Renishaw plc, for the financial support and industrial guidance.

A huge thanks to my mecenati, Roberto and the superior twin, Emma, who ultimately enabled me to complete this work with a piece of mind. These years spent in the cottage will be truly unforgettable. Thanks also to the lords of the rings, always ready for a celebratory ice-cream after a lightweight session. To my teammate, Lauren, you're welcome for me being such a great support to you throughout my PhD. Truth aside, thanks for all the silly dances in the kitchen and the over-abundance of Gs in my belly.

Concludo con un ringraziamento di cuore a tutta la mia famiglia, per il loro continuo sostegno e per le perplessità a riguardo di quando e come finisce il dottorato di Stefano. A mamma Cristina prima di tutto, a cui dedico questa tesi: mi hai mostrato come essere un adulto, senza mai dimenticare di apprezzare momenti semplici e felici. Un grazie di cuore a mia sorella Paola, per fare sempre del suo meglio per farmi sentire a casa ogni volta che torno per le vacanze. A Ele e Marco, per le domande specifiche e a bruciapelo, tipiche di un interrogatorio Prandini. Nessun ringraziamento per i quattro nipotini, Lorenzo, Francesco, Vittoria e Zeno, per essere cresciuti troppo velocemente: vi ho lasciati da bambini e vi ritrovo ora da ragazzini.

# Contents

<b>Abstract</b>	<b>iii</b>
<b>Acknowledgements</b>	<b>v</b>
<b>Contents</b>	<b>vii</b>
<b>List of Figures</b>	<b>x</b>
<b>List of Tables</b>	<b>xxi</b>
<b>Acronyms</b>	<b>xxiii</b>
<b>1 Introduction</b>	<b>1</b>
1.1 Overview . . . . .	1
1.2 Hypothesis and Research Questions . . . . .	5
1.3 Thesis Structure and Contributions . . . . .	6
<b>2 Literature Review</b>	<b>11</b>
2.1 Overview . . . . .	11



---

2.2	Image Registration . . . . .	12
2.3	Digital Volume Correlation . . . . .	23
2.4	Medical Image Registration . . . . .	29
2.5	Sensitivity Analysis . . . . .	37
2.6	MR Distortions . . . . .	40
2.7	Summary . . . . .	42
<b>3</b>	<b>Brain Shift: Parametric Identification and Error Analysis</b>	<b>43</b>
3.1	Introduction to Brain Shift . . . . .	44
3.2	MR Distortions . . . . .	48
3.3	Skull Alignment . . . . .	51
3.4	Deformable Registration: Optimisation . . . . .	55
<b>4</b>	<b>Brain Shift: Digital Volume Correlation</b>	<b>68</b>
4.1	Introduction . . . . .	69
4.2	Study Definition and Ethics . . . . .	71
4.3	Methods . . . . .	75
4.4	Results . . . . .	79
4.5	Discussion . . . . .	86
4.6	Data Availability . . . . .	91
<b>5</b>	<b>Deep Tissue Injury: Parametric Identification and Error Analysis</b>	<b>93</b>
5.1	Introduction to Deep Tissue Injury . . . . .	94
5.2	Pelvis Alignment: Optimisation . . . . .	95

---

5.3	Deformable Registration: Optimisation . . . . .	102
<b>6</b>	<b>Deep Tissue Injury: Digital Volume Correlation</b>	<b>120</b>
6.1	Introduction . . . . .	121
6.2	Methods . . . . .	122
6.2.1	MR Dataset . . . . .	122
6.2.2	DVC Measurements . . . . .	123
6.3	Results . . . . .	125
6.4	Discussion . . . . .	129
6.5	Data Availability . . . . .	133
<b>7</b>	<b>Conclusions and Future Work</b>	<b>135</b>
7.1	Research Questions and Contributions . . . . .	135
7.2	Future Work . . . . .	141
7.3	Final Remarks . . . . .	145
	<b>Bibliography</b>	<b>146</b>

---

## List of Figures

2.1	Depiction of the difference between a global (middle) and a deformable (right) registration problem. . . . .	17
2.2	Depiction of the components of an affine transformation: translation, rotation, scale and skew. . . . .	17
3.1	Example of an IGNS software: interface of Renishaw <i>neuroinspire</i> <sup>TM</sup> designed for the planning of most stereotactic neurosurgical procedures. . . . .	45
3.2	Average and intra-region variability of the magnitude of the warp field representing differences between scans from different scanners due to MR distortions. . . . .	50
3.3	Boxplot of the Dice coefficient and the Hausdorff distance representing the alignment of skulls after affine registration with the three algorithms tested (FLIRT, ANTs and <i>elastix</i> ). . . . .	54
3.4	Axial and sagittal views of the synthetic displacement field used for the evaluation of the accuracy of the measurements. . . . .	56
3.5	Boxplots of the mean norm error for each method (DRAMMS, SyN and <i>elastix</i> ) at superficial and deep brain areas. . . . .	59

- 
- 3.6 DRAMMS: heatmap of the individual and joint sensitivity on the error metric (MNE). On the left, results at superficial ROI (including meninges, GM and WM) and deep ROI (including ventricles, STN and Putamen). Values are percentages relative to the mean total variances. 60
- 3.7 DRAMMS: surface plots showing the pair-wise distribution of the error metric (MNE, in [mm]) between the three most influencing parameters. Red dots represent query points. . . . . 60
- 3.8 DRAMMS: histogram of the number of registration calls leading to MNE values below its 5<sup>th</sup>-percentile. Histograms are reported for the three most influencing parameters; in blue at superficial ROI (including meninges, GM and WM) and in orange at deep ROI (including Ventricles, STN and putamen). . . . . 61
- 3.9 SyN: heatmap of the individual and joint sensitivity on the error metric (MNE). On the left, results at superficial ROI (including meninges, GM and WM) and deep ROI (including ventricles, STN and Putamen). Values are percentages relative to the mean total variances ( $7.54401 \cdot 10^{-6} \text{ mm}^2$ ) on superficial whereas  $4.11782 \cdot 10^{-5} \text{ mm}^2$  on deep ROI). 62
- 3.10 SyN: surface plots showing the pair-wise distribution of the error metric (MNE, in [mm]) between the three most influencing parameters. Red dots represent query points. . . . . 62
- 3.11 SyN: histogram of the number of registration calls leading to MNE values below its 5<sup>th</sup>-percentile. Histograms are reported for the three most influencing parameters; in blue at superficial ROI (including meninges, GM and WM) and in orange at deep ROI (including Ventricles, STN and putamen). . . . . 63

- 3.12 *elastix*: heatmap of the individual and joint sensitivity on the error metric (MNE). On the left, results at superficial ROI (including meninges, GM and WM) and deep ROI (including ventricles, STN and Putamen). Values are percentages relative to the mean total variances ( $0.0106621 \text{ mm}^2$  for superficial and  $0.0461161 \text{ mm}^2$  for deep ROI). . . . . 64
- 3.13 *elastix*: surface plots showing the pair-wise distribution of the error metric (MNE, in [mm]) between the three most influencing parameters. Red dots represent query points. . . . . 64
- 3.14 *elastix*: histogram of the number of registration calls leading to MNE values below its 5<sup>th</sup>-percentile. Histograms are reported for the three most influencing parameters; in blue at superficial ROI (including meninges, GM and WM) and in orange at deep ROI (including Ventricles, STN and putamen). . . . . 65
- 3.15 Distribution of the MNE for the best registration call for each method tested (that is, SyN on the left, DRAMMS in the centre and *elastix* on the right). Values are extracted over the brain area for one subject. Colour bar represents values in [mm]. . . . . 65
- 4.1 Poster used for the recruitment targeting participants in the age range 50 to 70 years of age, as individuals in the 20-30 years age range could be easily found in the academic setting. . . . . 73
- 4.2 Schematic of the acquisition protocol for the study carried out in the 3T scanner. Duration of each acquisition sequence is reported below for prone scanning, on the left; and for supine scanning (right), after switching participant position. . . . . 74

- 
- 4.3 Polar histograms of the direction of gravity (i.e., head orientation of participants) during scanning. On the left, greater values of azimuth angle represent head of the participant turned right during scanning. On the right, higher values of elevation angle represent head of the participant tilted downwards during scanning. The shape of the skull from the MNI atlas is overlapped as reference for the neutral head orientation. . . . . 79
- 4.4 Axial views of the initial alignment of the pelvic elements between supine (blue), prone (orange) scans. . . . . 80
- 4.5 Vector plots of PBS for two axial (*a* and *b*) and two sagittal (*c* and *d*) slices. Length of vectors have been scaled for visualisation purposes: their magnitude is represented by the underlying contour plots. As reference, dashed coloured lines represent the position of the other slices. In particular, slice *a* was positioned at the level of the anterior and posterior horns of the lateral ventricles, whereas slice *c* was positioned at the level of the falx cerebri. . . . . 81
- 4.6 Polar diagrams showing azimuth (left) and elevation (centre) angles as well as magnitude (right) of PBS averaged over some ROI: left (L) and right (R) gray matter (GM), white matter (WM), ventricles (Vent), thalamus (T), caudate (Cad), putamen (Put), pallidus (Pall), subthalamic nucleus (STN), red nucleus (RN), substantia nigra (SN) and brain-stem (BStem). Whiskers represent inter-subject variability. Decreasing values of azimuth angle in the  $[-90, -180]^\circ$  range represent vectors progressively oriented towards left, whereas increasing values of elevation angle in the  $[90, 270]^\circ$  range represent vectors progressively oriented downwards. STN, RN and SN were combined together due to the small number of voxels represented by these structures. . . . . 82

- 4.7 Distribution of the hydrostatic component at two axial ( $a$  and  $b$ ) and two sagittal ( $c$  and  $d$ ) slices. As reference, three ROI (Vent, STN, BStem) are delineated. Dashed coloured lines represent the position of the other slices. In particular, slice  $a$  was positioned at the level of the anterior and posterior horns of the lateral ventricles, whereas slice  $c$  was positioned at the level of the falx cerebri. . . . . 83
- 4.8 Distribution of the main deviatoric components of the Green-Lagrange strain. First row shows axial ( $a$ ) and sagittal ( $b$ ) slices of the L-R component; second row shows the P-A component ( $c$  and  $d$ ); third the I-S component ( $e$  and  $f$ ). As reference, three ROI (Vent, STN, BStem) are delineated. Dashed coloured lines represent the position of the other slices. Axial slices were positioned at the level of the anterior and posterior horns of the lateral ventricles, whereas sagittal slices were positioned 1 cm to the right of the falx cerebri. . . . . 84
- 4.9 Diagonal components of strain averaged over some ROI: left (L) and right (R) anterior and posterior meninges (Men Ant, Men Post), frontal lobe (Front), temporal lobe (Temp), ventricles (Vent), parietal lobe (Par), occipital lobe (Occ). Blue lines represent the overall diagonal component (whiskers representing inter-subject variability), whereas the orange and yellow lines its deviatoric and volumetric components. 85
- 4.10 Scatter plots of the correlation between PBS and MCB. Azimuth (blue dots) and elevation (orange squares) angles are reported on the left against values of MCB, whereas against magnitude of PBS on the right. As reference, linear fit is superimposed to the data. . . . . 85

- 4.11 Scatter plots of the correlation between PBS and gravity ( $\bar{g}$ ). Elevation angle of gravity is here reported against elevation angle (left) and against magnitude of PBS (right) for both prone (blue dots) and supine (orange squares) positioning. As reference, linear fit is superimposed to the data in the case of the statistical correlation between elevation angle of  $\bar{g}$  in supine and both elevation angle (on the left) and magnitude (on the right) of PBS. . . . . 86
- 5.1 Boxplots showing the extracted values of the DC (right) and the HD (left) for each method. Values of DC are evaluated over the whole pelvic area segmented; HD values, instead, are evaluated only at the IT and GT. Annotated values display the best performance for each method, that is, maximum DC and minimum HD values. Top, centre and bottom rows show results for the 3 subjects (sbj) analysed. As reference, diamond markers show the performance of each model with default parameters (if successful). . . . . 99
- 5.2 Sensitivity analysis on the initial registration: heatmap of the individual and joint sensitivity of the error metrics on the parameters trialled for *elastix*. On the left, percentages relative to the mean total variance of the DC (that is, 0.00271051), whereas on the right of the HD (that is, 13.7047 mm<sup>2</sup>). . . . . 100
- 5.3 Optimisation of the initial registration: surface plots of the DC (top row) and HD (bottom row, in [mm]) for the three most influencing parameters of the *elastix* method. Yellow dots represent the query points. Best performance is represented with lighter colours, that is, higher values of DC and lower values of HD. Similarity measures tested were SSD (number 1 in the plot), MI (number 2 in the plot) and CC (number 3 in the plot). . . . . 101



- 5.4 Simplified FE model of the buttock. On the left, the position of the segmented area is reported over the acquired field of vision. On the right, axial view of the generated mesh. Fat tissue is here depicted in orange, whereas muscle in yellow. For reference, nomenclature for anatomical locations used in the present study is reported on the mesh: Deep Medial Muscle, Deep Lateral Muscle, Superficial Lateral Muscle, Superficial Medial Muscle, Lateral Fat, Medial Fat . . . . . 104
- 5.5 Axial views of the generated ground truths: on the left, vector field given by a fixed displacement of 10 mm (azimuth angle of  $43.25 \pm 21.77^\circ$ , elevation angle of  $-0.77 \pm 1.53^\circ$  and magnitude of  $7.30 \pm 3.15$  mm), whereas given by a fixed displacement of 30 mm on the right (azimuth angle of  $45.07 \pm 25.44^\circ$ , elevation angle of  $0.26 \pm 1.02^\circ$  and magnitude of  $19.37 \pm 9.58$  mm). Lengths of vectors have been scaled for visualisation purposes: their magnitude is represented by the underlying contour plots. 104
- 5.6 Boxplots showing the distribution of MNE values on the left for the 10 mm results, on the right for the 30 mm results. Boxplots are reported for each method: that is, DRAMMS, SyN and *elastix*. Annotated values display the best performance, that is, the minimum MNE value. Top row show results in the muscle area, whereas for the muscle areas at the bottom. For reference, diamonds indicate the performance of the methods with their specific default parameters. . . . . 107
- 5.7 DRAMMS: heatmap of the individual and joint sensitivity on the error metric (MNE). On the left, percentages relative to the total variance in the 10 mm simulation, whereas on the right for the 30 mm simulation ( $0.992304 \text{ mm}^2$  for the 10 mm simulation, and  $15.5281 \text{ mm}^2$  for the 30 mm one). . . . . 108

- 5.8 DRAMMS: surface plots showing the pair-wise distribution of the error metric (MNE, in [mm]) between the three most influencing parameters. On the top, results for the 10 mm; at the bottom, results for the 30 mm simulation. Yellow dots represent query points . . . . . 109
- 5.9 DRAMMS: histogram of the number of registration calls leading to MNE values below its 5<sup>th</sup>-percentile. On the left, results for the 10 mm simulation, whereas for the 30 mm simulations on the right. Histograms are reported for the three most influencing parameters, in blue in the fat area and in orange in the muscle . . . . . 110
- 5.10 SyN: heatmap of the individual and joint sensitivity on the error metric (MNE). On the left, percentages relative to the total variance in the 10 mm simulation, whereas on the right for the 30 mm simulation (0.518632 mm<sup>2</sup> for the 10 mm simulation, and 3.16815 mm<sup>2</sup> for the 30 mm one). . . . . 111
- 5.11 SyN: surface plots showing the pair-wise distribution of the error metric (MNE, in [mm]) between the three most influencing parameters. On the top, results for the 10 mm; at the bottom, results for the 30 mm simulation. Yellow dots represent query points . . . . . 112
- 5.12 SyN: histogram of the number of registration calls leading to MNE values below its 5<sup>th</sup>-percentile. On the left, results for the 10 mm simulation, whereas for the 30 mm simulations on the right. Histograms are reported for the three most influencing parameters, in blue in the fat area and in orange in the muscle . . . . . 113

- 5.13 *elastix*: heatmap of the individual and joint sensitivity on the error metric (MNE). On the left, percentages relative to the total variance in the 10 mm simulation, whereas on the right for the 30 mm simulation ( $0.577863 \text{ mm}^2$  for the 10 mm simulation, and  $4.73588 \text{ mm}^2$  for the 30 mm one). . . . . 114
- 5.14 *elastix*: surface plots showing the pair-wise distribution of the error metric (MNE, in [mm]) between the three most influencing parameters. On the top, results for the 10 mm; at the bottom, results for the 30 mm simulation. Yellow dots represent query points . . . . . 115
- 5.15 *elastix*: histogram of the number of registration calls leading to MNE values below its 5<sup>th</sup>-percentile. On the left, results for the 10 mm simulation, whereas for the 30 mm simulations on the right. Histograms are reported for the three most influencing parameters, in blue in the fat area and in orange in the muscle . . . . . 116
- 5.16 Distribution of the magnitude of the error vectors (in [mm]). On the left column, results from the 10 mm simulation; on the right column, from the 30 mm simulation. From top row to bottom, DRAMMS, SyN and *elastix*. The muscle area is outlined in red. . . . . 117
- 6.1 Illustration of the acquisition set-up. On the top (a), schematic representation of the positioning of the subject in the bore of the scanner during acquisition; below on the left (b), photograph from one of the scanning sessions. An axial view of the wooden board used to support the buttocks is reported in (c): the 10 mm removable inserts used to reproduce the progressive stages of deformation are represented in light brown colour. Coronal views of the MR scans for the full-WB (d), partial-WB (e) and non-WB (f) conditions are reported on the right. Taken from Al-Dirini et al. [1] . . . . . 124

- 
- 6.2 Axial views of the initial alignment of the pelvic elements. The masks of the pelvis for the full-WB condition are delineated in blue, in green for the partial-WB and in orange for the non-WB scans. In purple, the muscle and fat areas are delineated as reference. . . . . 125
- 6.3 Axial (top) and sagittal (bottom) views of the displacement field for all the analysed subjects. Arrows show the direction of displacement vectors for both stages of deformation, that is, non-WB to partial-WB and partial-WB to full-WB. Length of vectors is scaled for visualisation purposes: the magnitude of the deformation from non-WB to full-WB is represented by the colormap. Fat and muscle ROIs are reported for reference. Axial and sagittal slices are located at the centre of the IT: for reference, the purple dotted line in the axial views show the location of the corresponding sagittal slice and vice-versa for the sagittal views. 126
- 6.4 Polar plot of the main components of the displacement field (right-left (R-L), posterior-anterior (P-A) and inferior-superior (I-S)) for the two stages of deformation analysed. Average values (here reported in [mm]) were evaluated over few ROIs (alongside their standard deviation between subjects): Medial Fat, Superficial Medial Muscle, Deep Medial Muscle, Muscle below IT, Muscle below GT, Deep Lateral Muscle, Superficial Lateral Muscle, Lateral Fat. . . . . 127
- 6.5 Axial (top) and sagittal (bottom) views of the distribution of the maximum compressive strain for the full deformation (non- to full-WB). Fat and muscle ROIs are delineated in turquoise and red, respectively, for reference. Axial and sagittal slices are located at the centre of the IT: for reference, the purple dotted line in the axial views show the location of the corresponding sagittal slice and vice-versa for the sagittal views. 128

- 
- 6.6 Polar plot of the main components of the Lagrangian strain tensor ( $E_{L-R}$ ,  $E_{P-A}$ ,  $E_{I-S}$ ) and the maximum shear strain ( $\gamma_{max}$ ) averaged over few ROIs: Medial Fat, Superficial Medial Muscle, Deep Medial Muscle, Muscle below IT, Muscle below GT, Deep Lateral Muscle, Superficial Lateral Muscle, Lateral Fat. . . . . 129
- 6.7 Spatial evolution of  $\gamma_{max}$  in the first (non- to partial-WB) and second (partial- to full-WB) stage of deformation. Curves represent average between subjects, whereas shaded areas the corresponding inter-subject variability. . . . . 130

---

## List of Tables

2.1	Main features of the deformable registration methods for medical imaging compared in this thesis work: SyN, DRAMMS and <i>elastix</i> . Computational effort was evaluated on an 8-core desktop computer with 64 Gb of memory. . . . .	32
3.1	Differences between scans acquired with the 7T and 3T scanners for both prone and supine positioning prior to correction and after correction with the scanner default software and with <i>gradunwarp</i> . Differences are represented in terms of average and standard deviation magnitude of the warp field in the brain area. . . . .	49
3.2	Rotation and translation values tested for the validation of the skull alignment. . . . .	52
3.3	Values of the parameters trialled in the optimisation of each registration methods. . . . .	58
3.4	Best parameter set for each registration methods. . . . .	66
4.1	Acquisition parameters for the structural sequences on the top row, whereas for diffusion sequence on the bottom row. . . . .	75

---

4.2	Average and standard deviation displacement values in the brain area with the corresponding inter-subject variability. Global statistics are extracted for the three components separately and for the magnitude of displacement. . . . .	80
4.3	Average and standard deviation values of strain in the brain area with the corresponding inter-subject variability along the three main directions.	83
5.1	Optimisation of the initial registration: ranges of parameters tested. Similarity measures tested include sum of squared differences (SSD), mutual information (MI) and correlation coefficient (CC) . . . . .	98
5.2	Ranges of parameters tested for the three deformable registration methods tested. . . . .	106
5.3	Optimal parameter set for each deformable registration method tested.	118
5.4	MNE values corresponding to the optimal parameter set, for each registration method. Values are extracted in the following ROIs: fat, superficial muscle and deep muscle. Values of the ground truth are also reported for comparison. . . . .	119

# Acronyms

*APD* Antero-posterior diameter

*BS* Brain shift

*DL* Deep learning

*DoF* Degrees of freedom

*DTI* Deep tissue injury

*DVC* Digital volume correlation

*FE* Finite element

*GM* Grey matter

*GT* Greater trochanter

*I – S* Inferior-superior

*IGNS* Image guided neurosurgical system

*IT* Ischial tuberosity

*L – R* Left-right

*MCB* Maximum cranial breadth

*MNE* Mean norm error



*MR* Magnetic resonance

*P – A* Posterior-anterior

*PBS* Positional brain shift

*R – L* Right-left

*ROI* Region of interest

*WB* Weight bearing

*WM* White matter

# Introduction

## 1.1 Overview

Navigation software for image-guided surgical interventions aids in planning a procedure to be carried out as minimally invasively as possible. Their use is critical for the optimal surgical outcome of procedures for deep brain stimulation, brain drug delivery and brain tissue biopsy. The planning is generally delineated on the base of the tissue distribution captured before a procedure generally via magnetic resonance (MR) imaging [2, 3]. However, surgical manipulation and gravity can induce deformation of the tissue (referred to as positional brain shift, PBS) that can invalidate the conditions which the planning was based on [4, 5]. This small shift has a magnitude comparable to the resolution of clinical scans and it is reported to be around or just below 1 mm [4–8]. A reliable and validated mathematical model for the intra-operative correction of surgical trajectories predicting such complex deformation is missing; accurate measurements of brain shift would undoubtedly improve the general understanding of the phenomenon, helping to assess the need for correction of surgical trajectories as well as how to achieve that.

Similarly, an accurate way to predict the deformation of soft tissues via mathematical models can benefit clinical strategies and systems for the control and prevention of pressure ulcers. They are localised areas of tissue degeneration and injury that result from sustained mechanical load and pose a considerable burden on patients and health-

care systems [9]. Further advancements in the prevention and management of pressure ulcers depend on the thorough understanding and reliable prediction of the onset of damage. This is particularly true for deep tissue injury, an ulceration frequent to the buttock where damage originates deep in the flesh and is not always associated with broken skin or external wounds. Damage initiation is related to the sustained straining effect of large tissue displacements, which are reported to reach values up to 27 mm in the gluteus maximus muscle [1, 10–12]. The response of the tissue can be modelled with computational biomechanical models (such as finite element modelling), which ultimately can have the potential to predict the initiation and location of the damage [13]. Rich deformation data depicting the mechanical response of a tissue sample is critical for their careful design and development, as well as for their thorough verification and clinical validation [14].

Recent advancements in imaging systems and computational capabilities have allowed not only the non-destructive visualisation of the internal conformation of samples, but also the characterisation of their deformation state under the effect of load [15]. Capturing the mechanical response of biological tissues is challenging due to their inhomogeneous nature, where the mechanical response varies throughout the tissue sample [16]. Such a complex mechanical behaviour can be characterised from the load applied and the constraints on the deformation (boundary conditions), only if the locally varying deformation of the sample is known in its entirety. Digital volume correlation (DVC) is a method that facilitates this [17]; in its simplest form, it makes use of imaged volumes representing the deformed and undeformed states of a sample to track the local movements of corresponding points or features. The full-field distribution of the spatially varying compression / extension state of a sample can then be visualised via maps of the displacement and strain fields and used to determine the mechanical response.

The importance of capturing the full-field measurements of spatially variable mechanical response of biological tissues is critical for the understanding of their response to load.

This information is crucial, as previously introduced, for the development as well as validation of clinical systems and strategies aimed at minimising tissue damage (e.g., surgical planning) or at preventing tissue injury (e.g., support surfaces). To complicate things further, the mechanical response of soft tissues is considerably affected by the surrounding biochemical environment and by the constraining effect of neighbouring tissues [18]. Any mechanical testing after tissue extraction (that is, *ex-vivo*) can give an inaccurate representation of their true mechanical behaviour. A non-destructive way to image the stages of deformation of biological tissues in their physiological environment (that is, *in-vivo*) is paramount.

Recent advancements in MR imaging has allowed the observation of the deep anatomy non-invasively and *in-vivo*, without the use of damaging radiation. In particular, the distribution of soft tissues can nowadays be captured over wide areas with excellent contrast, making the use of MR imaging in the clinical context ever growing. MR imaging consists in measuring the energy released by protons as they return to equilibrium after their direction of spin is perturbed [19]. An initial equilibrium is guaranteed by a strong magnetic field, which aligns the spins of magnetic atom nuclei towards along the same direction. This state of equilibrium is then perturbed via radiofrequency pulses, whereas spatial gradients are applied to encode spatial location. The time it takes for protons to return to equilibrium depends on the microstructure of the tissue; the volumetric conformation of different tissues can therefore be reconstructed with a suitable contrast over a wide area.

Thanks to the favourable contrast of tissues, MR imaging has also been recently used alongside digital volume correlation (DVC) to capture the deformation of hard tissues non-destructively and *in-vivo* [20, 21]. MR-based DVC enriches well-established experimental *ex-vivo* mechanical testing by depicting the response of tissues over a large volume in physiological conditions, surrounded by anatomical boundaries and under typical loads [16, 17]. *In-vivo* MR-based DVC has proved to be favourable in particular in the case of soft tissues, as their mechanical response is greatly affected

by tissue extraction and preservation [18]. However, their for soft tissues is somewhat limited [20], more so from clinical scans affected by limited resolution [21].

DVC studies investigating tissue response *in-vivo* are mostly based on anaesthetised animal models [20, 21]. Under these testing conditions, the conformation of the deformed and undeformed tissues can be acquired with appropriate resolution over a longer acquisition [20]. *In-vivo* MR imaging of compliant subjects, on the other hand, poses a compromise between resolution and acquisition time: rich spatial representation either requires unacceptable acquisition times due to subject comfort or it is affected by the artefacts given by unavoidable subject motion [22]. First and foremost, *in-vivo* MR scans have typically a resolution of just below a millimetre, limiting the spatial wavelengths of the deformation field that can be accurately reconstructed via DVC to only the ones larger than twice the resolution (without any constraints on the transformation model) [23, 24]. Secondly, the reconstruction of small displacements (that is, smaller than voxel resolution) relies on appropriate assumptions and constraints on the DVC calculations (that is, regularisation on the deformation model and on the optimisation). These guarantee sub-voxel resolution to some extent [24, 25]. Finally, error of the DVC measurements increases when capturing large deformations: the approximations and the assumptions which the deformable methods are based on can introduce inaccuracies in the estimated displacement field. First, the measure of similarity between two sub-regions to align suppresses high spatial variations in the displacement field, occluding, for instance, strain concentrations [24]. Moreover, there is a trade-off between accuracy and precision in the estimated displacement field; higher flexibility of the transformation model is required to accurately follow large deformations (such as strain concentrations), whereas precision is guaranteed by enforcing smoothness that limits spurious variations [25].

In the context of MR imaging, deformable registration methods for medical imaging have been developed on images affected by these limitations. One of the applications of these methods is capturing the small and large differences in anatomy between

subjects, so that scans of different individuals can be aligned together and compared in population studies [26]. Medical image processing and registration were major drivers for developments of DVC: these methods shares many similarities, although their progressions have differed due to the requirements of the individual applications [17]. Given that these freely-available methods have been thoroughly developed to tackle the specific challenges of *in-vivo* MR imaging on compliant subjects, it is natural to test their accuracy under such conditions before moving to DVC software developed for mechanical testing or material science.

Studies that have used medical image registration methods for *in-vivo* MR DVC [4, 5] lack a comprehensive and thorough evaluation of the accuracy of the measurements. Accuracy of the DVC calculations is of fundamental importance: it dictates the confidence in any clinical findings based on such measurements or their value for the validation and verification of computational models affected by or aimed at predicting biomechanical deformations. The work presented in this thesis aims to assess such accuracy on the two applications representing small and large deformation mentioned at the beginning of the section: that is, image-guided neurosurgery and prevention of deep tissue injuries. The comparison of the performance between these two deformation fields will be a first step towards understanding the absolute accuracy of such models.

## 1.2 Hypothesis and Research Questions

The work is based on the following hypothesis: *deformable registration methods for medical imaging have the accuracy and flexibility to capture, on a global and local scale, the small and large displacement of soft tissues in physiological conditions.*

This hypothesis is intended to give a measure of the degree of accuracy of well established deformable registration methods for medical imaging in following mechanically driven deformation of soft tissues. This was achieved by first testing the performance of three best performing registration methods in the literature (from Chapter 2, DRAMMS,

SyN and *elastix*) against the following two biomechanically plausible synthetic displacement fields: the small shift of the brain tissue under the effect of gravity; and the large deformations of tissues in the buttocks due to sitting. The minimal constraints on the estimation of the displacement fields limited any bias on the measurements given by any assumptions on the distribution of the deformation. The methods with their optimised parameters were then applied to real MR scans depicting *in-vivo* the aforementioned phenomena. Clinical conclusions were drawn where possible and the DVC measurements released as a freely available dataset for the development and verification of future biomechanical computational models.

The following research questions are addressed:

**Research question 1:** What is the accuracy of *in-vivo* MR DVC measurements of biomechanically induced small and large deformation fields?

**Research question 2:** Can *in-vivo* MR DVC measurements characterise the small displacements due to brain shift on a local and global scale, strengthening our understanding of the phenomenon?

**Research question 3:** Can *in-vivo* MR DVC measurements characterise the large displacements of the tissues of the buttock due to sitting on a local and global scale, strengthening our understanding of the phenomenon?

## 1.3 Thesis Structure and Contributions

Included in this section is a brief outline of the thesis and the corresponding contributions.

**Chapter 2** contains a literature review introducing the reader to the major technical works on image registration, with a focus on DVC and deformable registration for medical imaging. The chapter finishes with a brief introduction to sensitivity analysis,

an effective tool for error analysis, and to MR distortions, a critical source of error to any measurements of morphology based on MR scans.

**Chapter 3** begins with an introduction to the problem of PBS in the context of neurosurgery. Next, the main sources of error affecting DVC measurements of PBS from MR scans are investigated, namely, MR distortions, initial skull alignment and DVC measurements. Given the lack of a distortion-free imaging system, the effort that were made to measure MR distortions are reported: these were captured in relative terms as differences in the morphology in each of two subjects, imaged in two different scanners. The error related to the initial alignment of the skull (used as rigid reference between deformed and undeformed scans) is then examined, which was evaluated against few synthetic rotations and translations. Finally, the results of the optimisation of three deformable registration methods for medical imaging used for the DVC calculations are reported. Optimisation was carried out against a physically plausible deformation field replicating the small displacements due to PBS, obtained from a biomechanical computational model developed in the doctoral thesis by Nicholas Bennion [27]. This leads to the first contribution:

**Contribution 1** *Deformable registration methods for medical imaging showed accuracy which was one order of magnitude smaller than the resolution of the images in following a deformation field characterised by the small displacements representing positional brain shift. This addresses the first part of Research Question 1.*

**Chapter 4** contains the specifications of the acquisition protocol that was carried out to acquire PBS *in-vivo* from a population sample of 11 healthy individuals. The best registration method alongside its optimal parameter set from **Chapter 3** was then used to capture the deformation from the acquired scans. The chapter concludes with the analysis of the deformation and a few clinical implications. This leads to the second contribution:



**Contribution 2** *An average volumetric vector field with the corresponding inter-subject variability was extracted in-vivo, allowing tissue displacement within surgically relevant regions of interest to be characterised. This addresses Research Question 2.*

**Chapter 5** introduces the problem of deep tissue injury and the limitations of current clinical measures for the prevention and control of this type of pressure ulcers. Similarly to Chapter 3, the efforts made to quantify the main sources of error affecting DVC measurements from MR scans are reported. First, the results of the optimisation of three affine registration methods (FLIRT, ANTs and *elastix*) for medical imaging are reported; their accuracy in the alignment of pelvic skeletal elements to use as rigid references is investigated. Then, the outcome of the optimisation of three deformable registration methods is discussed, showing their accuracy in capturing simulated data of large deformations generated with a simplified biomechanical computational model of the buttock. This leads to the third contribution:

**Contribution 3** *Deformable registration methods for medical imaging showed accuracy which was around 10% of the average magnitude of the simulated deformation fields representing the large deformation of the buttock due to sitting. This addresses the second part of Research Question 1.*

**Chapter 6** shows the DVC measurements taken from the dataset provided by Al-Dirini et al. [1], depicting the progressive deformation of the buttock due to semi-recumbent sitting in 10 healthy individuals. The best registration methods (affine and deformable) alongside their optimal parameter sets from **Chapter 5** were used for the initial pelvic alignment and the following DVC measurements. The chapter concludes with the analysis of such deformation and few clinical implications. This leads to the fourth and final contribution:

**Contribution 4** *For the first time, the three-dimensional displacement field depicting the deformation of the buttock due to sitting in 10 healthy subjects was successfully*

*extracted in-vivo on a local and global scale, giving an extensive depiction of the pattern of deformation.* This addresses Research Question 3.

Finally, **Chapter 7** contains a conclusion of the work and findings presented in the thesis, as well as a delineation of further directions of development.

These contributions have resulted in the following peer-reviewed publication, where **Chapter 4** formed the main body and **Chapter 3** the supplementary materials:

Zappalá, S., Bennion, N. J., Potts, M. R., Wu, J., Kusmia, S., Jones, D. K., Evans, S. L., & Marshall, D. (2021). Full-field MRI measurements of *in-vivo* positional brain shift reveal the significance of intra-cranial geometry and head orientation for stereotactic surgery. *Scientific Reports*, 11(1), 17684. <https://doi.org/10.1038/S41598-021-97150-5>.

In addition, the draft of the following manuscript is to be submitted soon to the *Journal of Biomechanics*, where **Chapter 6** will form the main body and **Chapter 5** the supplementary materials:

Zappalà, S., Bethany E. K., Marshall, D., Wu J., Evans S. L. & Al-Dirini M. A. R.. Volumetric redistribution of the soft tissues in the human buttock captured from MR *in-vivo* scans: accuracy of measurements and analysis of deformation.

Finally, outcomes of the research have been presented in the following international conferences:

14-16/08/2019 : Two presentations at the 16<sup>th</sup> *International Symposium on Computer Methods in Biomechanics and Biomedical Engineering (CMBBE)* and the 4<sup>th</sup> *Conference on Imaging and Visualization*, New York City (USA) (Guarantors of Brain "Support for short meetings & conferences" bursary), titled "Digital Volume Correlation via Magnetic Resonance Imaging: an *In-vivo* Investigation

of Positional Brain Shift" and "Application of Digital Volume Correlation to the *In-vivo* Deformation of the Sub-dermal Tissues in the Human Buttock".

11-16/05/2019 : Electronic poster presentation at the *International Society for Magnetic Resonance in Medicine (ISMRM) 27<sup>th</sup> Annual Meeting & Exhibition*, Montreal (Canada) (ISMRM Educational stipend award), titled "Ten Minutes for the Brain to Settle: an *In-vivo* Investigation of Positional Brain Shift".

7-12/07/2018 : Poster presentation at the *8<sup>th</sup> World Congress of Biomechanics (WCB)*, Dublin (Ireland), titled "Is your brain deforming right now? An image-based investigation of the *in-vivo* positional brain shift".

# Literature Review

## 2.1 Overview

As introduced in Chapter 1, this thesis considers the suitability of digital volume correlation (DVC) measurements on the *in-vivo* deformation of soft tissues from magnetic resonance (MR) scans. This chapter aims to ensure that the content delivered in this thesis is as self-contained as possible: given the interdisciplinarity of the work carried out, a great effort was made to cover the most relevant technical contributions.

This chapter will begin with an introduction to deformable image registration, the backbone of DVC. The technical background to DVC will then be reviewed with a focus on its use in biological tissues. With the aim of investigating the deformation of soft tissues *in-vivo*, the chapter then moves on to reporting the main relevant literature on medical image registration, as they were designed and optimised on the limitations related to *in-vivo* MR scanning. Being very flexible tools, these methods need thorough parametric optimisation to gauge their suitability for DVC calculations and to assess the error in the measurements: sensitivity analysis for error analysis will therefore be briefly introduced. Finally, further in the assessment of the error affecting the DVC measurements, the problem of MR distortions will be introduced. MR distortions add a systematic error to the measurements and, hence, form another source of inaccuracy affecting MR-based DVC calculations.

The reader is asked to note that introductions to the two applications investigated

in the thesis (that is, positional brain shift and deep tissue injury) are reported in Chapters 3 and 5.

## 2.2 Image Registration

Image registration is a technique that allows the alignment of images on the basis of the common information they share, so that points representing similar features are mapped together. Image registration plays an important role, in particular, where the depiction of analogous information in the images to align differs in terms of view-points, intensity representations or time acquisitions [28]. Numerous disciplines have benefited from image registration, such as computer vision and medical imaging. The reader is pointed towards the following (among others) comprehensive reviews in the medical field for more details on the applications of image registration: Oliveira et al. [28], Sotiras et al. [26] and Keszei et al. [29].

Here, the problem of image registration will be considered between two images. One of the two images can be referred to as the moving (or source image), denoted by  $I_m(\mathbf{x})$  and defined in a three-dimensional discrete image domain made of voxels located at coordinates  $\mathbf{x} \in \mathbb{R}^3$ . The other image will be referred to as fixed (or target image) and denoted with  $I_f(\mathbf{x})$ , whose discrete domain of voxels is defined in a separate coordinate system from  $I_m(\mathbf{x})$ .

The registration problem lies in the estimation of the vector of parameters  $\mathbf{p}$  of the transformation  $T_{\mathbf{p}}$ , that maximises a similarity measure  $S$ , given some restrictions represented by the penalty term  $R$ :

$$\mathbf{p} = \arg \max_{\mathbf{p}} \left( S(I_f(\mathbf{x}), I_m(T_{\mathbf{p}} \circ \mathbf{x})) + \gamma R \right). \quad (2.1)$$

- The similarity measure  $S()$  represents the differences between features of the fixed image and the moving one after transformation  $I_m(T_{\mathbf{p}} \circ \mathbf{x})$  [30].

- The penalty term  $R$  enforces regularisation in the estimation, which incorporates *a-priori* information to restrict the estimation towards the space of feasible solutions (more details in the following sections) [31].
- $\gamma$  is the regularisation weight which controls the balance between the correspondence of features and the regularisation term.

The presentation of the image registration problem will be divided into its main three parts:

1. Definition of a search strategy.
2. Choice of the similarity measure.
3. Selection of the transformation model.

### **Search strategy**

Registration problems are generally solved with a non-linear optimisation technique, where the objective function describing the differences between images has a non-linear distribution and the search aims to find a global minimum, that is, the point that maximises their similarity. The discrete nature of the problem and the approximations in the calculations induce local minima to the search space that can deviate the registration estimation from an optimal solution.

Deformable image registration, in particular, is an inherently ill-posed problem where the number of unknowns exceeds the number of constraints [17, 26]. There is no closed-form solution and the search space has many local minima, giving different equally sub-optimal estimates of the unknowns. Constraints on the estimation are therefore needed to direct the registration towards the most reasonable transformation out of all the arbitrary ones that equally satisfy the registration problem. These constraints make the registration problem well-posed and an unique solution can be therefore determined [31].

Search strategy consists in spanning the search space in an efficient way, constraining the search only to meaningful alignment between images. Therefore, the quality of registration depends on the choice of search method and the constraints imposed [26]. In other words, if the similarity measure represents differences between features of the images, the optimisation aims to minimise such differences for a correct alignment [28].

Several optimisation algorithms has been developed over the years. Two main categories can be distinguished: continuous, where variables to estimate take continuous values and discrete, otherwise [26]. Some examples of continuous search strategies include gradient descent, conjugate gradient, Powell's conjugate directions, Levenberg-Marquardt, stochastic gradient descent. Continuous methods consist in refining the estimated parameters at each iteration by identifying and following the direction that ideally points towards the global minimum. Simpler methods are based on following the direction of the negative gradient of the cost function or the conjugate of the same direction [26]. An important parameter controlling the search is the gradient step. It represents the advancement of the solution in the direction of the minimum after each iteration, where large steps can decrease the time to reach convergence but can have the negative effect of deviating the solution from the minimum itself.

One approach to avoid local minima and direct the optimisation towards the optimal sub-space of acceptable solutions, and ultimately to the global minimum, is the pyramid strategy. This consists in progressively solving multiple registration sub-problems of the same image but from coarser to finer resolutions, where each successive step uses the previous best guess as initial transformation [32]. Downsampling the images, although being detrimental to the accuracy of the alignment, smooths the search space, suppressing most of the local sub-optimal minima [17]. At the end of the registration process the output is still based on the alignment of the images at their original resolution (guaranteeing precise alignment) but each iteration is based on an initial alignment given by a simpler registration process run on coarser versions of the same images. The multi-resolution pyramidal structure consists, in general, of four levels, with halved resolution

at each level from bottom (original resolution) to top. Multi-scale approaches have several advantages, such as speeding up the optimisation, increasing the convergence radius and being more robust to local minima [28].

### **Similarity Measure**

As more pertinent to MR image registration, this section will focus on intensity-based registration, where a suitable transformation is estimated based on the intensity distribution of the images. Feature-based (or geometric) registration problems, instead, will be quickly introduced at the end of the section.

Defining an appropriate criterion that measures the similarity between images is critical: first, it should account for the different physical principles of the acquisition systems so that the information from the intensities can be exploited to identify regions that are anatomically similar and should correspond. Moreover, it should be convex, allowing for accurate inference without distorting the information represented by the images [26].

The choice of the similarity measure depends on whether the registration problem is mono-modal, that is, similar acquisition modalities were used to acquire the images and similar distributions can be assumed; or multi-modal, where images have different distribution related to different acquisition modalities used. In the first case, the same anatomical structures are represented with similar intensity values, that mainly differ due to the noise affecting them. In this case, the simple sum of square differences between intensities can be the optimal similarity measure. On the other hand, when an affine relation has to be assumed between the intensities, then some variations of the cross-correlation are known to be more robust [17, 28].

In a multi-modality registration problem, instead, similar anatomical regions are not represented by similar intensity values. As no relation between the two intensity distributions can be assumed, similarity measures based on information criteria need to be chosen. Mutual information and its derived forms are the best choice in this



case. The measure comes from information theory and it is based on the calculation of joint distribution of intensity values [33]. The following two main limitations of the criterion motivated its many variants: degradation of alignment measure with overlapping regions [33]; limited spatial information born regarding the distribution of the features [30]. Normalised mutual information was therefore defined, as well as other variations aimed at including regional information as well [26].

As opposed to intensity-based problems, feature-based registration problems consist in minimising the distance between points or point-sets (such as curves or surfaces) that are manually or automatically extracted from the images. In the latter case, corresponding features do not have to be estimated during the registration call, as they are known, and the measure to minimise is the distance between point-sets [31]. The calculations are robust and straightforward; however, accuracy of the final alignment depends, to a great extent, on the reliability of their extraction and a vast number of them is needed for more complex deformable registration [26, 34]. The interested reader is pointed towards the review by Sotiras et al. [26].

The inclusion of spatial information to intensity-based criteria as additional geometrical features has shown promising results when similar anatomical structures are represented with similar intensity values. Examples of this are geometric moment invariants, local intensity histograms or Gabor filters [26, 35].

### **Transformation models**

The image registration approach can be global (or affine) or deformable (or non-linear, non-rigid) (see Figure 2.1): in the former, the transformation  $T_p$  from Equation 2.1 can be represented with a 4x4 homogeneous matrix that is common to every voxels in an image. In the latter case, a dense vector field at each voxel that best locally warps one image onto the other is outputted.

In the case of global registration methods, the transform is an affine mapping, where

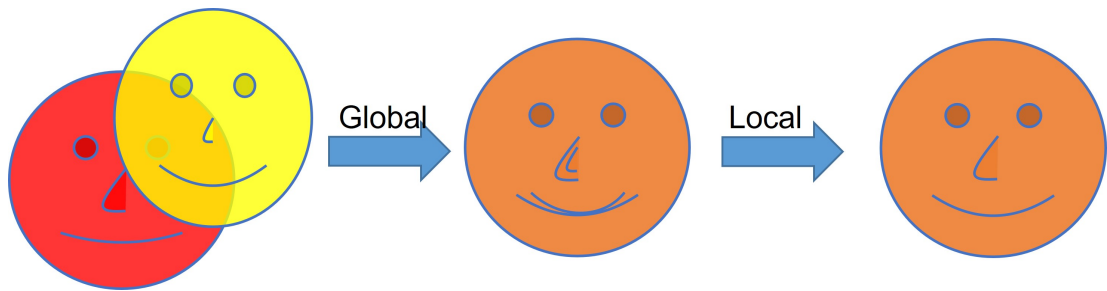


Figure 2.1: Depiction of the difference between a global (middle) and a deformable (right) registration problem.

parallel lines are corresponded to parallel lines [36]. The transform can be considered as a combination of the following components: translation, rotation, scale and skew (Figure 2.2) and it presents 12 degrees of freedom (DoF). The plethora of affine transforms also includes rigid transforms, composed by three components of rotation and three components of translation, making 6 DoF and similarity transforms, which also include three components of scaling, defining 9 DoF.

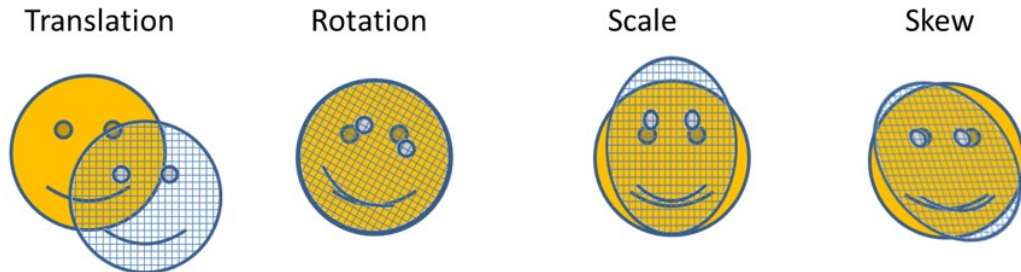


Figure 2.2: Depiction of the components of an affine transformation: translation, rotation, scale and skew.

In the case of deformable registration, the output transform is specific to sub-regions of the images [26]: the warp maps straight lines to curves [36]. The transform  $T_p$  is a dense mapping that varies spatially and presents numerous DoF (even millions [26]). In its most straightforward representation (i.e., non-parametric), the transformation can be considered as a three-dimensional warp field (or displacement field)  $\mathbf{u}(\mathbf{x})$ . The transformation is used to update the location of the voxel  $\mathbf{x}$  of the moving image, such that the new position of the voxel  $\hat{\mathbf{x}}$  can be retrieved as  $\hat{\mathbf{x}} = \mathbf{x} + \mathbf{u}(\mathbf{x})$ . A paramet-

erised representation of the warp field is often used to reduce the number of feasible transformations [26].

The choice of the transformation model impacts both the computational efficiency and the accuracy of the registration task [26]. The chosen transformation model imposes constraints on the overall estimation and should adhere to the nature of the deformation to follow. Increasing the complexity enriches the descriptive power of the model: however, higher complexity introduces higher computational demand; but more importantly it can also introduce spurious variations in the estimated warp affecting the estimation error.

Following the same classification as in Holden [36], transformation models for deformable registration can be enumerated as based on:

- Physical models.
- Interpolation/approx models.

The physical models solve the registration problem by interpreting the similarity between features of the images to register as a force that drives them together. These forces need to be in balance with the internal stresses generated, which can be interpreted as smoothness constraints on the deformation. The simplest models involve the use of linear elasticity that are based on only two parameters (Lamé constants  $\lambda$  that relates stresses to strain, and  $\mu$  that represents the shear modulus): the system to solve (Navier-Cauchy PDE) At each voxel then simplifies to 15 equations in 15 unknowns (6 values of strain, 6 values of stress and 3 values of displacement). The shortcoming of this model is that it ignores second-order terms of the displacement gradients, assumption that is valid only for infinitesimally small displacements. The transform exhibits sub-optimal performance in the case of inter-subject registration problems, which rely on capturing large deformations between features, up to a few centimetres [37].

Another transformation model inspired by physical phenomena is based on fluid-flow. Unlike the linear elastic one, it can model large localised deformations, with the draw-

back of an increased number of computations as well as greater registration errors [36]. It is based on solving Navier-Stokes partial differential equations, which are identical to the Navier-Cauchy ones but based on the velocity field, rather than on the deformation field. The Cauchy stress tensor here is a combination of hydrostatic fluid pressure (image similarity) and viscous stress tensor (constraints on the deformation field). Similarly to the linear elastic model, the registration problem is about balancing the momentum of the fluid with the pressure and the viscous forces. Optical flow models (such as Demons algorithm) are based on a similar concept, but incorporate the intensity gradient between frames representing incremental stages of deformation during registration [38, 39].

The second group includes transformations that are based on interpolation and approximation theory. In this section, the radial basis functions (RBFs) will be firstly described to then introduce basis-spline (B-spline) models, which possess desirable properties alongside good performance in terms of accuracy [40] and computational burden [36, 41].

RBFs are an umbrella of functions where the displacement is the sum of basis functions centred at some control points (or landmarks). These nodes do not have to correspond to a structured grid of voxels. The basis functions depend on the distance of a query point  $\mathbf{x}$  from a known point  $\mathbf{x}_i$  and they are positive definite functions. RBFs are fixed in the registration process, which aims to estimate the weight of each function that is summed up. RBFs generally have global support: although they perform well with sparsely populated data-points, the effect of outliers affects the whole displacement field [26]. One of the most used RBF are thin-plate splines [36]. They are the solution of a square Laplacian of the deformation field, which can be interpreted as a thin plane that passes on or next to control points. The smoothness of the plane is guaranteed by a resistance to bending. Although having useful smoothing properties and being able to fit through a sparse set of points, thin-plate splines are globally supported and struggle to follow more localised deformation.

Unlike thin-plate splines, B-splines have minimal support. In one dimension, any spline

function of degree  $n$  can be described as a linear combination of B-splines of the same degree over the same partition. A B-spline of order  $n$  is a basis function with minimal support around a control point: each one is obtained as a convolution of  $(n - 1)$ -order B-splines. The Cox-de Boor recursion formula allows the construction of B-splines of  $n^{th}$  order from two splines of order  $n - 1$ . A basis function of  $0^{th}$  order is defined as a step function between two knot points. The total number of control points depends on the number of knots and the degree of the spline, and their location depends on the fit to the data points that is wanted.

An example of a multivariate B-spline model is the free-form deformation (FFD) model, which can be formed from tensor products of univariate splines [26]. Their name represents the minimal assumptions they are based on, and distinguishes them from any knowledge-based methods where *a-priori* information on the deformation field is assumed [28]. Moreover, their support is local, hence the movement of a control point does not affect the whole warp field as in the case of thin-plate splines. Each point of an  $n$ -dimensional B-spline depends on  $n + 1$  neighbouring control points [42]. They are based on partitioning the support space into regularly spaced sub-domains (a lattice), defined by a grid of control points. For example, the cubic spline is defined, within the support region of sub-domain  $(u, v, w)$ , as:

$$\mathbf{u}(u, v, w) = \sum_{l=0, m=0, n=0}^{3,3,3} b_{l,3}(u)b_{m,3}(v)b_{n,3}(w)\mathbf{P}_{i+l, j+m, k+n} \quad (2.2)$$

where  $(i, j, k)$  are the indices spanning the grid of control points and  $b_{l,3}(u)$  the cubic

basis functions:

$$b_{0,3}(u) = \frac{(1-u)^3}{6}, \quad (2.3)$$

$$b_{1,3}(u) = \frac{3u^3 - 6u^2 + 4}{6}, \quad (2.4)$$

$$b_{2,3}(u) = \frac{-3u^3 + 3u^2 + 3u + 1}{6}, \quad (2.5)$$

$$b_{3,3}(u) = \frac{u^3}{6}. \quad (2.6)$$

Global deformations are captured with larger spacing between control points (and fewer number of DoF); whereas a tighter spacing allows to capture more information about the deformation and hence local differences in features (with the need of more computational burden given by the higher number of degrees of freedom) [43, 44]. Relative to thin-plate splines, B-splines are not only locally controlled (better fitting of local differences in features between images) but also computationally more efficient even with a large number of control points [43]. Similar penalty terms to the ones for the thin-plate splines can be added to increase the smoothness of the deformation field [43].

Other transformation models were considered to be out of the scope for the present work; the interested reader can find more information on registration via wavelets or knowledge-based approaches in the reviews by Holden et al. [36], Sotiras [26], and methods using machine learning in the reviews by Fu et al. [45] and Xiao et al. [46].

Additional constraints on the transformation model can guarantee good properties on the output warp field, allowing the model to have the flexibility to follow quick variations, while still guaranteeing good properties [26, 36]. These can be summarised as:

*Inverse consistency* - Registration algorithms are asymmetric, therefore the choice of fixed and moving images impacts the registration output. Inverse consistent methods aim at estimating both forward and backward transformations, constraining one to be the inverse of the other. These methods are symmetric only asymptotically and when the weight of the term imposing inverse consistency is dominant

over the similarity term.

*Symmetry* - Symmetric algorithms either are based on objective functions that are symmetric by construction, or the registration problem is based on two forward and backward sub-problems towards to a common mid-domain.

*Topology preservation* - Topology is preserved when injectivity and continuity is imposed onto the transformation model, as well as the continuity of its inverse. The determinant of the Jacobian guarantees injectivity of the warp field when it is greater than zero. The existence of the Jacobian implies the differentiability of the transformation and its continuity.

*Diffeomorphism* - Diffeomorphism is a stronger constraint aimed at preserving the topology whilst guaranteeing smooth mappings. Diffeomorphic transformations are differentiable mappings with a differentiable inverse.

Imposing diffeomorphism has shown good results when assumptions on the transformation models cannot be made, such as in the case of intra-subject registration [39]. Constraining the transformation to be diffeomorphic guarantees that connected / disconnected sets stay connected / disconnected, smoothness of curves and surfaces are maintained and points are transformed consistently [47]. Moreover, the use of diffeomorphic transform is motivated in the case of brain registration by microscopy studies showing a preservation of cell layout throughout the brain [48].

Although constraints on the deformation model are beneficial in most of the applications of image registration, tight constraints were shown to be detrimental on the accuracy of registration-based segmentation methods. In these cases, the quality of the propagation of the segmentations is of more importance than the smoothness of the obtained transformation, showing the benefits of looser constraints [40, 49].

This section has introduced the basis of deformable image registration, which is the backbone of DVC and image registration for medical imaging, which will now be described. The challenges related to *in-vivo* MR DVC will be presented. Then, deformable

image registration methods for medical imaging will be introduced and proposed as a initial solutions to address these limitations.

## 2.3 Digital Volume Correlation

In its simplest form, digital volume correlation (DVC) is a method that consists in estimating the displacement field from scans depicting consecutive stages of deformation of a sample. Differences between features in the two scans are tracked and the displacement field that induced the morphological differences outputted. One of the two images is iteratively morphed onto the other, in order to find the local warp field that best corresponds details of the features. At each iteration, the correspondence between sub-regions of the images is measured and the warp field updated until some condition on an acceptable alignment or number of iterations is reached. When features are properly aligned together, the output of DVC represents the distribution of the desired displacement field. Strain maps which depict the full-field compression state of the sample can then be calculated.

DVC extends other methods for strain evaluation, by giving the three-dimensional distribution over the whole imaged sample: strain gauges give a measure of strain only at discrete points on a surface, whereas extensometers give a one-dimensional measure over the whole sample [50]. Applications of DVC include the characterisation of the material properties of a sample, once boundary and loading conditions are accounted for. This is particularly beneficial in the case of heterogeneous materials, such as compressed stone wool, low density fiberboards, cellulose fibre mats and biological tissues [17, 50]. In these cases, strain gauges and extensometers would fail in the depiction of the complexity of the compression state of the sample. Moreover, DVC is used for the localisation of strain concentration for the identification of cracks and control of their propagation [51]. Finally, DVC measurements on biological tissues can further improve our understanding of tissue remodelling: tissue remodelling, as restoration and repair of



biological tissues, is a process that is partially strain-driven [52, 53].

The DVC method can be generalised into the following three main components [50]:

- Acquisition of the sample at different stages of deformation.
- Retrieval of the displacement field that best aligns features of the two volumes.
- Calculation of strain tensors from the computed displacement field.

Medical applications have been the major driver for early works on global DVC [17], both in terms of imaging systems to capture the stages of deformation and image processing to reconstruct the displacement field. In particular, the development of computed tomography (CT) and magnetic resonance (MR) imaging for diagnostic purposes has allowed the non-destructive depiction of the microstructure of both natural and industrial materials.

DVC and image registration for medical imaging have developed in separate ways due to the following differences: sub-voxel accuracy for the former versus voxel accuracy for the latter; small deformations caused by mechanical testing versus substantial warping caused by anatomical inter-subject variability; richness of features to align versus lack of suitable spatial and intensity resolution [17]. Early works using deformable registration methods for medical imaging for DVC include Schnaudigel et al. [5] and Gerard et al. [54].

**Volumes Acquisition** Imaging techniques used for DVC comprise of, but are not limited to, CT, MR, optical coherence tomography, confocal microscopy and ultrasonic imaging [17, 50]. The choice of imaging system is crucial, in order to acquire the stages of deformation with suitable spatial and intensity resolutions, without it interfering with the experimental set up. The main difference with its precursor, digital image correlation (DIC), is that accuracy of DVC measurements depends on the imaging systems' ability to reliably capture naturally occurring structural features with a suitable level of detail

and appropriate contrast. In the case of DIC, researchers can control on the quality of the random patterns that are deliberately drawn or sprayed on materials undergoing deformation to aid the correlation between the two images.

The conditions of testing pose considerable restrictions on the experimental apparatus and on the imaging system used. *Ex-situ* testing can be considered the simplest way of applying the load to a sample, as this is isolated from the original conditions and then tested. The sample can be prepared to fit the constraints of the imaging system or vice-versa. Specific experimental apparatus, instead, is needed for *in-situ* testing, where the sample is kept in its own original conditions and environment [17]. Regarding testing of biological samples, other conditions include *ex-vivo* and *in-vivo* testing. The former consists in testing the sample out of the physiological environment it originally came from, imposing fewer restrictions on the experimental apparatus. Although *ex-vivo* testing allows better quality of the acquired scans, tissue extraction and preservation negatively affect the mechanical behaviour of the tested sample. *In-vivo* testing, on the other hand, provides the real conditions of deformation and the true mechanical response of the samples; it poses, however, tight restrictions on the overall apparatus. Even tighter restrictions are related to *in-vivo* testing on human subjects for research purposes, where ethical approval is needed, for example, in case of using ionising radiation (e.g., CT) [55]. This leads to only the use of MR systems on compliant subjects, where high resolution scans cannot be obtained due to long acquisition times affecting the subject comfort and is not advised due to the artefacts related to unavoidable subject motion [22].

For instance, Dall'Ara et al. [20] compared the performance of two DVC methods (one local, the other global) on different datasets of *ex-vivo* zero-strain tests and one *in-vivo* database of bone structures on an anaesthetised rat model. Even in these ideal conditions where sample motion could be partially factored out, they showed that against *ex-vivo* testing, *in-vivo* DVC measurements were affected by higher errors due to moving artefacts and lower intensity contrast due to the lower radiation energy.

**Deformable Registration** DVC algorithms can be broadly categorised into two groups: local and global methods. The local methods were developed first and consist in partitioning the region to register into sub-volumes which are aligned independently. A displacement vector is then estimated for each sub-region, with inaccurate displacement calculations at boundaries [25]. All the contributions then need to be smoothed after estimation, to avoid discontinuities in the estimated displacement field [56]. The global DVC methods, instead, consist in outputting a dense displacement field, where each sub-volume contributes towards the whole output volume [17]. Regularisation is part of the estimation process and guarantees less discontinuities and inconsistencies in the output displacement field, leading to generally higher accuracy relative to local approaches [57]. With the aim of testing the suitability of deformable registration methods for medical imaging for DVC measurements, the second group will be the focus of the thesis work.

As previously mentioned, global DVC has many similarities with deformable registration for medical imaging, as the latter has been the major driver. The reader is referred to Section 2.2 for a presentation of the basis of the deformable registration component of DVC methods, that is, search strategy, similarity measure and transformation model. In the following, the challenges related to the deformable registration problems typical of DVC calculations are discussed.

Transformation model is the main component determining the accuracy of a DVC method. With the aim of reaching sub-voxel accuracy, displacement needs to be interpolated to have an estimate of displacement points between independent measurements [50]. Simpler interpolation models can give systematic errors (bias), as the displacement field does not have the flexibility to follow quick variations. On the other hand, higher order schemes have the flexibility to capture quick spatially varying components of deformation. This, however, introduces higher uncertainties, and subsequent variations in the outputted warp field [17, 50]. Uncertainty levels that arise from higher order deformation models can be kept under control by imposing stricter regularisation or by

choosing a larger spacing between independent measurements of displacements [17]. The larger the spacing, the lower the random errors associated with the displacement field [20], hence higher precision is achieved [58, 59]. However, the larger the spacing, the lower the flexibility of the transformation model to follow quick spatial variations, such as strain concentrations [25, 60], leading to systematic errors and decreasing accuracy. In particular in the case of large deformations, there is a trade-off between the accuracy of the measurements (that is, the higher complexity to follow quick spatial variations) and their precision (that is, the limited spurious variations around the true values). A balance between the flexibility and smoothness of the transformation model therefore play a pivotal role when capturing large displacements [25].

In the presence of large deformations, decorrelation effects can lead to improper calculation of the similarity between sub-regions of the images, with corresponded points representing different anatomical features [61, 62]. The pyramidal scheme introduced in Section 2.2, greatly limited the decorrelation effect in DIC and DVC calculations [61]. High-frequency content can anyway be lost in the cross-correlation due to the low-pass effect of the formulation due to the averaging process [24]: this can lead to loss in high frequency displacement information. Nogueira et al. [63] devised a window weighting function that flattens the frequency response and stabilise the frequency information (although the low-pass filtering effect cannot be factored out).

**Strain Calculations** The maps of the strain measurements can then be extracted from the dense displacement field. Among the many measures of strain, a convenient one is the Green-Lagrange strain,  $\mathbf{E}$ . By definition the translational and rotational components of deformation are discarded, so that only the compressive state of a sample even under larger deformations is represented [64]:

$$\mathbf{E} = \frac{1}{2} (\mathbf{F}^T \mathbf{F} - I), \quad (2.7)$$

$$\mathbf{F} = \frac{\partial \mathbf{u}(\mathbf{x})}{\partial \mathbf{x}} + I, \quad (2.8)$$

where  $\mathbf{x}$  is the voxel position in a Lagrangian coordinate system (that is, that moves with the material),  $\mathbf{u}(\mathbf{x})$  the deformation field,  $I$  the identity matrix and  $\mathbf{F}$  the deformation gradient.

The simplest way to calculate the deformation gradient  $\mathbf{F}$  is via central differences, where 3- (or more) point or formulae can be chosen depending on the level of noise affecting the displacements. Otherwise, a first- [65] or second-order [66] approximation of the strain tensor can be fitted to the displacement data via least-squares. The latter was shown to be advantageous when dealing with high strain gradients and showed the same level of errors in deriving strain values in the main field and at the edges of the field of view [66, 67].

The subset of displacement points used to calculate the tensors defines the strain window. The size of the strain window affects the accuracy of the calculations and its choice depends on the specific application [50]. On the one hand, larger strain windows reduce the noise affecting the displacement field (that are amplified in the differentiation) and generally lead to higher precision in the strain calculations [16, 67]. On the other hand, larger strain windows can attenuate existing strain gradients, reducing the capability of locating quick spatial variations in compression state and ultimately introducing systematic errors [16, 51]. This is particularly detrimental for the localisation of strain concentrations or in the case of strain distributions over irregular geometries.

This section has introduced DVC and its application to biological tissues. The challenges related to *in-vivo* MR DVC have also been discussed, in particular, in the case of acquisition on compliant subjects for research purposes. In the following section, the state of the art of deformable image registration methods for medical imaging will be introduced, as these methods have the accuracy and flexibility to be used for DVC measurements and have been developed to tackle the specific limitations of *in-vivo* MR imaging.

## 2.4 Medical Image Registration

Applications of image registration in the medical field include structural and functional image fusion, image subtraction for contrast enhanced images, population studies, surgical and radiotherapeutic planning, disease follow-up, and segmentation [28, 29, 40, 68]. There is a broad selection of freely available software for image registration, which come from many years of research in the medical field. This includes stand-alone registration methods [32, 35] as well as toolboxes with a broad selection of methods and utilities [44, 69]. Desirable aspects of a registration method are [29, 40]: versatility to be applicable to many scenarios; automatic, i.e., no need for parameter tuning; computationally fast and light to possibly be used in a clinical context; robust to noise, inhomogeneities, lost correspondences, pathological anatomy, different FOVs and intensity ranges; supported by clear and comprehensive manuals and wikis; consistent user support; finally, availability of utilities for auxiliary image processing [29].

Registration methods for medical imaging have nowadays the flexibility to be applied to many parts of the body [28]. To cite but a few, brain both in physiological [70] and pathological conditions [40], lungs [71], breast [43] and abdomen [72]. Generic registration algorithms have actually performed better than other methods tailored to any specific registration task by introducing some kind of a-priori constraints [71].

Recent research on medical image registration has focussed on models based on deep learning (DL). DL-based methods showed comparable results [73, 74] relative to the more conventional registration methods, with the benefits of requiring less computational demand, as most of these models are based on one iteration, and being less dependant on prior expert parameter tuning [73]. Two are the main categories, depending on the training that the models undergo: supervised, where examples of the registration problems are given for the model to learn from, prior to any application of the model; unsupervised, where the model learn from the registration problem to solve, without requiring training. State-of-the-art performance can be achieved with supervised models: they need, however, a large amount of labelled training data or reliable ground truth

to generate [46, 73]. In the case of unsupervised models, the deformation field is reconstructed without a ground truth as guidance, giving as output a warp field that can show spurious variations [75]. This thesis work will focus on conventional registration methods as research on guaranteeing good properties of the warp field from ML-based models is still ongoing, such as guaranteeing physically and physiologically plausible output warps [45, 73].

In the following section, the state of the art of academically popular deformable registration algorithms will be introduced and their selection justified in this section. The performance of many of these methods have been compared in several evaluation studies: the following section will begin with an introduction to such studies, to then describe in more details the best performing ones that were used in the thesis work.

One of the largest evaluation studies was carried out by Klein et al. [76]. It includes 14 deformable registration algorithms that were tested on 80 manually labelled brain scans and compared using 8 different error measures on both regions and surface overlaps. Scans were taken from four publicly available datasets, skull stripped and linearly registered to the MNI standard space prior to the non-linear registration. A total of 45,000 registrations were run. Algorithms were ranked on the basis of permutation tests, confidence intervals obtained from one-way ANOVA tests with Bonferroni correction, and indifference-zone ranking. SyN consistently showed good performance across subjects and label sets, reaching rank 1<sup>st</sup> in their evaluation system.

A few years later, the EMPIRE10 [71] challenge aimed to compare registration methods on different challenges related to the application of image registration to the CT scans of the lungs. A total of 34 and 20 algorithms in two separate phases were tested on the alignment of lung boundaries; alignment of major fissure (plate-like structure separating the top from the bottom side of the lungs); correspondence of 100 annotated landmarks that were automatically extracted and then matched by either three or four expert observers; correspondence of surgically implanted metallic markers on two ovine animal models (67 in the first, 103 in the second); singularity on the deformation field,

that is, the negative values of the determinant of the Jacobian. A ranking system for each one of these categories was designed in order to score each registration method. SyN and *elastix* were the top two performing methods (out of 20) in the second phase (taking place at the 2010 MICCAI Grand Challenge Workshop) of the EMPIRE10 challenge. In the first phase (taking place remotely in each participant's own facility), SyN still scored first; *elastix*, however, placed 7<sup>th</sup> out of 34.

In the evaluation by Ou et al. [40], the performance of twelve deformable image registration algorithms was tested against four challenges representing different challenges in brain clinical imaging: inter-subject anatomical variability; intensity inhomogeneity, noise and structural differences in raw images; acquisition protocol and FOV differences in multi-site databases; finally, pathology-induced missing correspondences. A combination of Dice coefficient and Hausdorff distance was used as performance criteria in the first three challenges. For the last one (presence of pathology), two independent experts were used to first define the contour of the abnormal region; then, 10 anatomical landmarks were identified in a 30 mm-wide band outside the abnormal region, with 40 landmarks in the rest of the images. SyN performed best at aligning cortical and sub-cortical structures from the simpler registration problems of skull-stripped images, followed by DRAMMS. DRAMMS then outperformed SyN (which came second) in the more challenging tests that included raw, multi-site and pathology-bearing images. [40]

Finally, Xu et al. [72] tested 6 registration methods on 100 abdominal CT scans. Thirteen abdominal organs were manually labelled by experts from each image. Scans were pairwise registered, leading to a large number of analysed registration problems. Dice coefficient, mean surface distance, and Hausdorff distance were used as error metrics. The aim of their study was to find the best method that aligns scans of different individuals for abdomen segmentation or atlas construction. The deformation field was reported to be discontinuous given the large number of organs in the abdominal area and the complexity of its morphology. For this reason, SyN performed worse comparably to other methods.



	<b>SyN</b>	<b>DRAMMS</b>	<b>Elastix</b>
<b>Similarity Measure</b>	Cross-correlation	High-dimensional Gabor filters	Mutual information
<b>Optimisation</b>	Gradient descent	Discrete	Adaptive Stochastic gradient descent
<b>Constraints on warp field</b>	Symmetric morphism	diffeo- Diffeomorphism	Twice continuously differentiable
<b>Computational time</b>	15 min	33 min	1 min
<b>Memory usage</b>	5 Gb	1 Gb	800 Mb

Table 2.1: Main features of the deformable registration methods for medical imaging compared in this thesis work: SyN, DRAMMS and *elastix*. Computational effort was evaluated on an 8-core desktop computer with 64 Gb of memory.

The evaluation studies gave a quantitative comparison of the performance of deformable registration methods for medical imaging and allowed the identification of the best performing ones. The remainder of this section will describe the best performing methods that were used in the present thesis work. In Table 2.1 a brief comparison of these methods is reported in terms of their similarity measure, optimisation process, constraints, computational time and memory usage.

**FLIRT** One of the most popular rigid registration algorithms used in medical image registration and therefore used in the present thesis work is FMRIB's Linear Image Registration Tool (FLIRT), part of the FMRIB Software Library (FSL). It was developed by Jenkinson and Smith [77] and it is based on a hybrid optimisation method, where both a global and local search is achieved via a multi-stage registration process.

The registration problem is first solved by a global search at 8 mm resolution. In this stage, three steps are run, that is, a coarse search over few rotation values for the best translation and scale values; a finer search over the rotation values, given the already extracted values of scale and translation; finally, a local optimisation for all three components for all the local minima identified in the previous steps. At 4 mm resolution, the three best guesses from the previous stage are perturbed and another refined solution found. Then, in the 2 mm and 1 mm resolution stages, the single best candidate transformation from the previous step (rotation, scale and translation) is used and a local optimisation is run to identify the optimal scale and skew (totalling 12 DoF).

For non entropy-based similarity measures, the contribution of a voxel is weighted by its distance from the boundaries of the FOV of the moving image, avoiding the effect of discontinuities in the intensity distribution. For entropy-based measures, instead, the binning needed to calculate the joint entropy is chosen so that they overlap (with a linear gradient), in order to have a smoother joint entropy (in other words, fuzzy-binning) [78].

**ANTs** The Advanced Normalization Tools (ANTs) is a comprehensive software library that includes methods for population analysis to capture statistics of the brain structure and its functions [69]. Among other auxiliary tools, ANTs offers a powerful registration method that allows the application of both affine and deformable image registration, which were used in the thesis work.

The following section will introduce the more complex deformable registration method, the symmetric image normalization (SyN) algorithm, as the affine algorithm follows a similar implementation. It allows the estimation of a transformation that is both diffeomorphic and symmetric. This guarantees that the transformation is differentiable as is its inverse and that there is no difference in the choice of which image to consider fixed or moving. The idea is based on deforming both the input images to a common mean shape. This leads to the estimation of two transformation fields which have velocity fields that are regularised over the path connecting one image to the common shape, guaranteeing the transformation to be diffeomorphic (and therefore the path to be a geodesic). This half-diffeomorphic transformation can then be joint together in order to define the overall warp field. The default similarity measure is the cross-correlation, but sum of squared differences and mutual information can be selected. The optimisation process is multi-scale and based on the gradient descend method. [79]

The initial implementation of the SyN method [79] implied the estimation of the vector field over all the voxels and with a constant sub-pixel update over the geodesic path between fixed and moving images. This implementation required substantial resources and a greedy version was created, which only stores vector fields solely at the extremities and at the mid-point of the geodesic connecting the moving to the fixed image, limiting the simultaneous storage needed [76]. The warp field was then extracted via a standard ordinary differential equations.

The default transformation model is based on the large deformation diffeomorphic metric mapping (LDDMM) [47], where the deformation is extracted from the velocity over time, whose estimation is regularised according to the Lagrange transport equation [79].

This formulation is a diffeomorphism by construction and it allows the definition of geodesic distances between points of the images to register, which proved to be beneficial in the analysis of brain anatomical variability [26]. A later implementation by Tustison et al. [80] included the B-spline formulation, which showed statistically significant better overlap values than the LDDMM implementation. This implementation is based on the directly manipulated FFD (DMFFD) which skips the smoothing needed during the gradient descent optimisation strategy used in traditional FFD models by projecting the update in the gradient fields to the class of B-spline functions. This was shown to alleviate the hemstitching effect that can happen with the traditional FFD formulation based on gradient descent, which can cause inefficiency in the optimisation process [80].

**DRAMMS** The deformable registration via attribute matching and mutual-saliency weighting (DRAMMS) is a robust algorithm based on the comparison of voxels represented by a set of attributes extracted from multi-scale and multi-orientation Gabor filters. The resulting method was proven to be robust to inter-subject variability, intensity inhomogeneities, noise, differences in the field of view and pathology-induced missed correspondences [40]. This is due to the estimation of the warp field, where each voxel is dynamically weighted during the process on the base of its saliency in defining a reliable correspondence. A salient correspondence is one that corresponds one voxel of the moving image to very little ones in the fixed image, guaranteeing a correspondence between identical anatomical features rather than just similar geometric features. Reliability is not measured independently in each image, but by giving higher weights to voxels of the moving image that are very similar to a neighbour of another in the fixed image and very dissimilar to the voxels on a peripheral neighbourhood. The weight of a voxel is extracted by comparing its set of attributes in the fixed image with the ones in a neighbourhood of the moving image. The rich set of Gabor attributes are then simplified by identifying the most salient ones based on a backward elimination and forward inclusion algorithm: this reduces the problem of the redundancy given by the non-orthogonality of all the scales and orientations of the Gabor filters, alongside

decreasing the computational burden.

The estimation of the transformation is based on the discrete optimisation, due to its computational efficiency and robustness to local minima. Finally, it can be considered multi-scale, since different scales of the Gabor filters represent different frequency contents [35].

The transformation model is based on the free form deformation (FFD) model by Rueckert et al. [49], based on composing transformations at multiple resolution levels that are guaranteed to be diffeomorphic by constraining the displacement of each control point not to exceed 40% of the spacing between them. More spaced control points lead to a smoother deformation field: therefore it was proven that constraining the maximum displacement on the base of the knot spacing would guarantee injectivity of the estimated transformation [81].

*elastix* *elastix* is a toolbox with a modular design that allows the user to test different registration options, including optimisation methods, multi-resolution schemes, transformation models, cost functions and interpolators. With the aim of making this flexible and powerful method more user-friendly, a database of parameter sets is available to the users (who are encouraged to upload theirs), with the aim of showing the best combinations in different studies for the specific application. The basic implementation is based on the (Insight Toolkit) ITK source library [44]. Both the affine and the deformable registration method from this library were used in the present thesis work. This section will focus on the latter, as the affine algorithm follows a similar implementation.

*elastix* allows the application a hierarchical strategy to the values of most parameters, including multi-resolution schemes that allow one to blur / downsample scans at higher levels of computations, as well as multi-level of complexity of transformation models, allowing for coarse resolutions at higher levels and the number of samples of the joint histogram bins when using MI-based similarity measures.

Many transformation models are available. In the present study, the affine registration

method and the deformable algorithm based on the FFD model by Rueckert et al. [43] were used. The main feature of the method is that transformation models are parameterised and the generic output of the call is not a warp field, yet a file of parameters. The function *transformix* can be used to evaluate the warp field at specific points / on a uniform grid.

Many optimisation strategies are available, as for instance uniform sampling on whole scans, outside scans (which showed good results in regularising the transformation model [44]), random sampling and sampling on masks to specify a region of interest. Random sparse sampling off-grid is also available, avoiding the irregularities on the cost function that are caused when sampling at points on the uniform voxel grid. The cost function shows peaks and troughs depending on the form of the transformation model at a specific iteration. The effect of the random off-grid sampling leads to smoother cost functions over the different forms of the transformation model over the iterations [44].

## 2.5 Sensitivity Analysis

Deformable registration methods for medical imaging are very powerful and have the flexibility to be applied to many body parts [71]. Their flexibility, however, can lead to variable performance depending on the parameter set used. The sensitivity of registration methods to these parameters is still an open topic of research [40].

Given the pivotal role of accuracy in displacement measurements, DVC methods have to be thoroughly optimised for the specific application [20]. Peña Fernández et al. [59] reported a decrease in 33% of the standard deviation of errors after optimisation in zero-strain measurements relative to the same experiment as in Dall’Ara et al. [20]. The following section will therefore report a quick introduction to sensitivity analysis, which aims to quantify the effect of parameters on the accuracy of the DVC measurements.

Sensitivity analysis allows the characterisation of the response of a model given the variation of input parameters [82]. Local sensitivity analysis infers the response of

a model in a neighbourhood of an instance of the input, whereas global sensitivity analysis aims to sample the whole hyperspace of reasonable values of the input, to gauge the response of the model for most of the possible combinations. Therefore, sampling techniques are needed in order to efficiently span the hyperspace of the input. Quasi-random sampling techniques such as Sobol's, Morris' and Latin hypercube allow one to span the space in a more efficient way than random sampling [83, 84].

Non-parametric linear regression and Pearson correlation were initially used to infer the linear and non-linear monotonic dependencies between input and the model's output [82]. More recently, variance-based methods were introduced, where the sensitivity of the model output to the model input is quantified in terms of the reduction in the variance of the model's output. Given  $X_i$  the random variable describing the distribution of the  $i^{th}$  parameter, then the variance of the output  $Y$  (here a random variable also it depends on the input  $X_i$ ), given that everything is known about the  $i^{th}$  parameter, is:

$$V_i = var\{E(Y|X_i)\}.$$

The measure  $V_i$  can be interpreted as the expected amount of uncertainty in the model output  $Y$  given that the true value of the input  $X_i$  is known [83]. The variance is evaluated between all possible values of  $X_i$ . If we then divide this variance by the overall variability of the random variable  $Y$ , then we obtain the main effect index  $S_i$ :

$$S_i = \frac{V_i}{var(Y)}. \quad (2.9)$$

Now, the uncertainty on the output, given that every input is known but the  $i^{th}$  parameter, can be expressed as:

$$V_{T_i} = var(Y) - var\{E(Y|\mathbf{X}_{-i})\}, \quad (2.10)$$

where  $\mathbf{X}_{-i}$  represents the random vector of the random variables representing each parameters excluding the  $i^{th}$  parameter. Similarly, the total effect index can be defined

as:

$$S_{T_i} = \frac{V_{T_i}}{\text{var}(Y)}. \quad (2.11)$$

It is straightforward to notice that:

$$\sum_{\text{parameters}} S_i \leq 1 \leq \sum_{\text{parameters}} S_{T_i}, \quad (2.12)$$

with equality only when all interactions are 0 [85]. Joint interactions between two (2<sup>nd</sup> order) or more parameters can be extracted by evaluating the joint expected reduction in the variance:

$$V_p = \text{var}\{E(Y|\mathbf{X}_p)\}, \quad (2.13)$$

where  $\mathbf{X}_p$  is the random vector representing all the desired parameters.

However, variance-based methods for sensitivity analysis need simulations in the order of over  $500(k + 2)$  considering only first order sensitivity (that is, without assessing pair-wise interactions), where  $k$  is the number of parameters influencing the model output [83]. For computationally expensive models where the number of runs achievable is somewhat limited, metamodels (or emulators) allow the extraction of the total sensitivity indices using considerably fewer model evaluations.

The meta-model described by Oakley and O'Hagan [85] and implemented in GEM-SA (used in the present thesis work), treats sensitivity analysis, and therefore the evaluation of  $S_i$  and  $S_{T_i}$ , with a Bayesian approach, imposing a multi-variate a-posteriori  $t$ -distribution of the output corresponding to any set of inputs. This allows the evaluation of the measures previously introduced as regression with Bayesian inference. This approach allows also the extraction of the uncertainty related to the estimations of the measures as confidence intervals. Two requirements are needed for the Gaussian process to best represent a model's response. First, the output needs to behave smoothly with respect to the inputs for mathematical tractability [85]. Moreover, independence of inputs allows a tidy decomposition of the total variance in first and second order



components.

The overall uncertainty was shown to be smaller than the one extracted with a brute-force Monte Carlo evaluation of the sensitivity of the parameters; moreover, Oakley and O'Hagan [85] reported that 15360 model evaluations were needed when using a variance-based method to achieve the same error as the one obtained with 250 model evaluations after fitting the metamodel.

## 2.6 MR Distortions

Finally, this literature review concludes with a brief presentation of MR distortions, which introduce an artificial warp to the MR scans, altering the true morphology of the imaged samples. These distortions ultimately affect the accuracy of DVC calculations by introducing a heterogeneous systematic error. The analysis of distortions is still an open problem and there is a general lack of a proper correction [86].

MR distortions depend both on the scanner used (static magnetic field inhomogeneities) or the gradient coil (gradient nonlinearities, eddy currents) and on the scanned object (chemical shift, susceptibility changes) [87–90]. Moreover, their effect is directly proportional to the magnetic field strength [91] and it is stronger further away from the iso-centre [86, 87, 89, 90], affecting more along the z-axis [86, 87]. Distribution on the brain area is non-uniform, with larger distortions in inferior and frontal areas, close to air-filled cavities [89, 90, 92].

The literature reports either phantom or clinical studies where CT scans were used as ground truth to infer the accuracy and fidelity of MR imaging. Care must be taken when interpreting results based on phantom studies: a more complex distribution of distortions is to be expected when scanning participants, due to the effects of susceptibility related to iron deposits in the basal ganglia, signal cancellations at air-tissue boundaries, chemical shift and flow effect [88].

Watanabe et al. [87] reported an accuracy on corrected MPRAGE scans of a phantom acquired with a 3T scanner, giving a root mean squared error of  $1.8 \pm 0.36$  mm. The authors also state that the default algorithm developed by the scanner's vendor did not correct to a satisfactory level. Karger et al. [88] reported an average  $\pm$  standard deviation of  $1.3 \pm 0.3$  mm,  $0.9 \pm 0.1$  mm and  $0.9 \pm 0.5$  mm superiorly, centrally and inferiorly on corrected images of a phantom on a 3T scanner. On a 1.5T scanner, instead, they reported values of  $1.1 \pm 0.3$  mm,  $1.4 \pm 0.2$  mm and  $1.5 \pm 0.4$  mm, respectively. Damman et al. [89] found distortion values of  $0.6 \pm 0.1$  mm and  $0.5 \pm 0.1$  mm on 1.5 and 7T scanners, respectively, when acquiring MPRAGE images of a phantom, after applying a 3D scanner-default distortion correction. Duchin et al. [90] carried out the study on clinical images. They showed errors just above 1 mm when identifying landmarks on 7T images after affine registration to CT, for an actively shielded 7T scanner. Their main finding is that affine registration was enough to model the distortion at high MR field, obtaining an acceptable alignment with CT images. Neumann et al. [86] reported a targeting error on a non-clinical study assessing the accuracy of stereotactic targeting of  $1.31 \pm 0.41$  mm on 1.5T and  $1.42 \pm 0.56$  mm on 3T MPRAGE images corrected with the scanner-default correction algorithm. Treiber et al. [93] report median displacement of 2.11 mm, (5<sup>th</sup> and 95<sup>th</sup> percentiles: 1.2 mm to 5.9 mm respectively). Regions mostly affected were the brainstem (median distortion 5.43 mm), temporal lobe (2.61 mm), and frontal lobe (2.21 mm), while the parietal (1.61 mm) and occipital (1.77 mm) lobes had the least amount of distortion. In particular, the temporal and frontal parenchyma adjacent to the bone-air interfaces showed distortions as severe as the brainstem. Again, they report these values relative to the MR structural scans, considered as ground truth, with no CT imaging.

Regarding the effect of acquisition sequences, both Neumann et al. [86] and Watanabe et al. [87] showed that MPRAGE led to worse, even if comparable, accuracy in comparison to using other contrast, as FLASH or VIBE. Moreover, Dammann et al. [89] showed greater distortion when using T2-weighted sequences than using T1-weighted sequences, due to longer echo time and inhomogeneities in the B1 field that affected the refocusing

of the magnetisation spins.

## **2.7 Summary**

This chapter has provided a comprehensive review of the key technical literature relevant to the research questions outlined in Section 1. The literature on such an interdisciplinary problem is substantial: a great effort was made to cover the most relevant contributions to the work carried out in the thesis. The reader is asked to note that introductions to the two applications investigated in the study are reported in Chapters 3 and 5: respectively, brain shift and deep tissue injury.

Image registration was firstly introduced as a basis for DVC and deformable registration in the medical field. This was followed by a brief description of DVC and the main technical contributions in the biomechanical field. The state-of-the-art registration methods for medical imaging were then presented as well as sensitivity analysis for the evaluation of their dependence on input parameters. Finally, the chapter concluded with a description of the MR distortions, which add a heterogeneous component of systematic error to the DVC measurements.

# **Brain Shift: Parametric Identification and Error Analysis**

## **Overview**

This chapter aims to evaluate the suitability of deformable registration for medical imaging in capturing small deformations due to positional brain shift (PBS), the sagging of the brain tissue due to the effect of gravity alone. Previous works that aimed at measuring PBS lacked of a thorough quantification of the accuracy of the measurements taken and of the sources of error affecting them [4–6, 8]. Quantifying the error affecting the measurements is paramount to gauge the confidence on the obtained results and the validity of their interpretations. The work of this chapter aimed at investigating the following main sources of error: magnetic resonance (MR) distortions, improper initial rigid registration and inaccuracies in the DVC measurements. Results advised on the margin of error associated to the DVC measurements of *in-vivo* PBS that will be introduced in Chapter 4.

The work presented in this chapter is part of the supplementary materials of the following peer-reviewed paper:

Zappalá, S., Bennion, N. J., Potts, M. R., Wu, J., Kusmia, S., Jones, D. K., Evans, S. L., & Marshall, D. (2021). Full-field MRI measurements of *in-vivo* positional brain shift reveal the significance of intra-cranial geometry and head

orientation for stereotactic surgery. *Scientific Reports*, 11(1), 17684. <https://doi.org/10.1038/S41598-021-97150-5>.

The chapter first presents in Section 3.1 the problem of PBS and its relevance to image-guided neurosurgical systems (IGNS).

Section 3.2 shows the extent of MR distortions affecting the brain morphology in two subjects acquired with two different scanners. The relative performance of two distortion correction methods were compared and the best one for the specific application identified.

Section 3.3 shows the efforts that were made to assess the accuracy of the initial skull alignment against some synthetic rotations and translations. An improper initial alignment of reference elements that do not undergo deformation can add an additional component of rigid displacement to the DVC measurements.

Finally, Section 3.4 shows the optimisation of three deformable registration methods for medical imaging against a synthetic deformation field representing PBS. Accuracy of the DVC measurements with the optimal parameter set was then determined.

### **3.1 Introduction to Brain Shift**

Given its low stiffness, brain tissue shifts within the skull cavity under the effect of gravity due to changes in head orientation even in normal healthy individuals without any surgical manipulation [4, 5, 54]. This shift is reported to be a non-rigid deformation induced by a complex interaction of gravity, geometry of contact surfaces, fluid pressure, mechanical response, presence of pathological tissue and surgical procedure [4, 5, 54, 94]. Displacements of a few millimetres are typically observed in physiological conditions, whereas displacements as large as a few centimetres can be observed for pathological causes (e.g. tumour, hydrocephalus) or surgical intervention (e.g. skull or dura opening, cerebro-spinal fluid leakage, device insertion, tissue resection) [3, 95, 96].

Commonly referred to as brain shift (BS), displacements are generally comparable if not 2-3 times larger than the current accuracy of image-guided neurosurgical systems (IGNS) [4, 5, 97]. These systems are routinely used for the planning and navigation of stereotactic procedures such as deep brain stimulation, local drug delivery and stereotactic biopsy [2, 3, 98]. IGNS allow the planning of the surgical trajectories and the indirect navigation of the surgeon to a target area, using as reference pre-operative scans. Accurate planning is essential in order to target the correct structure, as well as to define a minimal entry point in the skull and limit damage to tissue (cortical veins, sulci and lateral ventricles) surrounding the path to the medical devices [99, 100]. An example of the interface of one of these IGNS is reported in Figure 3.1.

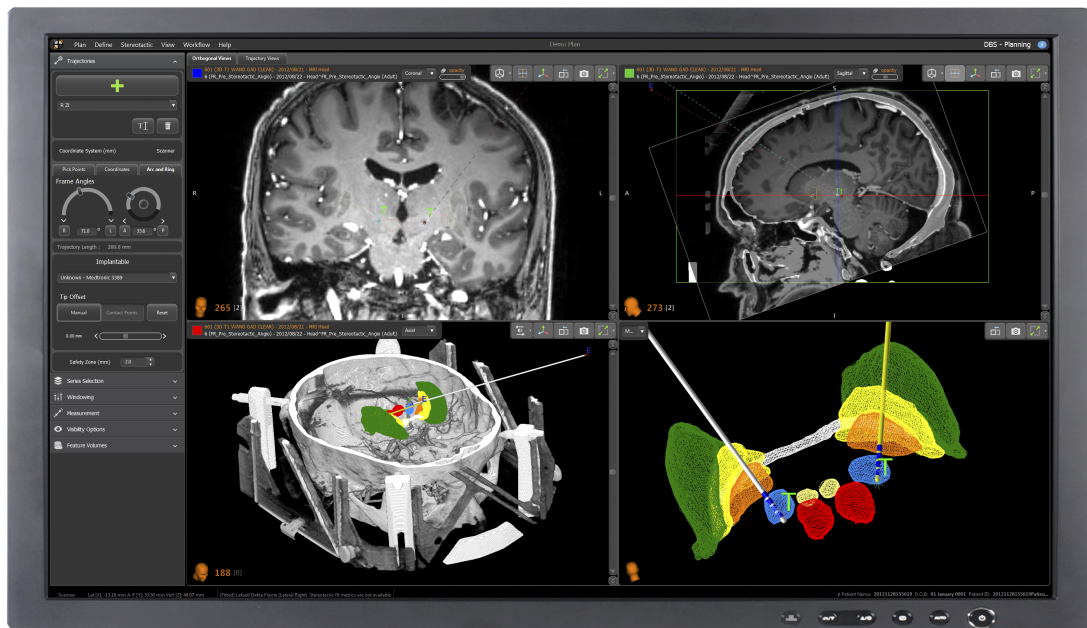


Figure 3.1: Example of an IGNS software: interface of Renishaw *neuroinspire*<sup>TM</sup> designed for the planning of most stereotactic neurosurgical procedures. Taken from <https://www.renishaw.com/en/neuroinspire-neurosurgical-planning-software--8244>

Provision of correct neuronal stimulation, drug administration or tissue biopsy requires accurate placement of the probe to within 1-2 mm of the target [99, 101–103]. Despite showing sub-millimetre accuracy [3, 98, 102], IGNS usually rely on a global rigid alignment of the pre-operative coordinate system to the patient reference on the surgical

table (acquired via intra-operative imaging); this approach implicitly assumes that every structure rotates and translates in an identical fashion and, as such, maintains the same dimensions and shape [54, 104, 105]. However, the BS caused by any slight differences in head orientation between the pre-operative scanning session and the surgical procedure can cause a non-uniform deformation comparable in magnitude to the margin of error for surgical targeting [4–6]. Therefore, this positional BS (PBS) occurring without any presence of pathology nor surgical manipulation can affect the outcome of a procedure, as the planned targets might differ from their actual location. Any further improvements of IGNS do not rely on the accuracy of each individual components, but on the addition of a suitable correction of the location of surgical targets given the PBS arising during a surgical procedure.

Due to PBS, IGNS have recently been used only to localise targets, and are not fully trusted [54]. The clinical standard for checking the correct positioning is micro-electrode recording (MER), which is based on the insertion of a single or multiple small-tip electrodes that register the single cell or group neuronal activity in order to locate structures of interest depending on their firing frequency and amplitude [106–108]. As this invasive technique requires a compliant patient, anaesthesia has to be stopped during the procedure. Further, the risk of haemorrhagic complications is high [106].

Intra-operative imaging and computational modelling are two emerging techniques that have been recently used alongside IGNS to update the location of target areas given the effect of PBS. The former is based on the use of MR imaging, computer tomography (CT), ultrasound (US) or optical systems in the surgical room [99, 100, 109, 110]. The actual conformation of the brain tissue as well as the location of the implanted medical devices can be imaged during the surgical procedure. Starr et al. [100] showed that, in comparison with standard stereotactic procedures based on MER checking, the use of intra-operative imaging gave a 29% improvement in the placement error, with a 60% improvement in the off-medication state in the follow-up. Even if minimally invasive, these systems are questionable due to the cost of the equipment needed; the impact on

the workflow; the poor image quality; the exposure to ionising radiations in the CT case or any hazard in an MR environment [54, 95, 109].

Compensation for PBS via mathematical models have recently shown promising results [109, 111]. Given the increasing availability of computational power, such complex models can be run almost in real-time [112–114]. One such example is finite element (FE) modelling, which are becoming an accurate and cost-effective solution in a neurosurgical context [109, 111]. FE modelling is based on simulating the mechanical response of complex structures (brain) under loading conditions (gravity), which are constrained by boundaries (meninges, falx, tentorium, etc). FE models have the capability to simulate complex processes, such as the head orientation chosen for surgery, the extent and position of the skull opening, the insertion of medical devices. Among others, Dumpuri et al. [111] and Sun et al. [113] reported an error of  $0.7 \pm 0.3$  mm in the prediction of PBS driven by the captured deformation of the tissue from an exposed brain area. Garlapati et al. [115] showed that a linear FE outperformed the state-of-the-art registration technique for the compensation of PBS through intra-operative imaging. Although non-invasive and cost-effective compensation for the shift arising during a procedure, such models are still a long way from being the clinical standard in image-guided neurosurgery due to lack of comprehensive clinical validation [97, 109, 116].

Further improvements in compensation measures suitable for clinical practise require a comprehensive understanding of the mechanics behind PBS as well as rich datasets to verify and validate such measures against [18]. In achieving this, the following and the next chapter will focus on the efforts that were made to capture *in-vivo* the PBS in a population of 11 healthy subjects. The characterisation of the mechanics in normal physiological conditions (i.e., in the healthy brain) is the first step towards modelling the more challenging shift induced by pathology or surgical manipulation. To the best of the author's knowledge, previous studies were based on observations mostly limited to surfaces [4, 5] or based on measurements at specific locations [7, 8]. This motivated the three-dimensional, full-field DVC measurements that were captured



*in-vivo* of PBS from MR images that will be introduced in Chapter 4. However, the validity of any interpretations of the DVC calculations depend on their accuracy, that is, on the quantification of the sources of error affecting the measurements. This chapter will show the efforts that were made to achieve this.

## 3.2 MR Distortions

As introduced in Chapter 2, residual MR distortions after shimming cause a spurious warp in the scans which depends on the magnetic field and gradients applied, as well as on the way the imaged object perturbs the MR field. If not fully compensated for, this spurious warp is a source of error in the DVC measurements, since it is acquired as additional component of deformation. Given the sub-optimal performance of a built-in correction method reported by Watanabe et al. [87], the following section shows the relative performance of the compensation method developed by the vendor of the scanner against *gradunwarp*, the standard correction used in a multi-site and multi-modality acquisition project over a large population sample [117].

**Methods** The performance of the distortion correction method built in the scanners was compared to *gradunwarp* [118], the correction method used in the WU-Minn Human Connectome Project consortium [117]. Both methods calculate the distortion field from the spherical harmonic coefficients specific to the scanner [118]. These normalised coefficients represent non-linear terms of the truncated series of the distribution of the distortion field, which can be used to reconstruct the three-dimensional warp field approximating the MR distortions.

Two subjects were both scanned in a Siemens 7T MAGNETOM (Siemens Healthcare, Erlangen, Germany) and in a Siemens 3T PRISMA at the same Cardiff University Brain Research Imaging Centre (CUBRIC), Cardiff University in different acquisition sessions. T1-weighted MPRAGE scans were acquired, which parameters are reported

Correction	Prone	Supine
None	$1.88 \pm 0.34$ mm	$1.40 \pm 0.36$ mm
Scanner default	$1.32 \pm 0.11$ mm	$1.31 \pm 0.33$ mm
<i>gradunwarp</i>	$1.25 \pm 0.10$ mm	$1.30 \pm 0.20$ mm

Table 3.1: Differences between scans acquired with the 7T and 3T scanners for both prone and supine positioning prior to correction and after correction with the scanner default software and with *gradunwarp*. Differences are represented in terms of average and standard deviation magnitude of the warp field in the brain area.

in Table 4.1. Images acquired with the 7T scanner were warped to the 3T ones via deformable registration (symmetric image normalisation (SyN) [79]), prior to any correction as well as after correction with the built-in method and with *gradunwarp*. This approach was used for scans acquired with subject lying both in prone and in supine positions. The correction method leading to the smallest differences between scans in the same position from different scanners was therefore used for the DVC measurements of Chapter 4. Differences between scans were calculated as norms of the vectors from the warped field output of the deformable registration.

**Results** Results (Table 3.1) show a better correspondence between scans after using the software *gradunwarp*. In prone position, the warp field representing differences between scans was on average 33% smaller after using *gradunwarp*, and 30% smaller after using the scanner-default software; in supine position, these values were considerably smaller, that is, 7% and 6%, respectively.

Fig. 3.2 shows the distribution of the error norms after aligning the 3T and 7T scans (prone on the left, supine on the right) over some regions of interest (ROI). The figure confirms the previously mentioned larger effect of distortions in prone images than in supine images. Moreover, it shows larger differences in frontal regions relative to posterior ones. Finally, lateral differences can be noticed, with larger errors in the same left regions relative to the scanner reference (that is, right regions in the plot for prone positioning and left regions in the plot for supine positioning, relative to the anatomical

reference).

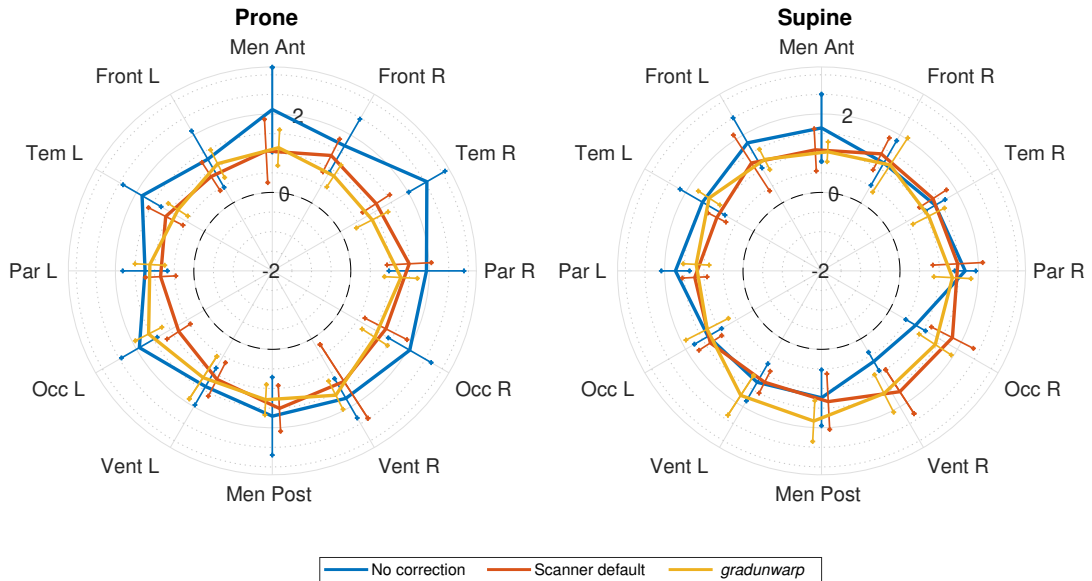


Figure 3.2: Average magnitude of the warp field representing differences between scans from different scanners. On the right, results when imaging the subjects in prone position, whereas in supine on the right. Whiskers represent intra-region variability. In blue, differences between scans with no correction applied; in orange and yellow error after correction with the scanner default method and *gradunwarp*. Values are evaluated over the following ROI: left (L) and right (R) anterior and posterior meninges (Men Ant, Men Post), frontal lobe (Front), temporal lobe (Temp), ventricles (Vent), parietal lobe (Par), occipital lobe (Occ).

**Discussion** The relative performance of MR distortion correction methods showed a better correspondence between anatomies after correction with the software *gradunwarp*, which was therefore used for the DVC measurements in Chapter 4. Differences between the morphology of the same subject acquired with different scanners were  $1.25 \pm 0.10$  mm in prone positioning and  $1.30 \pm 0.20$  mm in supine.

Results are in line with previous studies: Watanabe et al. [87] reported an improvement in the root mean squared error of 15% after using the default distortion correction with a 3T scanner. Karger et al. [88] reported an decrease of 54% in mean deviation with a 3T scanner and 12% with a 1.5T scanner. Tavares et al. [119] reported an improvement of 43% with a 1.5T scanner. Finally, Neumann et al. [86] found an increased accuracy of

6% with 3T and up to 55% with 1.5T scanners after applying the distortion correction.

Differences after correction (either with the scanner default compensation or *gradunwarp*) led to more consistent differences in anatomy between ROI as well as between prone and supine positions. Larger differences in the frontal regions can be related to the effect of air cavities, which are known to affect the MR field [89, 90, 92]. The differences noticed along the lateral direction are in line with the MR distortions along the same direction reported on two phantoms to give absolute differences of  $0.4 \pm 0.2$  mm on 7T [89] and  $1.3 \pm 0.26$  mm on a 3T scanner [87], respectively, both after correction.

Although not providing an absolute error related to the MR distortions, the following results show the importance of applying distortion correction, which reduced differences in anatomy between scanners. A considerable residual warp has to be acknowledged ( $1.30 \pm 0.20$  mm) even after correction. This residual error could have been a combination of the unknown MR distortions affecting the 3T scans (used as reference), which could not be determined; inaccuracy in the deformable registration call; and the likely differences in tissue conformation due to slight different head positioning, as images were acquired in different acquisition sessions. Further investigation is needed to evaluate the distribution of MR distortions specific to the scanner against a distortion free ground truth.

### 3.3 Skull Alignment

Differences between anatomical features of the deformed and undeformed scans should be solely related to the deformation of the soft tissues. In these conditions, the output of the DVC measurements depicts the desired displacement field at soft tissues. Hard tissues, such as skeletal elements, do not undergo deformation; therefore, they can be considered as rigid reference and need to be accurately aligned between the two scans (that is, setting the initial conditions of deformation). Any differences between these reference structures is captured as additional component of deformation by the DVC

calculations. The following section aims at quantifying the error related to this initial registration step.

**Methods** The error related to such alignment was determined against few synthetic rigid transformations. Three best performing affine registration methods from the following software libraries were compared: FSL [78], ANTs [79] and *elastix* [44]. Typical rotations and translations that were seen in the study were represented (Table 3.2). A maximum rotation of  $30^\circ$  was applied around the left-right axis (tilt),  $5^\circ$  around the posterior-anterior one (roll) and  $10^\circ$  around the interior-superior axis (pan). Translation was kept to a maximum of 5 mm, given the initial alignment of the centre of images implemented in most of the registration algorithms. Few compositions of these were also tried. Transformations were applied to the MPRAGE scans of 8 subjects from a 7T scanner (further details in Section 4.2) prior to the skull-based registration. Rician noise was added to the generated images, which standard deviation was set to the noise distribution affecting the background of the original image [120]. Given the extensive investigation in the literature regarding linear registration problems applied to the alignment of brain structures, optimisation was considered unnecessary and the default parameters regarded as optimal for these simple intra-subject and intra-modality registration calls.

	L-R angle	P-A angle	I-S angle	L-R translation	P-A translation	I-S translation
T <sub>1</sub>	$30^\circ$	$0^\circ$	$0^\circ$	5 mm	0 mm	0 mm
T <sub>2</sub>	$0^\circ$	$5^\circ$	$0^\circ$	0 mm	5 mm	0 mm
T <sub>3</sub>	$0^\circ$	$0^\circ$	$10^\circ$	0 mm	0 mm	5 mm
T <sub>4</sub>	$-30^\circ$	$0^\circ$	$0^\circ$	-5 mm	0 mm	0 mm
T <sub>5</sub>	$0^\circ$	$-5^\circ$	$0^\circ$	0 mm	-5 mm	0 mm
T <sub>6</sub>	$0^\circ$	$0^\circ$	$-10^\circ$	0 mm	0 mm	5 mm
T <sub>7</sub>	$15^\circ$	$-2.5^\circ$	$-5^\circ$	2 mm	-2 mm	2 mm
T <sub>8</sub>	$15^\circ$	$-2.5^\circ$	$5^\circ$	2 mm	2 mm	-2 mm
T <sub>9</sub>	$-15^\circ$	$-2.5^\circ$	$5^\circ$	-2 mm	2 mm	2 mm
T <sub>10</sub>	$-15^\circ$	$2.5^\circ$	$-5^\circ$	-2 mm	2 mm	-2 mm

Table 3.2: Rotation and translation values tested for the validation of the skull alignment.

The accuracy of this initial step was evaluated by calculating the Dice coefficient (DC),

given by [121]:

$$\frac{|Q \cap \hat{P}|}{|Q| + |\hat{P}|}, \quad (3.1)$$

where  $Q$  represents the original skull segmentation and  $\hat{P}$  the skull segmentation after registration of the synthetic images. These segmentations were automatically generated via the brain extraction tool (BET) command of the FSL software library [122].

Rohlfing [123] showed that DC alone is not sufficient to gauge the accuracy of the alignment between unlocalised regions such as the brain, which contain little information on spatial location. An additional measure was therefore used, that is, the Hausdorff distance  $HD$  [124]:

$$HD = \max \left( \overrightarrow{HD}(\hat{P}, Q), \overrightarrow{HD}(Q, \hat{P}) \right), \quad (3.2)$$

$$\overrightarrow{HD}(\hat{P}, Q) = \max_{\forall p \in \hat{P}} \left( \min_{\forall q \in Q} \|p - q\| \right), \quad (3.3)$$

where  $\overrightarrow{HD}(\hat{P}, Q)$  is the directional  $HD$  and  $p$  and  $q$  voxels in the masks  $\hat{P}$  and  $Q$ , respectively.

**Results** Fig. 3.3 shows the values of the DC and HD averaged among the subjects for each of the registration methods tested. ANTs performed best given the outliers showed by *elastix* (reported in the zoom out box in the bottom-right part of the figure), and was therefore used throughout the study.

**Discussion** All three registration methods performed well in these simple affine and intra-subject registration problems tested. Values are in line with previous studies, which identified successful registrations of large structures (such as the brain) with DC above 80% [72, 79]. Registration calls could be considered, therefore, satisfactory and precise.

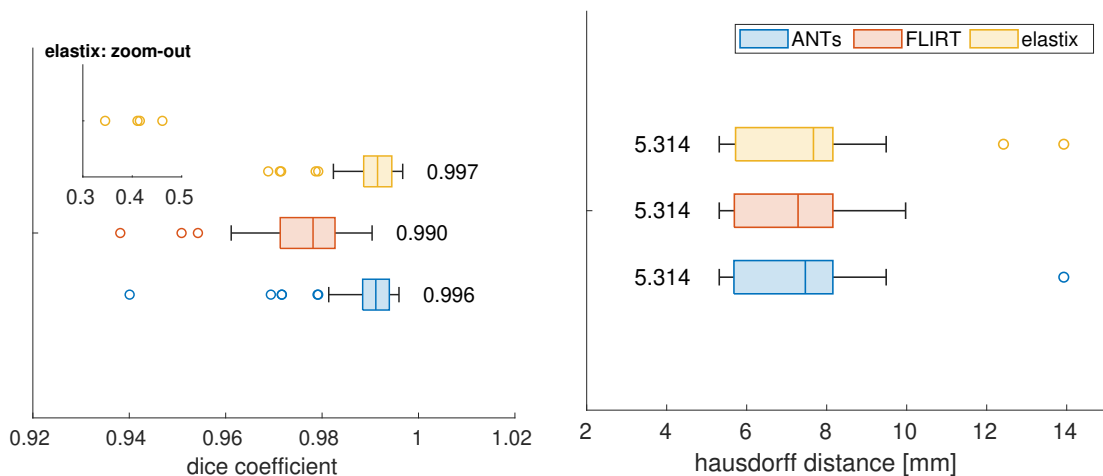


Figure 3.3: Boxplot of the DC (left) and the HD (right) representing the alignment of skulls after affine registration with the three algorithms tested (FLIRT in blue, ANTs in red and *elastix* in yellow). In the top-left corner of the DC plot a zoom-out box highlights few outliers for *elastix*. Annotated values display the best performance for each method, that is, maximum DC and minimum HD values.

Klein et al. [76] reported DC values above 60% in inter-subject registration problems of brain areas using FLIRT. Similarly, Ou et al. [40] reported DC values for FLIRT above 62% for similar inter-subject registration problems. FLIRT performed worse in the alignment of various abdominal organs, showing values of DC below 50% [72]. Finally, Visser et al. [125] reported similar performance of FLIRT, linear ANTs and linear *elastix* on few normalisation problems of low grade brain gliomas, with values of DC above 70% and HD below 5 mm.

A limitation of the study was the lack of expertly drawn landmarks, which would have given a better estimation of the error in the alignments [123]. Automatic skull segmentation was used, therefore it was not possible to assess the accuracy of the extracted boundaries, which had to be considered correct. This was evident in the same optimal values of HD between methods, that is 5.314 mm. This was related to imperfections in the generated masks, which were captured by the maximum operation in the HD calculations.

### 3.4 Deformable Registration: Optimisation

Once the initial conditions of deformation are set, differences between scans are only related to the mechanical deformation of the soft tissues, making the output field of the deformable registration the desired displacement field. Given the comparable magnitude of PBS to the resolution of the scans, accuracy of DVC measurements of displacements below the resolution relies on the smoothness constraints imposed onto the deformation field and the optimisation process during the registration call. This section shows the efforts that were made to measure the error related to the measurements of displacement.

**Methods** Three best performing deformable registration algorithms for medical imaging were optimised and then compared in order to gauge their accuracy in measuring a synthetic displacement field replicating PBS. As introduced in Section 2.4, the extensive comparisons by Klein et al. [76], Ou et al. [40] and Murphy et al. [71] put DRAMMS [35], SyN [69] and *elastix* [44] at the top for best performance. These methods have been proven in the literature to capture both small and large deformations, without any *a-priori* information on the mechanical response of the deforming tissues [120, 126].

A local and flexible transformation model was selected for the methods, that is, B-spline. Apart from showing good performance [43, 80], its support is local, in order to have the flexibility to follow the spatial variations of the deforming soft tissues. Diffeomorphism was also considered a good property of the transformation model, as it safe to assume that biological tissues deform smoothly under the effect of load [40]. The minimal assumptions on the estimated deformation field make these methods the best tool to capture data to use for the unbiased design and verification of any mathematical models to use for the intra-operative correction of surgical trajectories [26, 36].

A biomechanically plausible displacement field was generated through a biofidelic finite element (FE) simulation of PBS, based on a brain mesh extracted from the Montreal



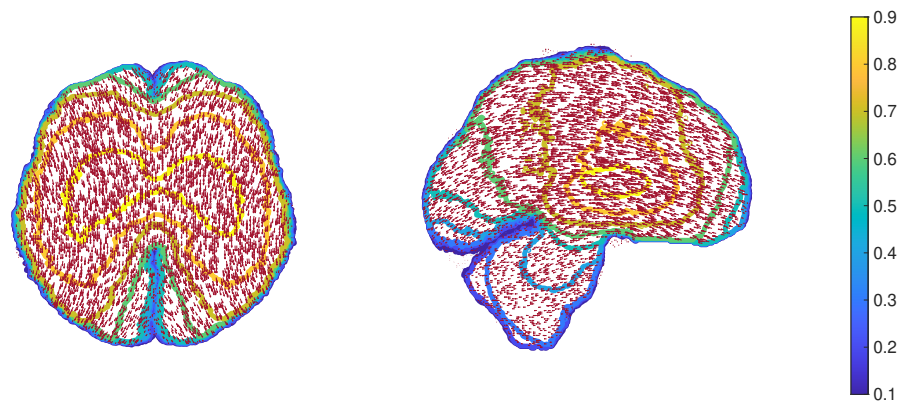


Figure 3.4: Axial (left) and sagittal (right) views of the synthetic displacement field used for the evaluation of the accuracy of the measurements of PBS. Length of vectors have been scaled for visualisation purposes: their magnitude is represented by the underlying contour plots (in [mm]).

Neurological Institute-Hospital 152 (MNI152) standard atlas [127] (Fig. 3.4). The FE method is a computational tool aimed at obtaining an approximate solution to the system of equations describing the mechanical behaviour of an object, given its mechanical response and geometry, as well as boundary, loading and initial conditions. It consists in the sub-division of the domain into smaller simple parts, called finite elements, forming the mesh. An approximate solution to the problem is solved at each finite element [128, 129]. The complex system of equations is then retrieved by assembling all the smaller solutions at finite elements. More information on the FE model used in this chapter can be found in the doctoral thesis by Nicholas Bennion [27]. This displacement field was characterised by a magnitude of  $0.60 \pm 0.26$  mm, azimuth angle of  $-89.70 \pm 11.98^\circ$  and elevation angle of  $1.27 \pm 11.46^\circ$ . The warp field from the MNI152 standard space was then morphed to the specific anatomy of each participant and applied to the supine scans of the 8 subjects [130] (further details in Section 4.2) and these registered back to the original using each of the selected methods.

Given the extensive literature on brain registration, parameters were varied around the default values recommended by developers. Parameters controlling for the transformation model, the similarity measure and the regularisation in the calculations were

optimised, leaving the others to default values in order to reduce the number of combinations to test (Table 3.3). Given the simple monomodal and intra-subject nature of the registration task, variations of cross-correlation were chosen as a similarity measure for all methods. Computations were run on a cluster at Cardiff University Brain Research Imaging Centre (CUBRIC).

Specific to the call to DRAMMS, regularisation weights were varied between 0.1 (aggressive fitting) and 0.25 (smoother deformations). Knot spacing for the free form deformation model was varied between 3 and 9 voxels (2.4 mm and 7.2 mm) [49]. Between 3 and 7 samples were drawn in the optimisation process along each direction and their diagonal, giving a total of 55 and 127 samples (in a neighbour that depends on the selected Gabor scales), respectively.

Regarding the call to SyN, knot spacing of the B-spline transformation model [80] at the top of the four multiresolution levels was varied between 16 mm and 33 mm (final knot spacing between 2 mm and 4.125 mm at original resolution). Gradient step controlling for the extent of movement of control points after each iteration was varied between 0.05 and 0.3, where small values represent small advancements. Radius of the similarity window was varied from 1 to 6 voxels, defining regions of  $2 \cdot radius + 1$  voxels (that is, between 26 and 2196 voxels), respectively.

Finally, for *elastix*, the tested final grid spacing ranged from 2 mm to 8 mm, with scaling factors of 8, 4, 2, 1 over the four resolution levels. Between 1000 and 2500 random samples were drawn from a cubic region with side length between 30 mm and 70 mm, giving regions made of 52734 and 669921 voxels.

Error metric used was the mean norm of the error vector (MNE) [120, 131]:

$$MNE = E_{\mathbf{x}} [\| \mathbf{T}_{gt}(\mathbf{x}) - \mathbf{T}_e(\mathbf{x}) \|], \quad (3.4)$$

where  $\mathbf{T}_e(\mathbf{x})$  is the estimated displacement field via deformable registration and  $\mathbf{T}_{gt}(\mathbf{x})$  the ground truth representing PBS,  $\mathbf{x}$  is the original position of voxels in a region of

Method	Parameter	Values
DRAMMS	samples in optimisation	3, 5, 7
	regularisation weight	0.1, 0.15, 0.2, 0.25
	final knot spacing [vxls]	3, 5, 7, 9
SyN	base knot spacing	16, 19, 23, 26, 29, 33
	neighbourhood radius [vxls]	1,2,3,4,5,6
	step update	0.05,0.1,0.17,0.25,0.3
<i>elastix</i>	final grid spacing	2 4 6 8
	spatial samples	$1e^3$ $1.5e^3$ $2e^3$ $2.5e^3$
	region size	30 40 50 60 70

Table 3.3: Values of the parameters trialled in the optimisation of each registration methods.

interest and  $E_x$  the expected value over the voxels at some ROI.

The choice of the optimal parameter set was based on both pair-wise surface plots of MNE values and on the frequency of individual parameters' values in optimal calls (that is, corresponding to error values below the 5<sup>th</sup>-percentile). First, sensitivity analysis via Gaussian emulation (GEM-SA software [132]) was used to assess the influence of parameters on the error metric and identify the most influential parameters. Surfaces were then extracted by fitting a Gaussian process regression model to the MNE values via MATLAB. Optimal values of the hyperparameters of the Gaussian process were automatically optimised during the call. The generation of pair-wise surfaces required averaging of MNE values between all the other parameters not represented in the surface. Therefore, the use of the frequency of individual parameters in calls characterised by MNE below 5<sup>th</sup>-percentile as additional representation was motivated by the absence of any averaging in the calculations. When reaching a plateau the parameter set closer to the default parameters or that was associated with lower degrees of freedom was chosen [17].

**Results** Fig. 3.5 shows the boxplot of the distribution of the error metric for all registration calls at superficial (meninges, GM and WM) and deep (ventricles, STN and

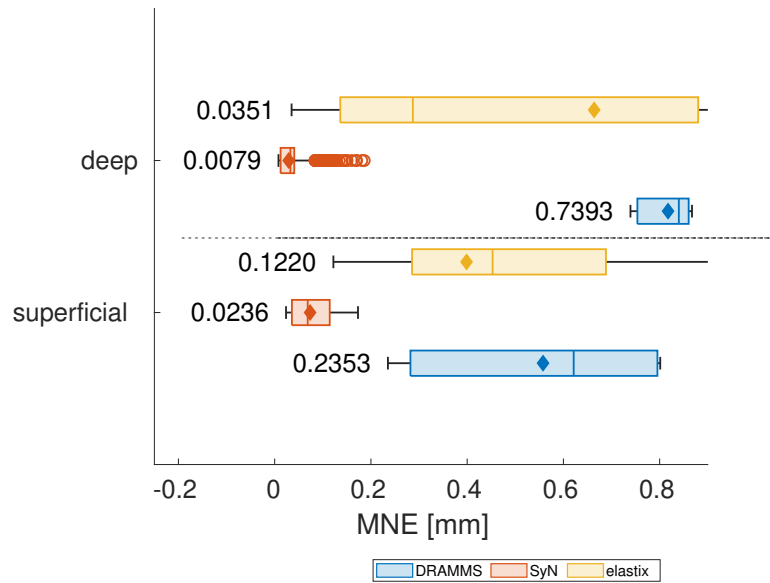


Figure 3.5: Boxplots of the mean norm error (MNE, in [mm]) for each method (DRAMMS in blue, SyN in red and *elastix* in yellow). Annotated values display the best performance, that is, the minimum MNE value. Top row shows results for the superficial (including meninges, GM and WM), whereas bottom row for deep (including Vent, STN and Put) brain areas. For reference, diamonds indicate the performance of the methods with the specific default parameters.

putamen) ROI. The 5<sup>th</sup>-percentiles of MNE were 0.258 mm, 0.010 mm and 0.110 mm for DRAMMS, SyN and *elastix*, respectively. SyN showed very little variability in MNE values, with an inter-quartile range of 0.040 mm (7% of the average simulated displacement). DRAMMS showed a higher inter-quartile range 0.218 mm (36%), with the highest shown by *elastix* (that is, 0.550 mm, 92%).

Heatmaps of the sensitivity analyses are reported in Fig. 3.6, 3.9 and 3.12, whereas surface plots are reported in Fig. 3.7, 3.10 and 3.13. Finally, each group of plots ends with the histogram of the frequency of parameters' values in optimal registration calls, that is, calls that lead to MNE below its 5<sup>th</sup>-percentile (Fig. 3.8, 3.11 and 3.14).

Table 3.4 shows the optimal parameter set for each method. MNE values at superficial ROI with optimal parameters were  $0.5597 \pm 0.2265$  mm,  $0.0743 \pm 0.0412$  mm and  $0.3983 \pm 0.2058$  mm for DRAMMS, SyN and *elastix*, respectively. Similarly, values

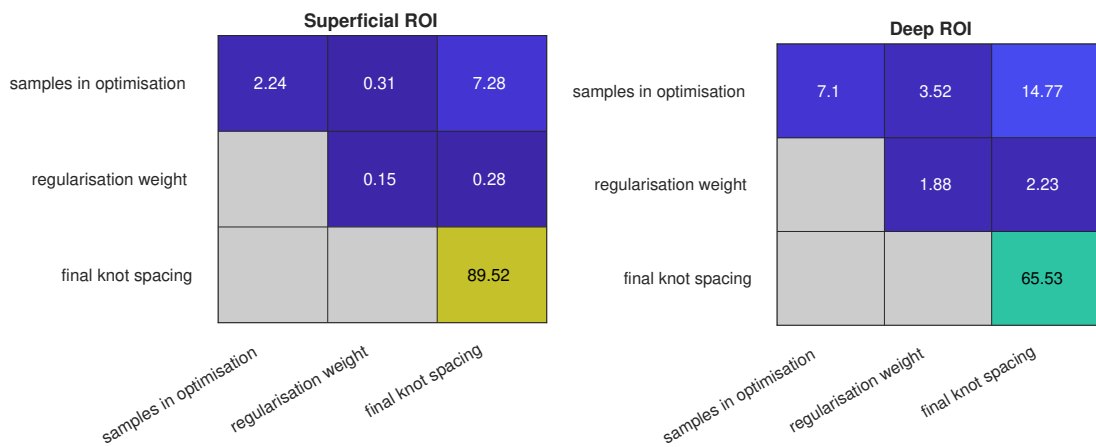


Figure 3.6: DRAMMS: heatmap of the individual and joint sensitivity on the error metric (MNE). On the left, results at superficial ROI (including meninges, GM and WM) and deep ROI (including ventricles, STN and Putamen). Values are percentages relative to the mean total variances ( $1.1662 \cdot 10^{-5} \text{ mm}^2$  at superficial ROI whereas  $6.34252 \cdot 10^{-8} \text{ mm}^2$  at deep ROI).

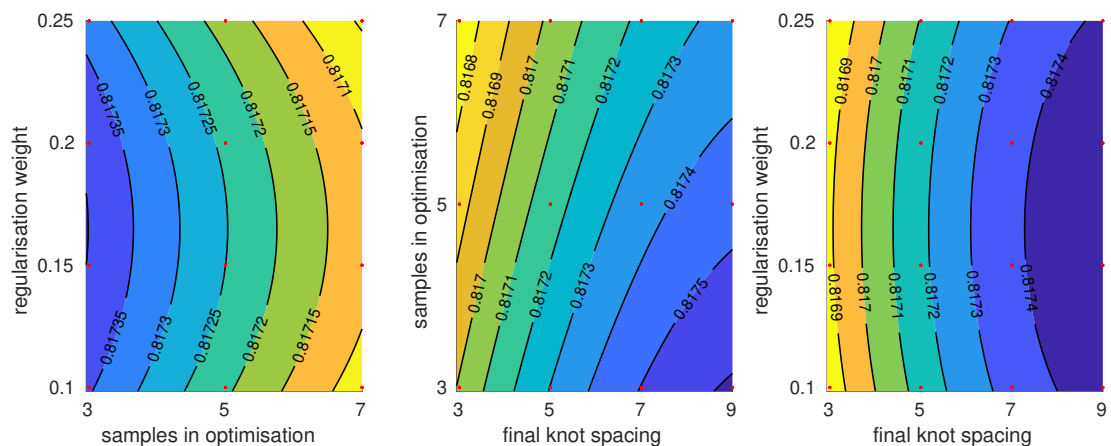


Figure 3.7: DRAMMS: surface plots showing the pair-wise distribution of the error metric (MNE, in [mm]) between the three most influencing parameters. Red dots represent query points.

at deep ROI were instead  $0.8172 \pm 0.0486 \text{ mm}$ ,  $0.0262 \pm 0.0114 \text{ mm}$  and  $0.2208 \pm 0.2116 \text{ mm}$ . SyN was therefore chosen for its favourable error statistics. The distribution of the error for the chosen parameters for one of the subjects is reported on an axial slice in Fig. 3.15 for the three methods. DRAMMS showed a general bias in the MNE values, whereas *elastix* showed small scattered areas of high MNE values.

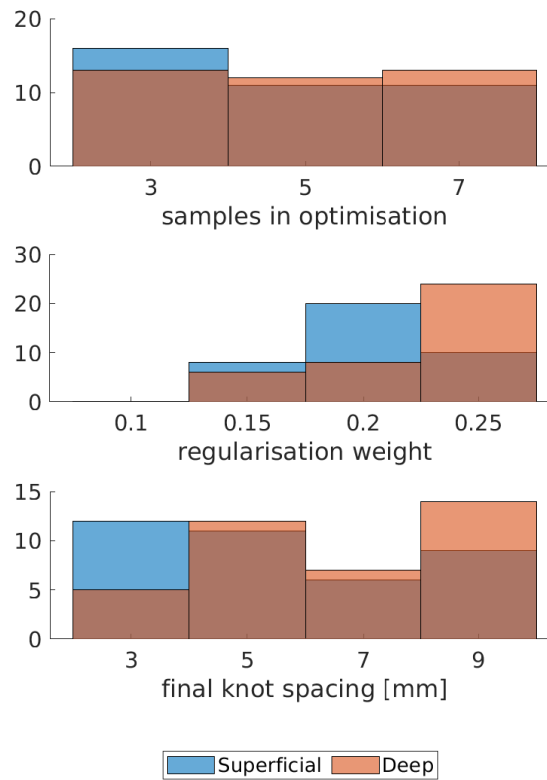


Figure 3.8: DRAMMS: histogram of the number of registration calls leading to MNE values below its 5<sup>th</sup>-percentile. Histograms are reported for the three most influencing parameters; in blue at superficial ROI (including meninges, GM and WM) and in orange at deep ROI (including Ventricles, STN and putamen).

**Discussion** SyN showed best performance in following a biomechanically plausible ground truth representing PBS: the optimal parameters were therefore used for the DVC measurements in Chapter 4. The chosen parameter set led to an average MNE of  $0.050 \pm 0.038$  mm in the brain area, which was considered acceptable, it being one order of magnitude smaller than the expected average PBS [17].

SyN and *elastix* showed good performance, with 5<sup>th</sup>-percentile MNE values of 0.010 mm and 0.110 mm, respectively. These two methods showed lower metric error in deeper regions, probably due to the smoother and more consistent distribution of the tissue deformation away from boundaries. DRAMMS, instead, showed a noticeable higher error, with a 5<sup>th</sup>-percentile MNE value of 0.258 mm.

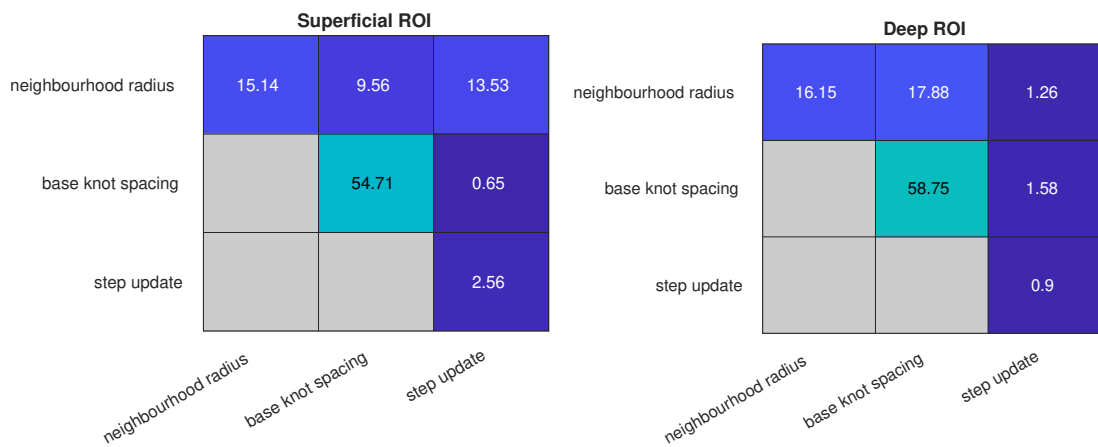


Figure 3.9: SyN: heatmap of the individual and joint sensitivity on the error metric (MNE). On the left, results at superficial ROI (including meninges, GM and WM) and deep ROI (including ventricles, STN and Putamen). Values are percentages relative to the mean total variances ( $7.54401 \cdot 10^{-6} \text{ mm}^2$ ) on superficial whereas  $4.11782 \cdot 10^{-5} \text{ mm}^2$  on deep ROI).

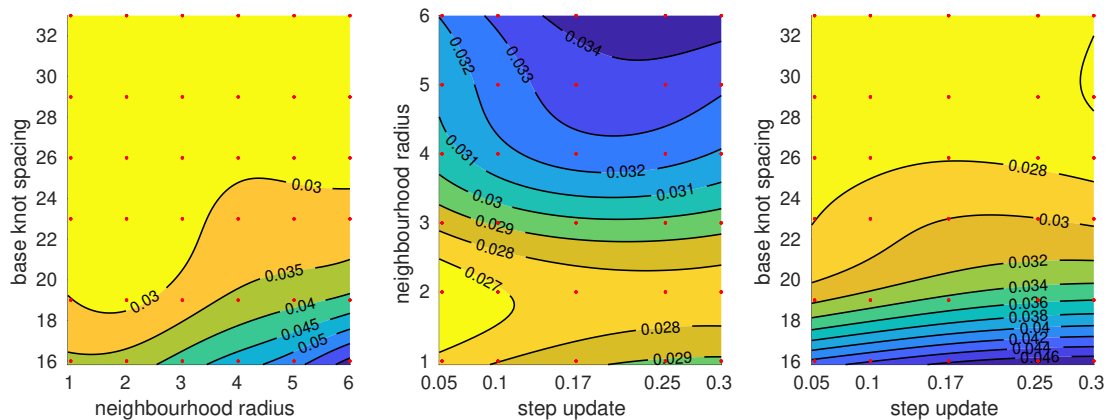


Figure 3.10: SyN: surface plots showing the pair-wise distribution of the error metric (MNE, in [mm]) between the three most influencing parameters. Red dots represent query points.

Little effect had the optimisation on the performance of SyN. It was necessary, instead, for *elastix* and DRAMMS, which showed the greatest inter-quartile range of MNE values. Regarding *elastix*, this could be related to the absence of a penalty term on the transformation model, such as a restriction on the bending energy of the transformation model. This left only knot spacing to control for the smoothness of the estimated deformation field. Indeed, this caused the small areas of high MNE values that can

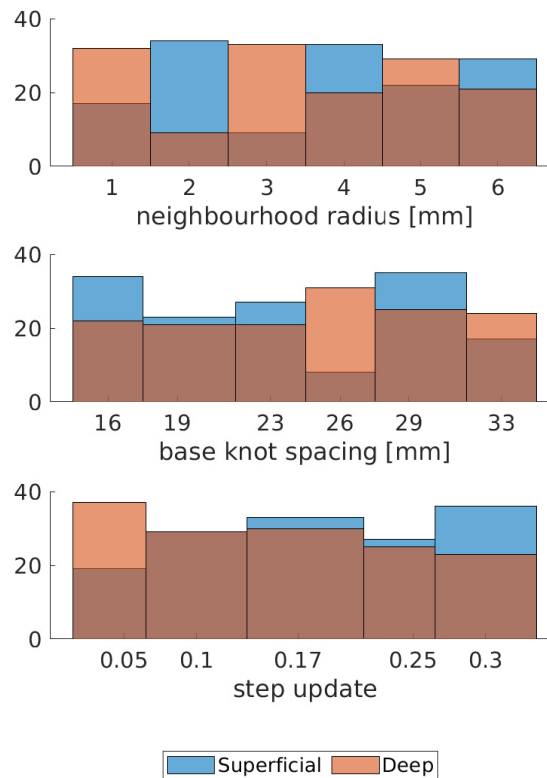


Figure 3.11: SyN: histogram of the number of registration calls leading to MNE values below its 5<sup>th</sup>-percentile. Histograms are reported for the three most influencing parameters; in blue at superficial ROI (including meninges, GM and WM) and in orange at deep ROI (including Ventricles, STN and putamen).

be noticed in the distribution of Fig. 3.15. This confirms the results obtained in the EMPIRE10 challenge [71], where methods were tested for the positiveness of the determinant of the Jacobian of the output warps. *elastix* consistently scored 4<sup>th</sup> lowest (out of 34) in this test, in both phase 1 and phase 2. Given the smoothness of PBS, future developments will aim at including also a penalty term on the transformation model of *elastix*.

Grid spacing was the most critical parameter for all registration methods, explaining at least 50% of the variance in MNE values. Different were its optimal values between the methods, where smaller values were preferable for DRAMMS and *elastix*, whereas larger spacings for SyN. Regarding spatial distribution, frequency of parameter values



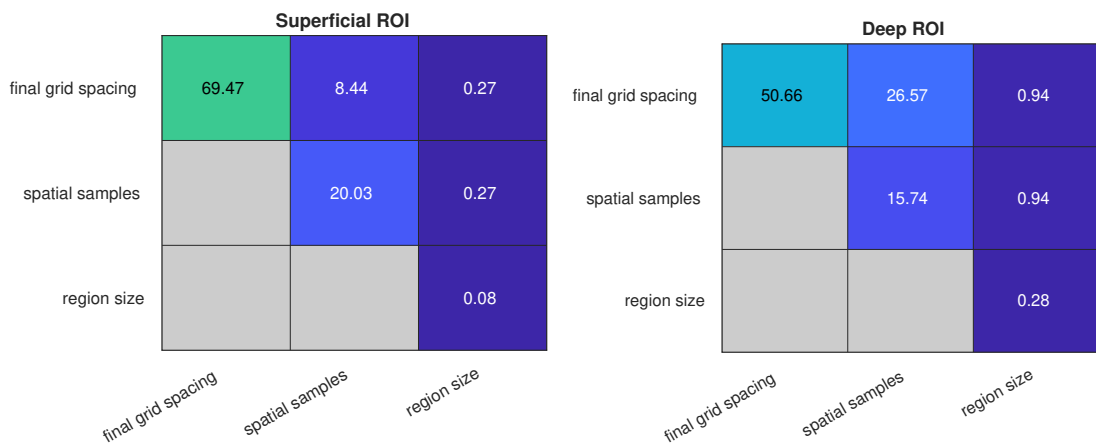


Figure 3.12: *elastix*: heatmap of the individual and joint sensitivity on the error metric (MNE). On the left, results at superficial ROI (including meninges, GM and WM) and deep ROI (including ventricles, STN and Putamen). Values are percentages relative to the mean total variances ( $0.0106621 \text{ mm}^2$  for superficial and  $0.0461161 \text{ mm}^2$  for deep ROI).

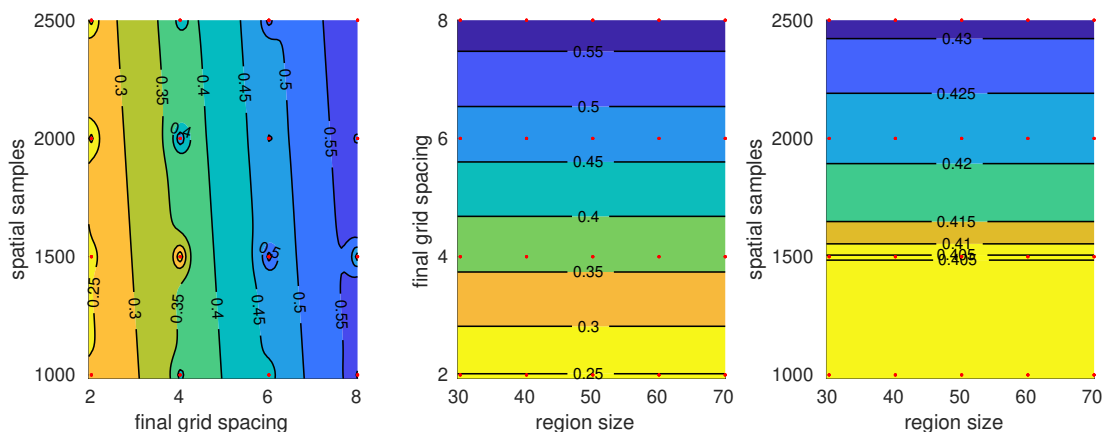


Figure 3.13: *elastix*: surface plots showing the pair-wise distribution of the error metric (MNE, in [mm]) between the three most influencing parameters. Red dots represent query points.

in registration calls below the  $5^{th}$ -percentile of MNE values showed that smaller grid spacings of the B-spline model were preferable at more superficial ROI. Larger control point spacing performed best in deeper regions confirming the more consistent and smoother deformation field in those regions.

Evaluating accuracy on synthetic data represents a best case-scenario [133], as synthetic

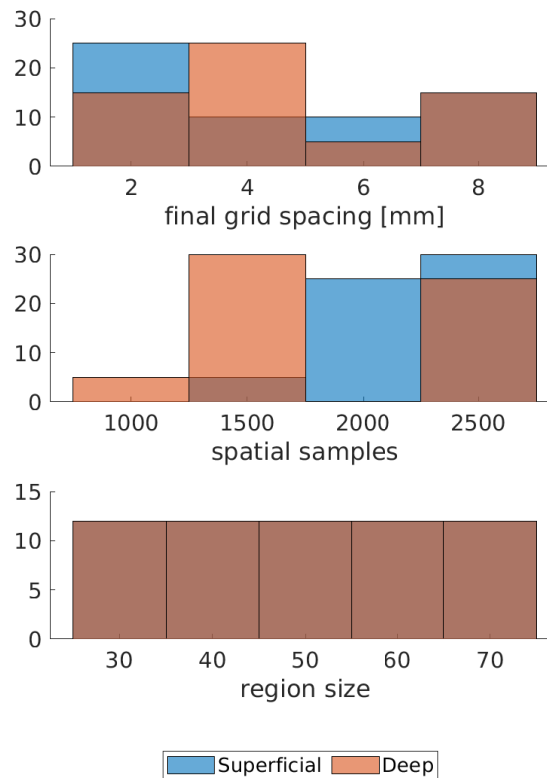


Figure 3.14: *elastix*: histogram of the number of registration calls leading to MNE values below its 5<sup>th</sup>-percentile. Histograms are reported for the three most influencing parameters; in blue at superficial ROI (including meninges, GM and WM) and in orange at deep ROI (including Ventricles, STN and putamen).

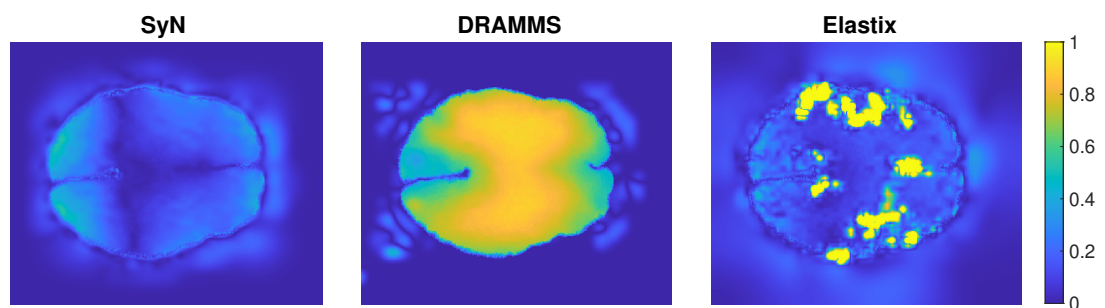


Figure 3.15: Distribution of the MNE for the best registration call for each method tested (that is, SyN on the left, DRAMMS in the centre and *elastix* on the right). Values are extracted over the brain area for one subject. Colour bar represents values in [mm].

Method	Parameter	Optimal value
DRAMMS	samples in optimisation	7
	regularisation weight	0.25
	final knot spacing	9
SyN	base knot spacing	29
	neighbourhood radius	3
	step update	0.05
<i>elastix</i>	final grid spacing	4
	spatial samples	1500
	region size	30

Table 3.4: Best parameter set for each registration methods.

warp field, interpolation and noise pattern cannot reproduce the realistic conditions fully. However, given the lack of an real ground truth to test the accuracy on and the lack of expertly placed fiducial landmarks, any further attempt in assessing the accuracy of the method was considered out of scope and a limitation of the study.

The study also lacked of an assessment of the effect of interpolation after initial registration on the estimated displacement fields. Its effect is mentioned in the literature on DVC measurements, but not extensively investigated [17, 20]. The study by Schreier et al. [134] reported favourable results of spline- and Fourier-based interpolation methods on 2D digital image correlation measurements, reducing the systematic error in the measurements.

## Summary

This chapter has shown the efforts that were made to measure the sources error affecting the DVC measurements, identified as MR distortions, initial skull alignment and inaccuracy in the call to the deformable registration. The analysis allowed the identification of the best performing method, alongside the optimal parameter to be used in the DVC measurements Chapter 4.

First, MR distortions are known to deform the morphology of a sample object in an MR scanner; this heterogeneous warp is to be considered as a systematic error affecting the DVC measurements. In the case of two individuals, differences between scans of the same subject imaged in scanners with different magnetic field strengths were captured via deformable registration. *Gradunwarp*, a popular correction method in the neuroimaging community, showed lowest error ( $1.27 \pm 0.11$  mm), relative to the scanner default compensation method.

As a second source of inaccuracy in the DVC measurements, initial skull registration was shown to have an average accuracy in DC values of 0.996 and a HD values of 5.314 mm. Any misalignment between rigid skeletal elements are captured as an additional component of deformation by the DVC measurements and considered as displacement of soft tissues.

Finally, error in the actual DVC measurements after optimisation led to an average error of  $0.0503 \pm 0.0385$  mm in the brain area. SyN showed superior performance relative to the other two deformable registration methods compared (that is, DRAMMS and *elastix*) in following a synthetic deformation field simulating PBS. SyN alongside the best parameter set identified were used in the following Chapter 4.

# **Brain Shift: Digital Volume Correlation**

## **Overview**

This chapter describes the methods used to capture positional brain shift (PBS) and the clinical significance of the measurements. The work carried out in this chapter contributes towards a larger over-arching research project involving other two complementary PhD works, which objective was to capture or generate the deformation of PBS with different approaches, so to facilitate the cross validation of the methods and the obtained results. One of the other two projects aimed to generate a finite element model of the head for the accurate simulation of PBS [27]; the other, instead, aimed to manufacture a brain phantom that could reliably replicate PBS [135]. The work of this chapter aims to capture the actual PBS from healthy individual to validate the other two models of PBS investigated. It adds to the previous knowledge on PBS by providing volumetric measurements of the deformation of the brain tissue at surgically relevant regions of interest in both subject-specific and average spaces; by investigating the compressibility of the brain tissue; by exploring the influence of intra-cranial geometry and head orientation on PBS. The work presented in this chapter is part of the the main body of the following peer-reviewed paper:

Zappalá, S., Bennion, N. J., Potts, M. R., Wu, J., Kusmia, S., Jones, D. K.,

Evans, S. L., & Marshall, D. (2021). Full-field MRI measurements of *in-vivo* positional brain shift reveal the significance of intra-cranial geometry and head orientation for stereotactic surgery. *Scientific Reports*, 11(1), 17684. <https://doi.org/10.1038/S41598-021-97150-5>.

Section 4.1 expands on the more generic introduction to the problem related to brain shift introduced in Section 3.1, with the findings in the literature regarding the general consensus on the pattern of deformation of PBS.

Section 4.2 introduces to the specification of the acquisition protocol and the participant recruitment. Section 4.3 describes the registration pipeline, beginning with the affine alignment to set the initial conditions of deformations, followed by the DVC measurements using the optimal parameter set identified in Section 3.4.

Results of the analysis of deformation are shown in Section 4.4, which clinical implications are then discussed in Section 4.5.

## 4.1 Introduction

As introduced in the previous chapter (Section 3.1), positional brain shift (PBS), the sagging of the brain under the effect of gravity, is comparable in magnitude to the margin of error for the success of stereotactic interventions ( $\sim 1$  mm). This non-uniform shift due to slight differences in head orientation can lead to a significant discrepancy between the planned and the actual location of surgical targets.

The pattern of deformation in the physiological case is reported to be far from rigid, with local variations even between individual sulci and gyri of the cortex [4]. The regional variability of PBS is significant, as the momentum generated by gravity is non-uniformly distributed [4] and the tissue properties vary among structures, due to different histological compositions between grey and white matter tissues [5]. PBS has been shown to be generally localised in deep, central brain regions (e.g., basal

ganglia), which are the main targets for IGNS-based interventions [4–6]. Considering prone to supine changing of positioning, PBS has been shown having a rotational component in the sagittal plane, with the centre of rotation located around the brainstem region [4, 5, 136, 137]. Different boundary structures limiting such deformation have been reported, such as the falx, the tentorium, as well as vascular, endural and dural elements [4, 5, 136, 137]. The brainstem, apart from acting as a centre of rotation, was also shown to pull the brain tissue depending on the angle of the neck, even if this contribution was reported to be secondary to the effect of gravity at neck flexion between 20° and 30° [107, 138].

As previously mentioned in Chapter 3, these conclusions were drawn based on observations mostly limited to surfaces [4, 5] or to measurements at specific locations [7, 8], failing to capture the local and global deformation of the tissue. To expand on the contributions previously introduced, the study aimed to acquire and analyse a dense set of full-field measurements of the *in-vivo* deformation of brain tissue resulting from a prone-to-supine change in head orientation. Understanding the mechanics in normal physiological conditions (i.e., in the healthy brain) is the first step before modelling the more challenging shift induced by pathology or surgical manipulation. Deformable image registration was used to extract the displacement field between skull-aligned magnetic resonance (MR) scans representing the different states of deformation of the tissue (that is, via digital volume correlation (DVC)). This study adds to the previous knowledge on PBS [4–6, 8] with the following contributions:

- provision of a dataset of accurate volumetric measurements at various regions of interest (ROI) and surgically relevant structures;
- normalisation of data from different subjects to a common reference space allowing an inter-subject analysis on a voxel-wise basis.
- investigation of the local compressibility of the brain, in particular to further test the hypothesis that the brain is slightly compressible with spatial heterogeneity in compressibility;

- exploration of factors influencing PBS, such as intra-cranial geometry and head orientation.

## 4.2 Study Definition and Ethics

This study was carried out at the Cardiff University Brain Research Imaging Centre (CUBRIC), Cardiff University. The aim of the protocol was to acquire MRI images representing the differences in the brain morphology between prone and supine positions, that is, PBS. This study was approved by the Ethical Committee of the Cardiff University School of Psychology, United Kingdom. All methods were carried out in accordance with the relevant guidelines and regulations. Informed consent was given by all participants before scanning.

The initial aim was to scan around 10 healthy people for each of 5 decades of life (20-30, 30-40, 40-50, 50-60, 60-70 years), in order to characterise the variability of brain shift among different life spans. However, the difficult subject recruitment required a prioritisation of the age ranges 20-30 and 50-70. Then, the closure of the CUBRIC centre due to the COVID-19 outbreak impacted the completion of planned experiments. The study was therefore considered completed with 13 subjects in the age range 20-30 and 12 in the range 50-70, allowing for a statistical analysis between these two population samples.

In order to avoid any pathological conditions to the brain tissue affecting its morphology or mechanical response, subjects were excluded from the study in case of (self-reported):



- Alcohol intake of more than 30 units/week or intake of more than 10 units within 48 h prior to scanning. A unit of alcohol is equal to 10 ml of pure alcohol and is roughly equivalent to a glass of wine (125 ml) or a single measure of spirits (25 ml) [139].
- History of alcohol or drug abuse [139].



- History of severe head trauma requiring medical attention [139].
- History of neurosurgical procedure [140].
- History of neurological, psychiatric disease or cognitive difficulties [139, 141].
- Risk factors for stroke, such as diabetes, cardiovascular disease or hyperlipidaemia [139, 141].
- Any contraindication for MRI scanning [140].

Posters (Figure 4.1) describing the study were shown in University departments and public places, once the approval was obtained by the corresponding gatekeeper. Recruitment was also carried through e-mailing lists in each of the University department, prior to approval by the corresponding gatekeeper. An incentive of 10 pounds per hour was offered to each participant. The amount was paid according to the going rate amongst similar kinds for study.

A diagram of the acquisition protocol is reported in Figure 4.2. The total required time, considering participant welcoming and scanning setting-up, was maximum 2 hours. The scanner used was a Siemens 3T PRISMA (Siemens Healthcare, Erlangen, Germany). Subjects were scanned initially in a prone position (20 min in total) where diffusion-weighted followed by MPRAGE T1-weighted [142] scans were acquired. Padding on cheeks and the forehead were used to make the subject comfortable in such prone position, taking care not to reduce the access to air. The time taken to position the subject comfortably in the scanner guaranteed that the tissue had displaced fully towards the frontal part of the skull before scanning. This setting was tested successfully in a previous pilot study based on T1w MPRAGE scans of 8 subjects scanned in a Siemens 7T MAGNETOM (Siemens Healthcare, Erlangen, Germany) scanner. The results of the pilot showed no further deformation of the brain tissues in 8 healthy participants after 8 mm from swapping head orientation. No additional material was used, but for the standard MRI imaging.

# Is Your Brain Deforming Right Now?

Make an impact on the future of image-guided neurosurgery

We are looking for **healthy volunteers aged 50-70** for a study aimed at imaging the shape of the brain under different orientations of the head

---

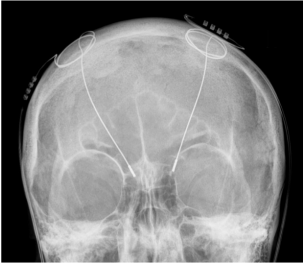
Participants are asked to lie **face-down** in an MRI scanner for around **20 minutes** whilst images of the head are acquired, then **face-up** for around **40 minutes**. The study lasts a maximum of **2 hours** and takes place at the Cardiff University Brain Research Imaging Centre (**CUBRIC**).

Participants will be offered **£20** as a thank-you for their time.

---

The study is based on the teamwork of four PhD students under the supervision of **Prof. Sam Evans** (School of Engineering), **Prof. Derek Jones** (CUBRIC) and **Prof. David Marshall** (School of Computer Science and Informatics). The work is part of a strategic alliance between Cardiff University and **Renishaw PLC**.


---




The results of the project will help in the design of a smarter graphical system for surgical navigation. The overall aim is to improve the delivery of electrodes for deep brain stimulation (e.g., **the treatment of Parkinson's Disease**) or the targeted delivery of drugs to the brain tissue (e.g. **Cancer Therapy**).

---

If you would like to take part or would like further information, please contact **Stefano Zappalà** at: **[zappalaS@cardiff.ac.uk](mailto:zappalaS@cardiff.ac.uk)**



CUBRIC



apply innovation™

Bottom picture by Hellerhoff [CC BY-SA 3.0 (<https://creativecommons.org/licenses/by-sa/3.0/>)], from Wikimedia Commons

Figure 4.1: Poster used for the recruitment targeting participants in the age range 50 to 70 years of age, as individuals in the 20-30 years age range could be easily found in the academic setting.

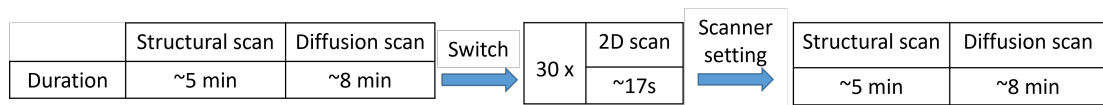


Figure 4.2: Schematic of the acquisition protocol for the study carried out in the 3T scanner. Duration of each acquisition sequence is reported below for prone scanning, on the left; and for supine scanning (right), after switching participant position.

After asking subjects to move to a supine position, 30 2D spoiled gradient-recalled echo (FLASH) scans (including 2 sagittal, one axial and one coronal slices) were acquired at every 17 s, in order to capture brain shift in the first 8 min of deformation. Then, additional T1-weighted MPRAGE followed by diffusion-weighted scans were acquired.

Acquisition parameters for both pilot study (7T) and main study (3T) are reported in Table 4.1. Manual shimming was run on the 7T scanner by an experienced MR physician, whereas the vendor’s automatic shimming was used for the 3T data. 3D FatNav correction was applied to the 3T scans, which consists in a retrospective correction of the subject micro-movements (that is, root-mean-squared displacement of 1.08 mm and rotation of  $0.84^\circ$ ) tracked during scans via additional accelerated fat-selection 3D scans [22].

For both prone and supine acquisitions, care was taken to position the head of each participant consistently in the head coil and to locate the latter at the isocentre of the magnetic field, via a laser module built in the system.

Anonymised demographics were stored alongside the scans, such as age, height and weight to allow statistical analysis. With the aim of sharing scans and demographic information publicly after publication of the work, consent from each subjects was obtained and their information not shared unless consent was given. All the recommended guidelines for the anonymisation of the scans were followed: all sensible information in the headers was deleted and the faces of participants blurred via *mri\_deface* from the FreeSurfer library [143] prior to sharing the data publicly.

	<b>MPRAGE at 7T</b>	<b>MPRAGE at 3T</b>	<b>FLASH at 3T</b>
<b>TR</b>	2200 <i>ms</i>	2300 <i>ms</i>	8.6 <i>ms</i>
<b>TE</b>	2.93 <i>ms</i>	2.88 <i>ms</i>	4 <i>ms</i>
<b>Flip Angle</b>	7°	9°	20°
<b>FOV</b>	256x318	256x256	256x256
<b>Slices</b>	242	256	1
<b>Resolution</b>	0.8x0.75x0.75 <i>mm</i> <sup>3</sup>	1x1x1 <i>mm</i> <sup>3</sup>	1x1 <i>mm</i> <sup>2</sup>
<b>Scan Time</b>	4m 28s	5m 32s	17 s
	<b>DWI at 3T</b>		
<b>TR</b>	3500 <i>ms</i>		
<b>TE</b>	80.6 <i>ms</i>		
<b>Flip Angle</b>	90°		
<b>FOV</b>	154x154		
<b>Slices</b>	84		
<b>Resolution</b>	1.5x1.5x1.5 <i>mm</i> <sup>3</sup>		
<b>Scan Time</b>	8m 30s		
<b>Diffusion Directions</b>	9 B0 blip-up 4 B0 blip-down 20 at 200 <i>s/mm</i> <sup>2</sup> 20 at 500 <i>s/mm</i> <sup>2</sup> 30 blip-up at 1200 <i>s/mm</i> <sup>2</sup> 30 blip-down at 1200 <i>s/mm</i> <sup>2</sup> 60 at 2400 <i>s/mm</i> <sup>2</sup>		

Table 4.1: Acquisition parameters for the structural sequences on the top row, whereas for diffusion sequence on the bottom row.

## 4.3 Methods

**Data Acquisition** The following initial work is based on only eleven (7 male and 4 female) healthy young adults from the population sample scanned (average age: 25.18 years; range: 22-32 years). This was chosen to limit the confounding effect of age [4], leaving the comparison of the two acquired population samples as future directions. The first six participants were scanned as part of the pilot study in the Siemens 7T MAGNETOM scanner (Siemens Healthcare, Erlangen, Germany); the last five were scanned in the Siemens 3T PRISMA. This initial study consisted of the comparison of the T1-weighted MPRAGE scans, leaving the 2D scans and the diffusion-weighted

scans for future investigations.

**Data Pre-processing** In order to reduce any residual MR distortions, correction with the software *gradunwarp* [118] was applied (standard for the multi-site Human Connectome Project [117]). It showed better performance relative to the scanner-default distortion correction on two participants who were scanned in both 7T and 3T scanners (Section 3.3). Scans were corrected for low-spatial frequency intensity inhomogeneities with the unified segmentation module of the Statistical Parametric Mapping (SPM) [144] toolbox [145]. Finally, a semi-automated segmentation process was carried out to extract the skull and brain masks, where the brain extraction tool (BET) command of the FSL software library [122] was used and the segmentations thus-obtained were amended manually where necessary via Seg3D (Scientific Computing and Imaging Institute (SCI)).

**Digital Volume Correlation** Prior to deformable registration, images were aligned at the level of the skull in order to define the initial conditions of deformation. The prone scan of each participant was registered to the supine one, which served as the subject-specific reference volume. Registration was limited to the skull to avoid any bias induced by PBS; affine rather than rigid transformation was chosen to reduce any residual distortions [90, 92]. The ANTs [79] affine registration method was used as it showed better performance than two other popular registration software in correcting for some combinations of rotations and translations (Section 3.3).

The warp field resulting from a deformable registration call of the skull-aligned prone and supine images depicted the displacement field due to PBS alone [5]. The symmetric image normalisation (SyN) [79] method was used: it showed better performance than two other state-of-the-art registration packages for neuroimaging in following a biofidelic synthetic deformation field representing PBS (Section 3.4). Parameters were left as default apart from those controlling similarity measure (cross-correlation) and the transformation model (BSpline [80]) which were optimised against the ground truth; the

best set gave an error of  $0.0503 \pm 0.0385$  mm in the brain area, one order of magnitude smaller than the expected magnitude of PBS.

**Spatial Normalisation** In order to conduct an inter-subject (group) analysis, all supine scans were spatially normalised (that is, deformably registered) to the Montreal Neurological Institute-Hospital 152 (MNI152) standard space (isotropic resolution  $1 \text{ mm}^3$ ) [127] with the same SyN software. Vectors of each displacement field were re-oriented (ANTs suite) according to the global rotation matrices representing the specific head orientations of participants relative to the standard space; this guaranteed the correspondence between deformation and head orientation following normalisation [130]. An average displacement field was extracted with the corresponding inter-subject variability that would otherwise be lost when measuring PBS on templates extracted after averaging images between participants [5].

Furthermore, the normalisation allowed the derivation of the orientation of each participant's head in the scanner (i.e., direction of gravity) relative to the neutral supine position represented by the MNI152 standard space, as well as the antero-posterior diameter (APD:  $176 \pm 6$  mm) and the maximum cranial breadth (MCB:  $137 \pm 6$  mm) [4]. Any correlation between these factors and PBS was evaluated using the Spearman correlation coefficient [146].

**Analysis of Deformation** Statistics were computed both globally and locally with MATLAB R2020b (Mathworks, Natick, MA). Results presented throughout the study are either reported in Cartesian or in spherical coordinates. For the former, a RAS (right-anterior-superior) convention was used. For the latter, the azimuth angle represented orientation of vectors on an axial plane relative to the positive axis of the left-right (L-R) direction; elevation angles represented orientation on a sagittal plane relative to the positive axis of the posterior-anterior (P-A) direction.

A ROI-wise analysis was performed after normalisation to infer the anatomical vari-

ability in PBS. Atlases used include: Harvard Oxford (HO) [147], the Atlasing of the Basal Ganglia (ATAG) [148] and the International Consortium for Brain Mapping (ICBM) [149] atlases. These included deep white matter structures as well as ventricles and basal ganglia, which are relevant surgical targets for IGNS-based interventions [150–152].

Finally, the Green-Lagrange strain tensor [153] was evaluated at each voxel in the brain in order to interpret the deformation in a differential manner, that is, discarding any rigid body displacement. The strain tensor,  $\mathbf{E}$ , was extracted as:

$$\mathbf{E} = \frac{1}{2} (\mathbf{F}^T \mathbf{F} - I), \quad (4.1)$$

$$\mathbf{F} = \frac{\partial \mathbf{u}(\mathbf{x})}{\partial \mathbf{x}} + I, \quad (4.2)$$

where  $\mathbf{x}$  is the voxel position in the original configuration,  $\mathbf{u}(\mathbf{x})$  the deformation field,  $I$  the identity matrix and  $\mathbf{F}$  the deformation gradient.

To further investigate the role of the tissue meso-architecture, strain tensors were partitioned into a hydrostatic component representing volume change (at small strains):

$$E_{hyd} = \frac{E_{xx} + E_{yy} + E_{zz}}{3}, \quad (4.3)$$

where  $E_{xx}$ ,  $E_{yy}$ ,  $E_{zz}$  are the three diagonal elements of the strain tensor; and a deviatoric component representing shape change:

$$\mathbf{E}_{dev} = \mathbf{E} - E_{hyd}. \quad (4.4)$$

## 4.4 Results

**Subject Positioning** Fig. 4.3 shows head orientation among subjects as direction of gravity during scanning. Average  $\pm$  standard deviation of azimuth and elevation angles were, respectively,  $89.91 \pm 2.99^\circ$  and  $-9.86 \pm 8.90^\circ$  for prone, and  $-91.01 \pm 2.03^\circ$  and  $171.72 \pm 6.22^\circ$  for supine, showing an average neutral pan but slight upward tilt of the head in both prone and supine scans.

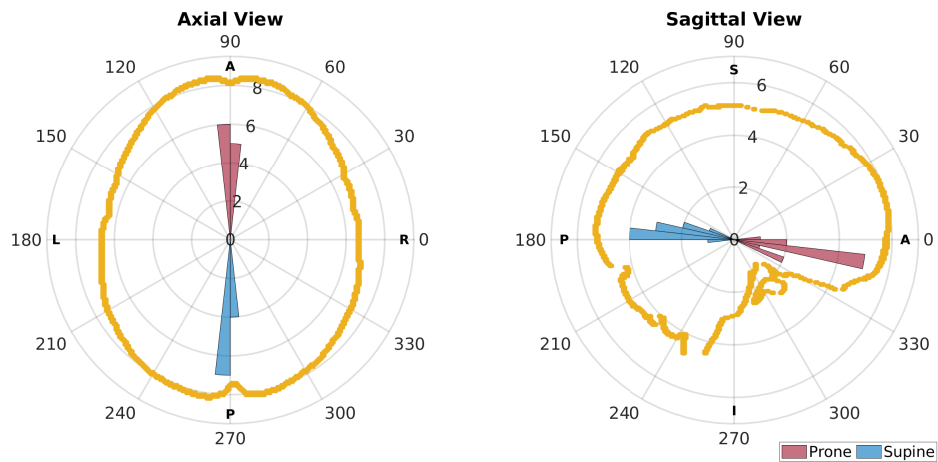


Figure 4.3: Polar histograms of the direction of gravity (i.e., head orientation of participants) during scanning. On the left, greater values of azimuth angle represent head of the participant turned right during scanning. On the right, higher values of elevation angle represent head of the participant tilted downwards during scanning. The shape of the skull from the MNI atlas is overlapped as reference for the neutral head orientation.

**Skull Alignment** Fig. 4.4 shows the resulted alignment of the skull from the prone scans onto the skull from supine ones.

**Analysis of Deformation** The most significant component of displacement was P-A as reported in Table 4.2. With respect to the average, the inferior-superior (I-S) component showed greater variability among subjects. A consistent shift towards left can be noticed in the L-R component. Fig. 4.5 shows PBS as a displacement field. An overall translational component towards the posterior part of the skull can be seen, with



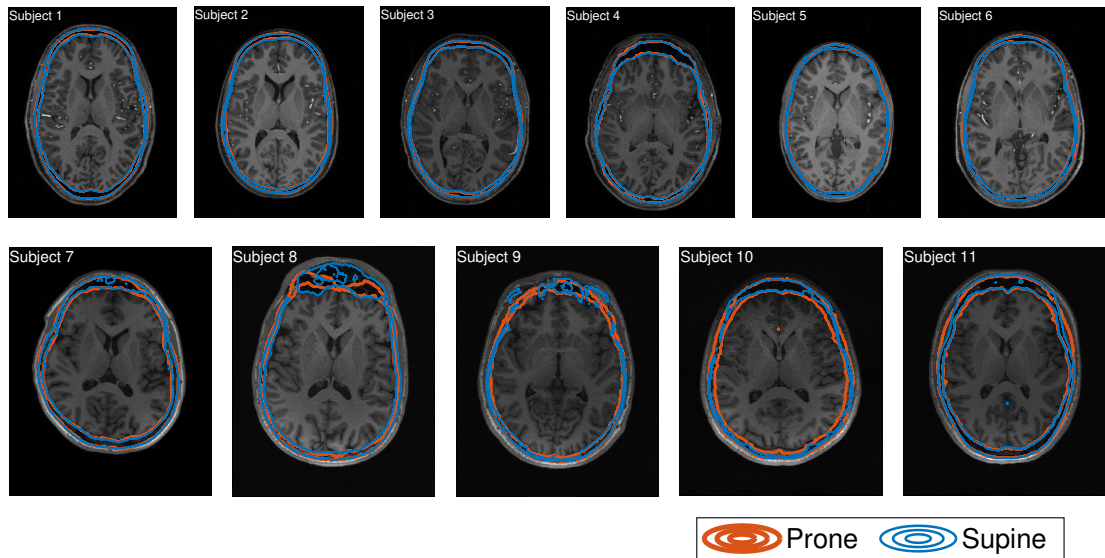


Figure 4.4: Axial views of the initial alignment of the pelvic elements between supine (blue), prone (orange) scans.

significant local variability. Displacement was greater in deeper (compared to more superficial) regions and in particular further away from anatomical boundaries such as the falx cerebri (midline), the tentorium cerebelli (just below the cerebrum) and the meninges (periphery). Whilst inward displacement can be seen in frontal regions, movement was negligible more posteriorly. The previously observed shift to the left can be seen here in the axial distributions of Fig. 4.5; this lateral displacement correlated weakly with brain volume ( $p=0.07$ ,  $r=-0.58$ ), showing a greater leftward deformation with bigger brain volumes.

	Mean $\pm$ standard deviation	Inter-subject variability
<b>Left-right</b>	$-0.09 \pm 0.23$ mm	0.19 mm
<b>Posterior-anterior</b>	$-0.2 \pm 0.36$ mm	0.26 mm
<b>Inferior-superior</b>	$0.10 \pm 0.33$ mm	0.3 mm
<b>Magnitude</b>	$0.57 \pm 0.34$ mm	0.41 mm

Table 4.2: Average and standard deviation displacement values in the brain area with the corresponding inter-subject variability. Global statistics are extracted for the three components separately and for the magnitude of displacement.

Fig. 4.6 shows deformation within significant ROI. Values of azimuth angle (left of

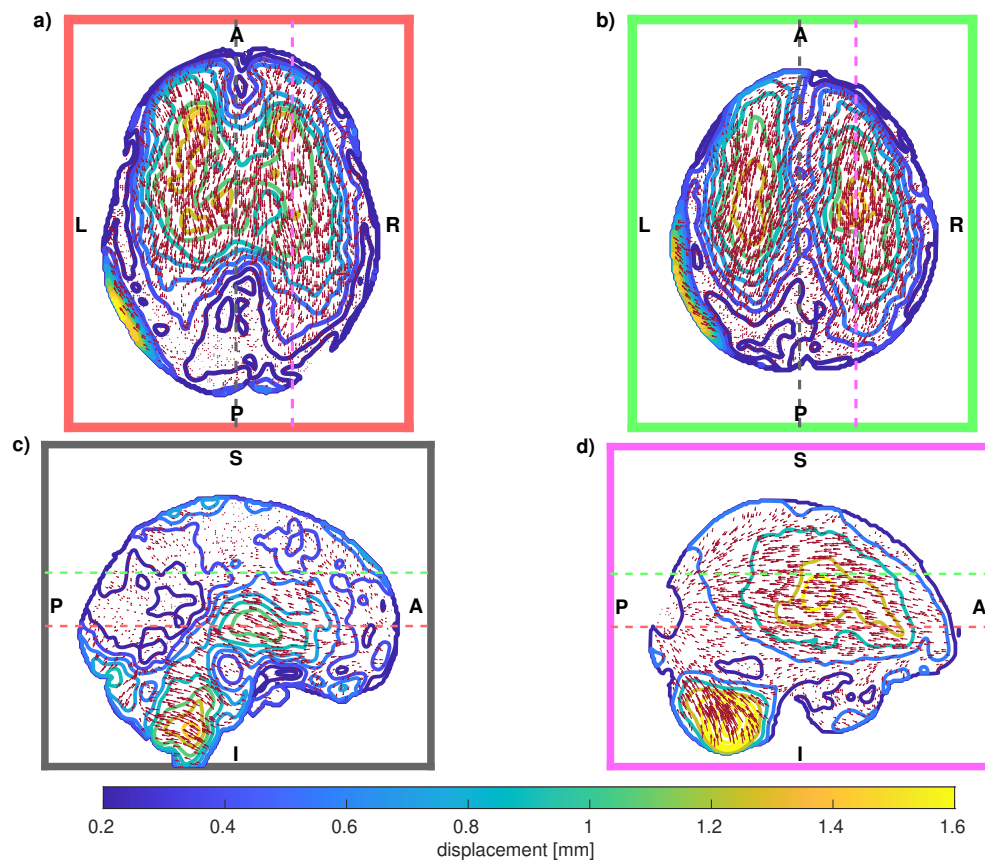


Figure 4.5: Vector plots of PBS for two axial (*a* and *b*) and two sagittal (*c* and *d*) slices. Length of vectors have been scaled for visualisation purposes: their magnitude is represented by the underlying contour plots. As reference, dashed coloured lines represent the position of the other slices. In particular, slice *a* was positioned at the level of the anterior and posterior horns of the lateral ventricles, whereas slice *c* was positioned at the level of the falx cerebri.

Fig. 4.6) indicate an overall displacement from anterior to posterior, as well as a predominant leftward component of deformation at peripheral (GM) and inferior (STN/RN/SN and BStem) regions. Elevation angle (centre of Fig. 4.6) shows an overall upward displacement which was bigger in the left than in the right hemisphere. Magnitude (right of Fig. 4.6) was greater in deep regions (e.g., basal ganglia) and lesser towards the skull and slightly bigger in the left than in the right hemisphere. Inter-subject variability between ROI showed slightly bigger values at deep structures than at the periphery, with an average of 0.15 mm at surgically relevant ROI.

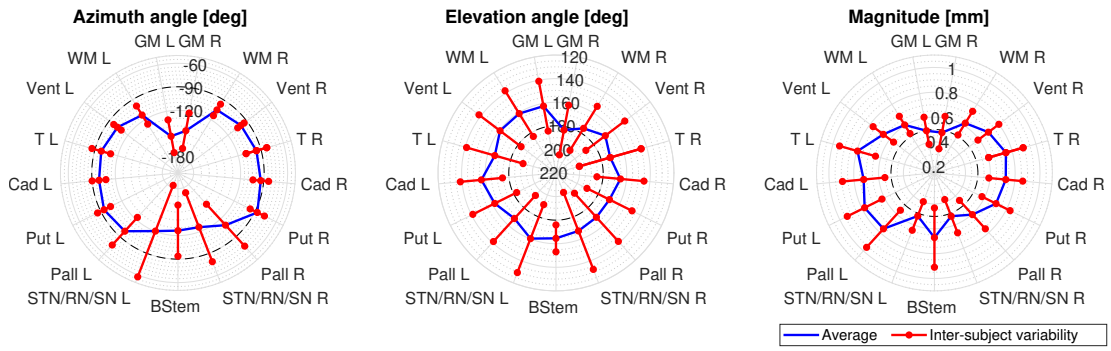


Figure 4.6: Polar diagrams showing azimuth (left) and elevation (centre) angles as well as magnitude (right) of PBS averaged over some ROI: left (L) and right (R) gray matter (GM), white matter (WM), ventricles (Vent), thalamus (T), caudate (Cad), putamen (Put), pallidus (Pall), subthalamic nucleus (STN), red nucleus (RN), substantia nigra (SN) and brain-stem (BStem). Whiskers represent inter-subject variability. Decreasing values of azimuth angle in the  $[-90, -180]^\circ$  range represent vectors progressively oriented towards left, whereas increasing values of elevation angle in the  $[90, 270]^\circ$  range represent vectors progressively oriented downwards. STN, RN and SN were combined together due to the small number of voxels represented by these structures.

Average and standard deviation values of strain are reported in Table 4.3, alongside the corresponding inter-subject variability. Figures 4.7 and 4.8 show the distribution of the hydrostatic and the deviatoric strains, respectively. Strain maps show elongation in frontal regions and confirm the negligible deformation in posterior regions as previously noticed. Local variability of deformation can be seen, as well as some structures (such as ventricles) and anatomical boundaries (such as the falx cerebri and the tentorium cerebelli). The polar plots in Fig. 4.9 show the diagonal components of the strain tensor for different lobes also decomposed in their hydrostatic and deviatoric components. Deformation along P-A direction occurred as both volume preserving ( $0.52 \pm 1.02 \%$ ) and volume change ( $0.44 \pm 0.64 \%$ ) expansion in the frontal lobe. However, deformation occurred predominantly as shape change in more posterior regions ( $-0.48 \pm 1.14 \%$ ), with a small volumetric compression ( $-0.25 \pm 0.76 \%$ ).

The APD did not reach statistical significance in the correlation with PBS. In supine positioning, however, MCB strongly correlated with azimuth ( $p=0.04$ ,  $r=-0.63$ , Fig. 4.10)

	Mean $\pm$ standard deviation	Inter-subject variability
<b>L-R</b>	0.18 $\pm$ 1.34 %	0.09 %
<b>P-A</b>	-0.04 $\pm$ 1.38 %	0.08 %
<b>I-S</b>	0.03 $\pm$ 1.32 %	0.09 %

Table 4.3: Average and standard deviation values of strain in the brain area with the corresponding inter-subject variability along the three main directions.

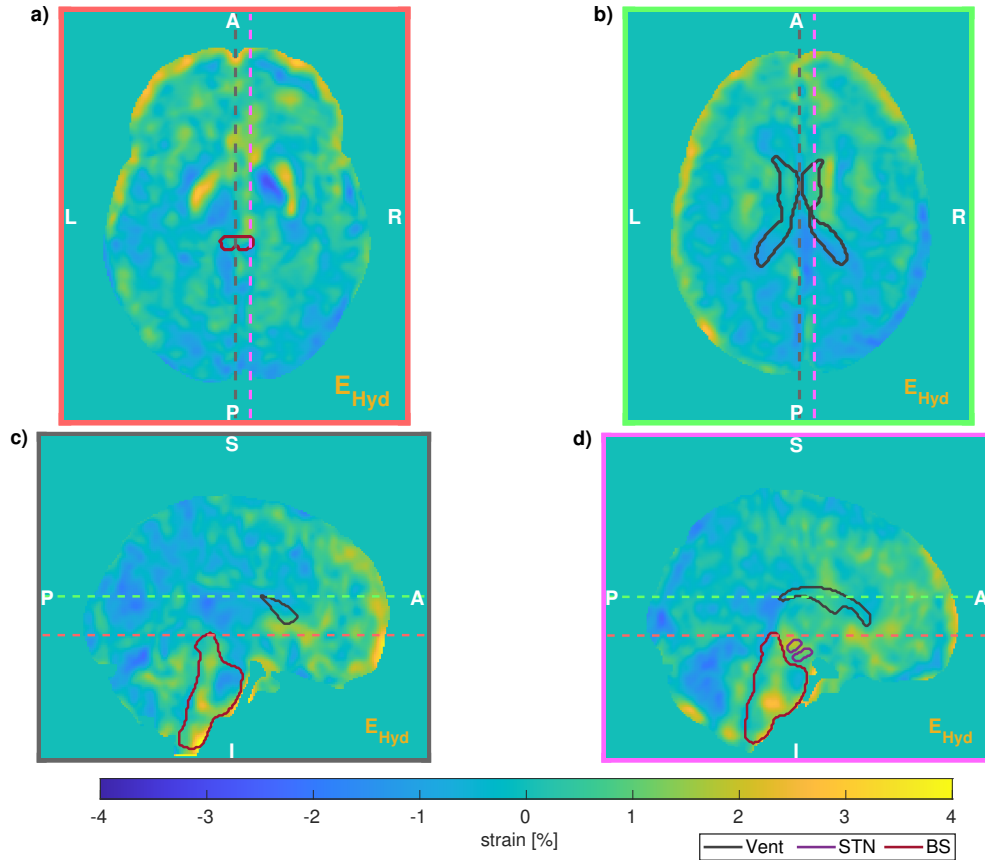


Figure 4.7: Distribution of the hydrostatic component at two axial (*a* and *b*) and two sagittal (*c* and *d*) slices. As reference, three ROI (Vent, STN, BStem) are delineated. Dashed coloured lines represent the position of the other slices. In particular, slice *a* was positioned at the level of the anterior and posterior horns of the lateral ventricles, whereas slice *c* was positioned at the level of the falx cerebri.

and elevation angles ( $p < 0.01$ ,  $r = -0.87$ , Fig. 4.10) of PBS, and weakly with magnitude ( $p = 0.08$ ,  $r = -0.55$ , Fig. 4.10). Linear fit showed that an increase of 10 mm of MCB led to a displacement  $20.66^\circ$  more to the left, a displacement  $29.17^\circ$  more downwards and finally a decrease of 0.12 mm in its magnitude.

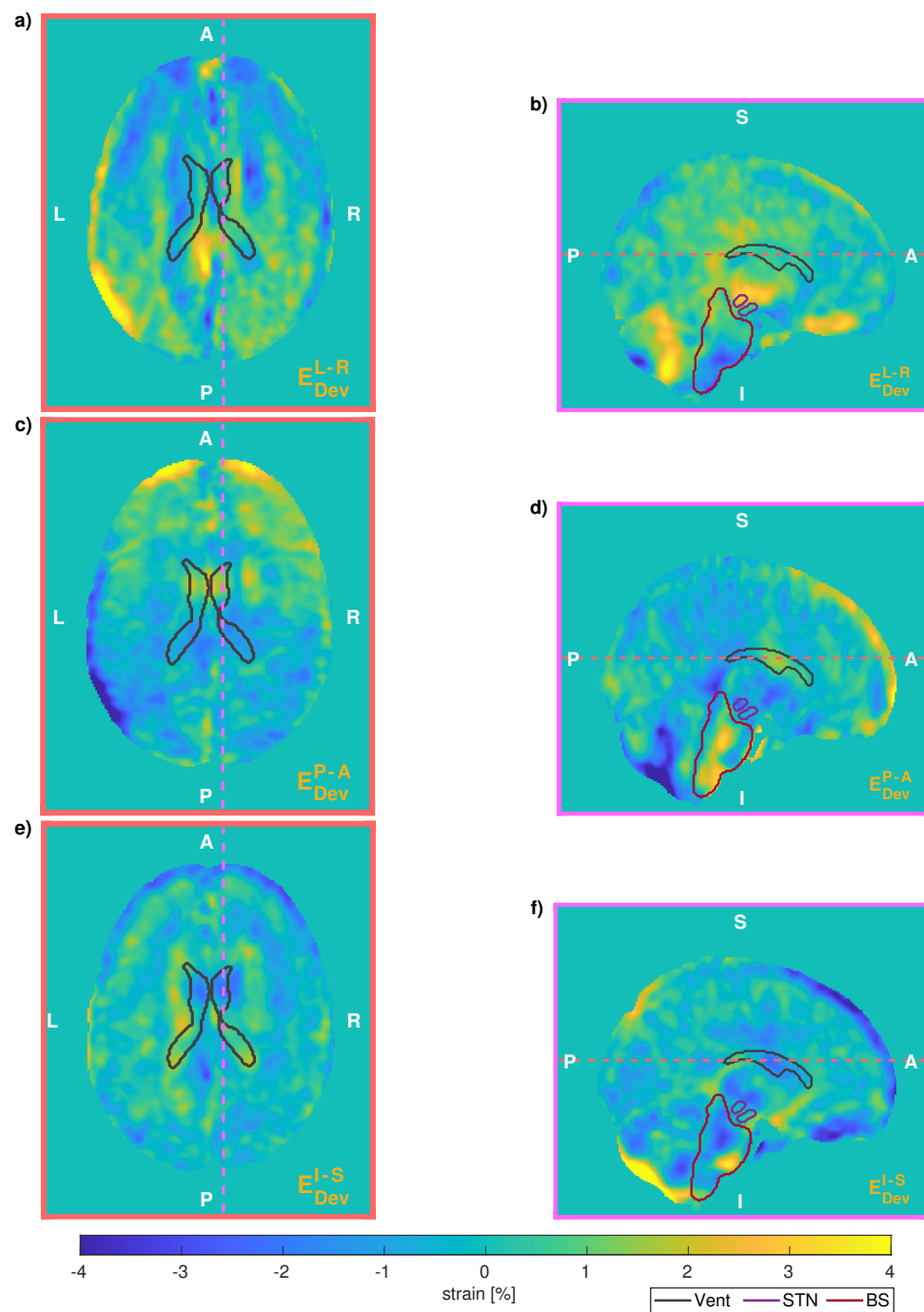


Figure 4.8: Distribution of the main deviatoric components of the Green-Lagrange strain. First row shows axial (*a*) and sagittal (*b*) slices of the L-R component; second row shows the P-A component (*c* and *d*); third the I-S component (*e* and *f*). As reference, three ROI (Vent, STN, BStem) are delineated. Dashed coloured lines represent the position of the other slices. Axial slices were positioned at the level of the anterior and posterior horns of the lateral ventricles, whereas sagittal slices were positioned 1 cm to the right of the falx cerebri.

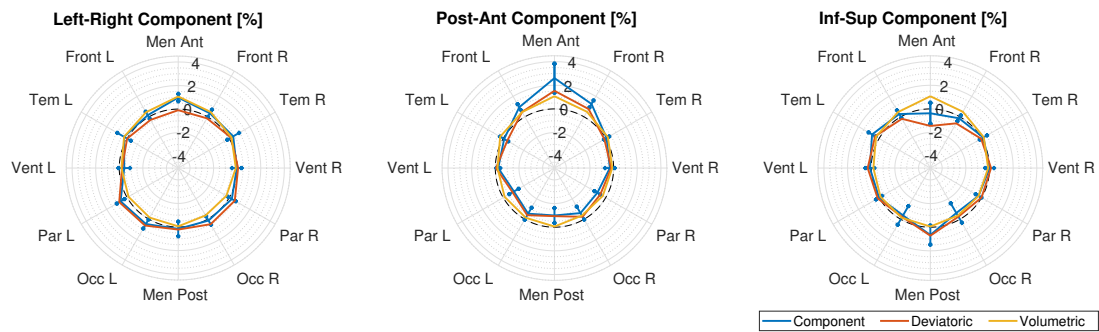


Figure 4.9: Diagonal components of strain averaged over some ROI: left (L) and right (R) anterior and posterior meninges (Men Ant, Men Post), frontal lobe (Front), temporal lobe (Temp), ventricles (Vent), parietal lobe (Par), occipital lobe (Occ). Blue lines represent the overall diagonal component (whiskers representing inter-subject variability), whereas the orange and yellow lines its deviatoric and volumetric components.

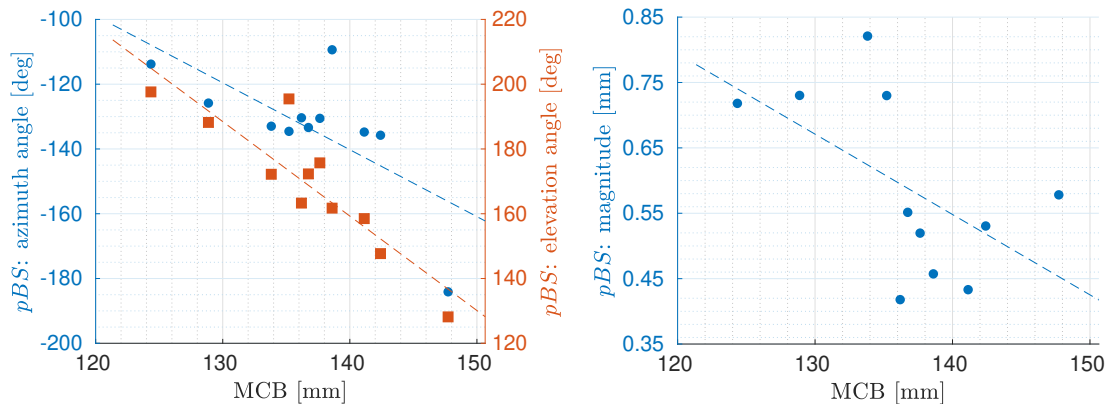


Figure 4.10: Scatter plots of the correlation between PBS and MCB. Azimuth (blue dots) and elevation (orange squares) angles are reported on the left against values of MCB, whereas against magnitude of PBS on the right. As reference, linear fit is superimposed to the data.

Head orientation in prone position did not reach statistical significance in the correlation with PBS. In supine positioning, however, a statistically significant correlation ( $p=0.01$ ,  $r=0.7364$ , Fig. 4.11) was found between elevation angle of gravity in supine and that of PBS: head tilt  $10^\circ$  more downwards in supine induced a shift  $10.86^\circ$  more downwards. Moreover, elevation angle of gravity strongly correlated with the magnitude of PBS ( $p<0.01$ ,  $r=0.80$ , Fig. 4.11): head tilt  $10^\circ$  more downwards induced a decrease in the shift by 0.18 mm.

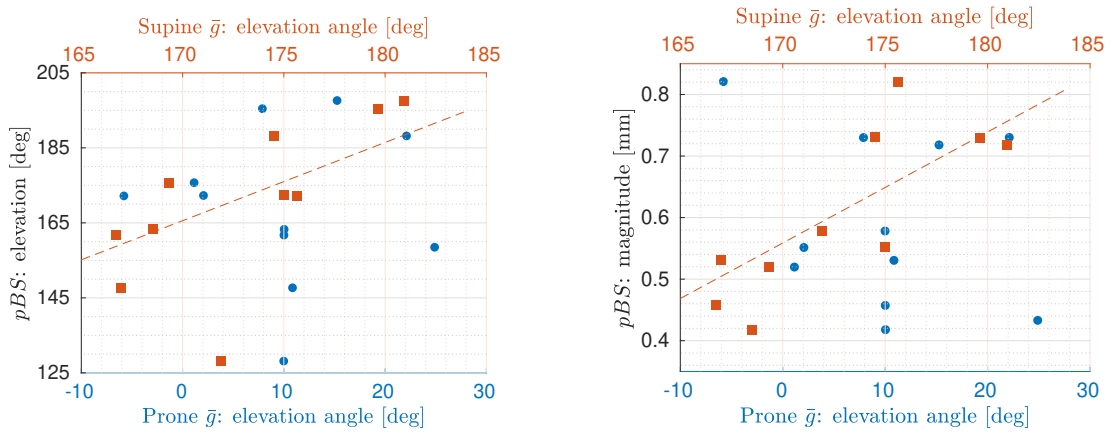


Figure 4.11: Scatter plots of the correlation between PBS and gravity ( $\bar{g}$ ). Elevation angle of gravity is here reported against elevation angle (left) and against magnitude of PBS (right) for both prone (blue dots) and supine (orange squares) positioning. As reference, linear fit is superimposed to the data in the case of the statistical correlation between elevation angle of  $\bar{g}$  in supine and both elevation angle (on the left) and magnitude (on the right) of PBS.

## 4.5 Discussion

This study successfully captured PBS as three-dimensional deformation over the entire brain volume, without limiting the analysis to any surface (such as the ventricular or the cortical surfaces [4, 5]). Differently from previous studies investigating the phenomenon in analogous conditions, accuracy of the measurements was evaluated, giving an error in following a biofidelic ground truth of  $0.0342 \pm 0.0229$  mm in the brain area. Analysis showed local variability in both displacement and compressibility of the tissue, demonstrating the complexity of PBS as interaction of gravity, anatomical boundaries and mechanical response of the tissue. Finally, the study revealed a strong correlation between the shift and both head orientation and the geometry of the intracranial cavity, giving a measure of their effect on PBS.

Values measured in the present study might be negligible relative to the typical shift seen during more invasive procedures such as craniotomy and tumour resection [94, 104, 154]. The obtained magnitude, however, was comparable to the error allowed for the correct targeting in IGNS-based interventions [3, 98, 101, 102]: deformation of some surgically

relevant structures ranged from 0.52 mm at the STN/RN/SN complex to 0.77 mm at the T. Values were in accordance with previous studies investigating the phenomenon in analogous conditions. Among these, Hill et al. [6] compared scans for two patients before surgery finding a deformation smaller than the resolution of their scans (1 mm). Schnaudigel et al. [5] reported brain deformation between 0.6 and 1.3 mm. Monea et al. [4] reported a 95% confidence interval of inwards shift between 1.08 and 0.47 mm at the brain surface and between 0.72 mm (inwards) to 0.83 mm (outwards) at the ventricular surface. Rice et al. [7] reported a value of PBS of 1 mm from measuring the change in thickness in occipital cerebro-spinal fluid. Recently, Yokoyama et al. [8] reported a downward and posterior displacement of the pituitary body of  $0.68 \pm 0.27$  mm and  $0.76 \pm 0.24$  mm, respectively, and a shortening of the pituitary gland by  $1.23 \pm 0.71$  mm from a sitting-to-supine change of positioning.

Deformation happened predominantly along the P-A axis following the direction of gravity, with a lateral component consistent among all subjects. Greater deformation could be seen further away from anatomical boundaries, and in particular in deeper structures, such as T, BG and BStem, confirming the influence of both gravity and anatomical constraints reported in the literature. The joint effect of the curved shape of the skull and the anchoring effect of the BStem most likely induced the anticlock-wise rotation around the L-R axis [4, 5, 155]; simultaneously, the tethering effect created by the meningeal and vascular elements might have contributed to the smaller deformation near these cortical areas [136, 137, 156]. The falx cerebri most likely limited any shift along its surface, inhibiting any deformation along the L-R direction (in particular at the level of the WM) [4, 5]; Finally, the tentorium cerebelli reduced the I-S deformation of the lowermost part of cerebrum. Results supported the pattern of deformation reported by Schnaudigel et al. [5]; but contrasted Monea et al. [4], who found a bigger shift of the cortex relative to the ventricles. The observed difference in elevation angle and magnitude of displacement between hemispheres can be related to the reported lateral asymmetry of the intra-cranial cavity [70, 157], as the head pan of subjects during scanning was consistent ( $89.91 \pm 2.99^\circ$ ) and did not show any statistical significance in



the correlation with PBS.

Strain analysis showed deformation as prevalent shape change rather than actual volumetric compression/extension. Frontal regions showed both stretch and expansion of tissue (consistent with the softer response in tension [158, 159]); on the other hand, posterior regions showed a prevalent deviatoric contraction along P-A (accommodated by an elongation along L-R and I-S directions) with a volumetric compression that was half the same component in frontal regions (consistent with the nearly incompressible nature of the brain tissue [160, 161]). The compression found in this study can be related to interstitial fluid redistribution and intracellular interactions as water escaping from *ex-vivo* specimens was reported during pre-conditioning before compressive testing [161]. Values were in accordance with the decrease in volume by  $5.07 \pm 3.24\%$  reported by Yokoyama et al. [8] at the lateral ventricles from a sitting-to-supine change of positioning. Whilst direct comparison is limited, Libertiaux et al. [162] reported a standard deviation of up to 5% in the volume ratio of *ex-vivo* specimens opposing to a natural compressive strain of up to 0.22 at rates between 1.2 mm/min and 120 mm/min; Franceschini et al. [163] showed small deformation of  $2.8 \pm 1.26\%$  of specimens under load of 3 and 6 N until displacement halted under physiological saline and free drainage. Conclusions on the mechanical response of the brain tissue are limited by the numerous factors influencing the full-field displacement measured in this study. However, brain tissue showed local variability in volumetric compression (up to 2%) in physiological conditions: these values help in assessing the degree of incompressibility [160, 162, 164] to assume when modelling the brain response in light of the accuracy required for the specific application.

The study reaffirmed the lateral component of deformation ( $-0.09 \pm 0.23$  mm) in prone-supine change of positioning as firstly reported by Schnaudigel et al. [5]. Despite being comparable to the margin of error of the measurements taken, this component was consistent in all subjects and stronger in deep and posterior regions (such as BG) [5]. As head orientation in an axial plane was neutral during scanning, gravity

alone could not be the only cause. First, MR distortions are reported to induce a spurious deformation along the L-R axis, which was measured on two phantoms giving absolute differences of  $0.4 \pm 0.2$  mm on 7T [89] and  $1.3 \pm 0.26$  mm on a 3T scanner [87] after correction. Second, asymmetry of the hemispheres is a well known characteristic of the human brain (Yakovlevian torque) which presents an anti-clockwise rotation around the P-A axis caused by a bigger right frontal and left occipital lobes relative to their contralateral [70, 165, 166]. Therefore, the leftward component of deformation seen in the present study could have been a joint effect of both residual distortion after correction and a clockwise deformation when moving to a supine position as a result of an even stronger twist effect when in prone positioning. Moreover, bigger brain volumes showed stronger leftwards deformation, the tissue being less constrained by anatomical boundaries. The results of the study further demonstrate the complexity of the phenomenon, as even an off-axis deformation can be critical to the overall accuracy of its prediction.

The inter-subject variability extracted in this study (average at surgically relevant ROI: 0.15 mm) represents the effect on PBS of further subject- and intervention-specific characteristics that needs to be addressed when modelling such phenomenon. Among these, intra-cranial geometry and head orientation revealed a strong correlation with PBS. Regarding the former, bigger cranial breadths diminished the constraining effect of anatomical boundaries on the brain tissue, giving bigger leftward and upward component of displacement. Monea et al. [4] also reported a statistically significant correlation of both MCB; however, statistical significance was reached only for lateral PBS and not for prone-to-supine change of positioning. Regarding head orientation, bigger shift was captured in neutral positions relative to more downwards tilted positions, as the curved shape of the skull might have limited the deformation of the brain tissue in more angled head orientations. No significant correlation was found for the head pan, due to the limited range of rotations acquired on an axial plane. In an experimental scenario, these factors need to be addressed in order to increase the accuracy of model-based predictions, conditional to the margin of error for the specific application. For the case

of IGNS, for instance, results of the study demonstrate the need for both subject- and intervention-specific correction of surgical trajectories as anatomical differences and slight changes in head tilt on a surgical table can affect the successful targeting of the correct structure.

A significant effort was made to understand and limit the potential inaccuracies related to the measurements, leading to the following main sources of error: residual MR distortions, improper initial skull alignment and inaccuracy of the deformable registration. Phantom and clinical studies on MR distortions report a spurious warp of around 1 mm [86–89] even after correction. This warp depends not only on the scanner (static magnetic field inhomogeneities) or the gradient coil (gradient nonlinearities, eddy currents), but also on the scanned object (chemical shift, susceptibility differences) [87–90]. Distribution of these properties over the brain is non-uniform, with larger distortions in inferior and frontal areas, close to air-filled cavities [89, 90, 92]. It is not stated whether distortions were accounted for in similar studies measuring PBS, as 1.5T [5] or 3T [4] scanners were used without any additional CT image. In the present study, *gradunwarp* showed better performance relative to the uncorrected scans and to the scanner-default distortion correction methods when comparing 7 T to 3 T images of two subjects (Section 3.2). Given the complexity of the phenomenon and the lack of a proper correction in the scanner [86], any further attempt to model distortions was considered out of scope and therefore a limitation of the study. Alongside distortions, any residual differences in the alignment of the skulls between the prone and supine scans of the same subject were captured by the deformable registration as an additional spurious component of deformation. Therefore, accuracy of this first step was evaluated on synthetic images (Section 3.3). Finally, with the aim of minimising the error when approximating the true deformation field, the transformation models of three best performing deformable registration methods were optimised against a biofidelic ground truth and their performance compared (Section 3.4).

Finally, the present study is limited by the small sample size, consisting solely of healthy

and young individuals. This choice was made for practical reasons, to make an initial evaluation and to limit the confounding effects of age [4]. As such, results presented here cannot be easily generalised to represent the average population of patients necessitating IGNS-based interventions. Widening the age range of the population sample or including patients in the analysis will be of more clinical interest and is going to be a future investigation.

## 4.6 Data Availability

The dataset generated during and/or analysed during the current study is available at the following OSF repository. OSF is a platform that allows researchers to collaborate, document, archive, share, and register research projects, materials, and data. Anonymised and face-stripped scans are available in the repository for other researchers to use, alongside the displacement and the strain maps extracted in the present work.

## Summary

Data acquisition of the physiological deformation of the brain tissue under the effect of gravity due to prone-to-supine change of positioning was discussed in the present chapter for a sample of 11 young adults. Differently from previous studies depicting the pattern of deformation of PBS, global and local three-dimensional measurements of deformation were captured over the whole brain area, both in a subject-specific and in an average spaces.

Even in the physiological conditions investigated in this study, magnitude of PBS resulted comparable to the 1 mm margin of error for the successful outcome of a IGNS-based intervention; displacement ranged from 0.52 mm to 0.77 mm at surgically relevant ROI.

Strain analysis confirmed the reported softer response of the brain tissue in tension ( $0.44 \pm 0.64$  % deviatoric strain and  $0.52 \pm 1.02$  % hydrostatic strain) and its nearly incompressibility ( $-0.48 \pm 1.14$  % deviatoric strain,  $-0.25 \pm 0.76$  % hydrostatic strain), with half the volume change in compression at posterior regions than the volume change in extension in frontal regions.

Cranial breath showed a strong correlation with PBS, showing a shift  $20.66^\circ$  more to the left and  $29.17^\circ$  more downwards, as well as a decrease in magnitude by 0.12 mm for a 10 mm increment in breadth. Head tilt, instead, induced a 0.18 mm smaller and  $20.86^\circ$  more downwards shift after a  $10^\circ$  downward tilt.

Results suggest the need for patient- and intervention-specific correction of surgical trajectories in order to improve the outcome of stereotactic procedures. Any improvement on IGNS does not rely on the amelioration of their hardware components, but on a suitable intra-operative update of the location of surgical targets. With this aim, the displacement field extracted in the study is of critical value for the initial validation of mathematical models aimed at compensating for PBS to integrate into IGNS, which is offered to download freely for interested researchers.

# Deep Tissue Injury: Parametric Identification and Error Analysis

## Overview

Similarly to Chapter 3, this chapter presents the efforts that were made to quantify the sources of error related to the DVC measurements of the large deformations of the human buttock from the *in-vivo* MR dataset [1] that will be investigated further in Chapter 6. As mentioned in Chapter 1, the approximations and the assumptions on both the calculations of the similarity measure and the flexibility of the transformation model introduce inaccuracies in the displacement measurements of large deformations. Quantifying the error associated to these estimations is therefore paramount to gauge the confidence in the DVC calculations of large deformations. Considerable effort was made to optimise three deformable registration methods, alongside assessing the corresponding accuracy against two biomechanically plausible ground truths replicating the phenomenon.

The work presented in this chapter will be part of the supplementary materials to the following draft to be submitted soon to the Journal of Biomechanics:

Zappalà, S., Bethany E. K., Marshall, D., Wu J., Evans S. L. & Al-Dirini M. A. R.. Volumetric redistribution of the soft tissues in the human buttock captured from MR *in-vivo* scans: accuracy of measurements and analysis of deformation.

First of all, Section 5.1 introduces to the problem of deep tissue injury, its clinical relevance and the importance of DVC measurements in the advancements of strategies and systems for the prevention and control of pressure ulcers.

Section 5.2, then, presents the optimisation of the affine registration methods that were used to set the initial conditions of deformation, that is, the alignment of pelvic elements, and the corresponding error.

Finally, Section 5.3 introduces first the biomechanical computational model that was designed to generate two physically plausible synthetic deformation fields representing the deformation of the human buttock under sitting loads. Then, three deformable registration methods were optimised against the latter ground truths and the corresponding error quantified.

## **5.1 Introduction to Deep Tissue Injury**

A pressure ulcer is localised damage to the skin and/or underlying tissue over bony prominences resulting from prolonged compression and shear strain induced by the interaction with supporting surfaces [13, 167–170]. Despite preventative measures being in place, pressure ulcers remain a burden on healthcare systems. In the UK, up to 202,000 people developed a new pressure ulcer annually in the period 2017/18, leading to an average annual cost of £748 for healed and £5972 for unhealed wounds per patient [9]. The highest incidence of pressure ulcers was observed in the sacrum and buttocks across six hospitals in the UK [171].

Deep tissue injury (DTI) is a pressure ulcer that originates at internal tissues surrounding bony prominences such as the ischial tuberosity (IT), greater trochanter (GT) and the sacrum [168, 172]. DTIs can, sometimes, be diagnosed even 24–72 hours after the initial onset [173] or can be initially miscategorised, as the damage is not always associated with broken skin or an open wound [174]. Age, impaired mobility, continence, temperature and nutrition have been found to be related to the onset of the damage,

making the efficacy of preventive measures adopted in clinical practice somewhat limited [10, 175, 176]. Among these, re-positioning, skin examination, wound dressing, nutritional assessment and pressure measurements at the skin-seat interface are common practice in the control and prevention of DTIs [172, 174, 175, 177]. Any advancements in the design of these measures rely on a better understanding of the aetiology of DTI, alongside a more reliable way to reproduce conditions associated with the onset of tissue damage [10, 10, 178, 179].

In order to achieve this, finite element (FE) models of sitting biomechanics allow the calculation of the internal deformation field of tissues in response to a load at the seating interface, replicating and ultimately predicting the conditions leading to tissue damage [10, 180, 181]. The reliability of FE models depends on the availability of accurate measurements that can fully represent the complexity of the phenomenon to be modelled. This is crucial for the appropriate design, exhaustive optimisation and thorough validation of such models [181–183]. To the best of the authors' knowledge, previous measurements failed to represent fully the three-dimensional complexity of the deformation of the human buttock *in-vivo* both at superficial and internal tissues [1, 184–187]. These include direct measurements from MR scans [1, 10, 11, 184], motion capture data [188] and digital image correlation on ultrasound images [189]. Rich volumetric measurements of such deformation would benefit the understanding of the phenomenon. Accuracy is therefore essential to gauge the margin of error associated with the DVC calculations and hence the value of these measurements.

## 5.2 Pelvis Alignment: Optimisation

As previously introduced in Section 3.3, for the output warp field of the elastic registration to depict the displacement field under investigation, every differences between scans not caused by the solely deformation of the soft tissues should be minimised. An initial registration of the scans was therefore needed to bring images to the same coordinate



system, but more importantly, to align bony structure to use as rigid reference between deformed and undeformed conditions (that is, setting initial conditions of deformation). Similarly to Section 3.3, the following section shows the optimisation of the registration methods in the alignment of pelvic skeletal elements, followed by the comparison of their performance in setting the initial conditions of deformation.

**Methods** The same dataset by Al-Dirini et al. [1] as in Chapter 6 was used, where magnetic resonance (MR) scans of 10 healthy subjects (aged 19-39, body mass index (BMI) =  $28.02 \pm 4.71 \text{ kg/m}^2$ ) depict the quasi-static deformation of gluteal soft tissues from sitting in a semi-recumbent position. The progressive deformation was captured by removing two 10 mm inserts from the left buttock. Scans were proton density weighted spin echo (TR=4542 ms, TE=32.18 ms) and were acquired in a 1.5T scanner, with an anisotropic resolution of  $0.78 \times 0.78 \times 10 \text{ mm}^3$ . Image deconvolution via software NiftyMIC [190] was used to decrease the voxel spacing along the same direction. The sagittal scans available in the dataset [1] (resolution  $10 \times 0.78 \times 0.78 \text{ mm}^3$ ) could not be used in the deconvolution call, due to them being affected by strong MR distortions. A single observer manually segmented the following skeletal structures from both the full-weight bearing (full-WB) and non-WB scans: bilateral inferior pubic rami (to include the left IT) as well as the left femoral head (to include the left GT). Registration parameters were optimised on the scans of three participants to include the effect of inaccuracies in the segmentations: subjects were selected to represent the minimum (subject 10), average (subject 2) and maximum (subject 8) BMIs in the population sample. Further details on the database used are in Section 6.2.1

The following best performing affine registration methods were compared: FLIRT (from the FSL suite) [78], ANTs [79] and *elastix* [44]. The segmented masks were used to restrict the intensity-based registration of the full-WB to the non-WB scans. Quality of the alignment was quantified with two error metrics. First, the Dice coefficient DC was

calculated on the whole masks to give a measure of the global correspondence:

$$DC = \frac{\#(\hat{A} \cap B)}{\#(\hat{A}) + \#(B)}, \quad (5.1)$$

where  $\hat{A}$  is the registered moving mask and  $B$  the fixed one. Moreover, the Hausdorff distance HD [124] was extracted to gauge the specific alignment of the masks representing the IT and GT only (regions of interest):

$$HD = \max \left( \overrightarrow{HD}(\hat{P}, Q), \overrightarrow{HD}(Q, \hat{P}) \right), \quad (5.2)$$

$$\overrightarrow{HD}(\hat{P}, Q) = \max_{\forall p \in \hat{P}} \left( \min_{\forall q \in Q} \|p - q\| \right), \quad (5.3)$$

where  $\hat{P}$  is the registered moving masks,  $Q$  the fixed one and  $\overrightarrow{HD}(\hat{P}, Q)$  the directional  $HD$ .

Search grids were generated using the Simulink Design Optimization package in MATLAB: 300 points were selected for each method via the Sobol quasi-random sampling, giving a total of 2700 runs. Computations were run on a cluster at the Cardiff University Brain Research Imaging Centre (CUBRIC). Sensitivity analysis via Gaussian emulation [85] (GEM-SA software [132]) was used to infer the main effect, as well as the pairwise interactions of parameters with the error metrics: these were given as percentages of the total variance on the metrics.

Chosen ranges of parameters are reported in Table 5.1. For all methods, three similarity measures were tested, that is, variations of sum of squared differences, mutual information and correlation coefficient. Transformation models with 6 (rigid), 9 (similarity) and 12 (affine) degrees of freedom (DoF) were selected.

Specifically for FLIRT, rotation angles were perturbed during optimisation in a range of angles between  $20^\circ$  (i.e.,  $-10^\circ - 10^\circ$ ) and  $180^\circ$  (i.e.,  $-90^\circ - 90^\circ$ ): the wider the range, the further the convergence is perturbed away from any sub-optimal local minima. A

minimum of 24 and a maximum of 512 histogram bins were selected for similarity measures based on intensity binning: their number determines the accuracy of the statistics of the intensity distribution [77].

Regarding ANTs, gradient step was varied between 0.05 and 0.3: the parameter limits the extent of movement of control points after each iteration, where small values represent small advancements and vice-versa. The radius of the similarity window was varied between 2 and 6 voxels, representing areas made of 124 and 2196 voxels, respectively.

Finally, for *elastix*, similarity measure was based on drawing between 1000 and 4000 random samples on a cubic region with side length ranging from 40 mm to 70 mm, giving regions made of 10519 and 56377 voxels.

Method	Parameter	Values
All	similarity measure degrees of freedom <i>z</i> -resolution [mm]	SSD, MI, CC 6, 9, 12 2 - 10
FLIRT	number of bins search angles [°]	24 - 512 10 - 90
ANTs	neighbourhood radius step update	2 - 6 0.05 - 0.3
<i>elastix</i>	spatial samples region size [mm]	1e3 - 4e3 40 - 90

Table 5.1: Optimisation of the initial registration: ranges of parameters tested. Similarity measures tested include sum of squared differences (SSD), mutual information (MI) and correlation coefficient (CC)

**Results** Figure 5.1 shows comparable intra-subject performance between methods (that is, within the same subject). Evident were instead the inter-subject differences in values (i.e., between subjects). *elastix* was the most robust method and was therefore used for the measurements of Chapter 6, with 405 calls reaching an acceptable DC

value of at least 0.80 [79]; FLIRT and ANTs, instead, showed only 342 and 361 runs with DC over 0.8, respectively.

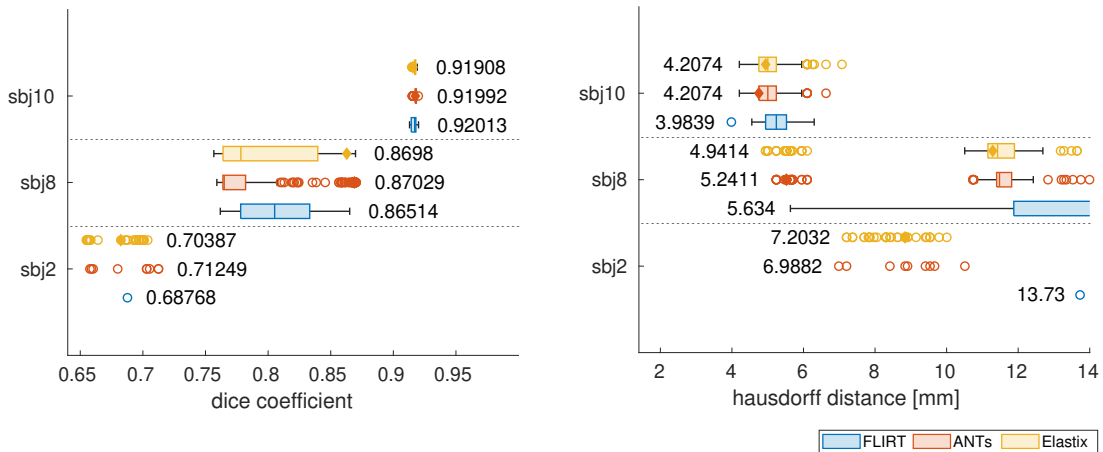


Figure 5.1: Boxplots showing the extracted values of the DC (right) and the HD (left) for each method. Values of DC are evaluated over the whole pelvic area segmented; HD values, instead, are evaluated only at the IT and GT. Annotated values display the best performance for each method, that is, maximum DC and minimum HD values. Top, centre and bottom rows show results for the 3 subjects (sbj) analysed. As reference, diamond markers show the performance of each model with default parameters (if successful).

Sensitivity analysis on *elastix* (Figure 5.2) showed that variability in DC given by uncertainty in inputs was 8% of its average, whereas the same fraction for the HD was 40%: the latter was therefore more sensitive to changes in parameters' values.  $Z$ -resolution, similarity measure and number of samples were the most influencing parameters:  $z$ -resolution explained the majority of the variance in DC values (72%), whereas 9% of the total variance in HD values; similarity measure led to the majority of the variability of HD (28%), whereas  $z$ -resolution and spatial sample together explained 4% of the total variance in HD.

Figure 5.3 shows the surface plots of the pairwise comparison between the previously identified three most influencing parameters. The optimal set was therefore chosen as: advanced mattes mutual information as similarity measure; affine transformation; 10 mm  $z$ -resolution; 1937 samples drawn from a cubic region with 49 mm side length.

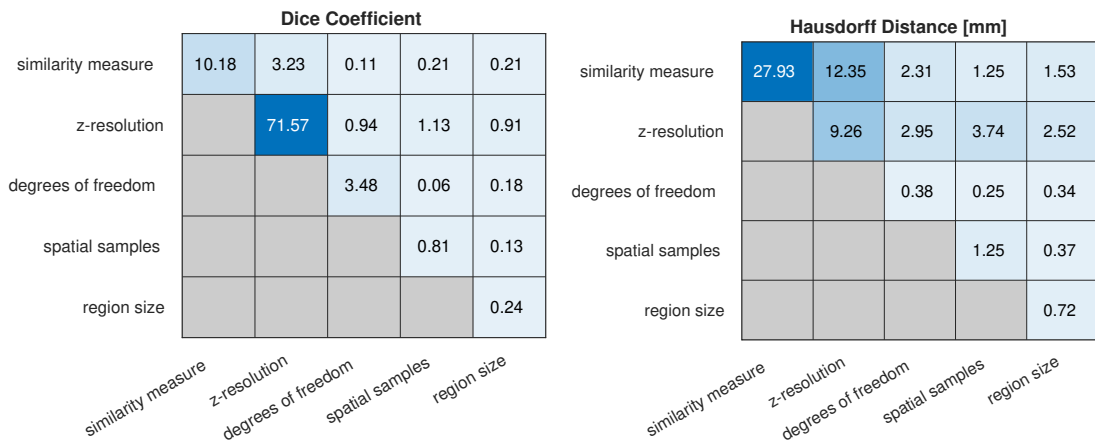


Figure 5.2: Sensitivity analysis on the initial registration: heatmap of the individual and joint sensitivity of the error metrics on the parameters trialled for *elastix*. On the left, percentages relative to the mean total variance of the DC (that is, 0.00271051), whereas on the right of the HD (that is, 13.7047 mm<sup>2</sup>).

**Discussion** Registration calls were satisfactory as the majority of DC values were close to 0.85 with few above it. Xu et al. [72] recommended values above 80% for satisfactory alignment of medium organs. Methods showed similar optimal intra-subject performance. This was expected given the simple registration problem, that is, intra-subject and monomodal registrations. Performance was mostly affected by differences in either the quality of the segmentations or in the initial alignment of the scans. On one hand, scans of subject 10 were well aligned prior to registration and were clear enough for straightforward segmentations: this led to most of the calls been successful for all methods. Parameters' optimisation for this subject had very little effect. On the other hand, scans of subject 2 were misaligned and segmentations proved to be challenging due to the small number of slices capturing the pelvic area. Most of the registration calls were unsuccessful and the few successful were outliers<sup>1</sup>. In this case, optimisation made the difference between an acceptable and a catastrophic registration call.

*elastix* was the most robust method in terms of number of successful alignments over the registration runs. This might have been related to the random sampling: bigger regions could be compared between images, and it was shown to be stronger to noise [44].

<sup>1</sup>Outliers are calculated as values that are one and a half times the inter-quartile range away from either the 25<sup>th</sup> or the 75<sup>th</sup> percentiles.

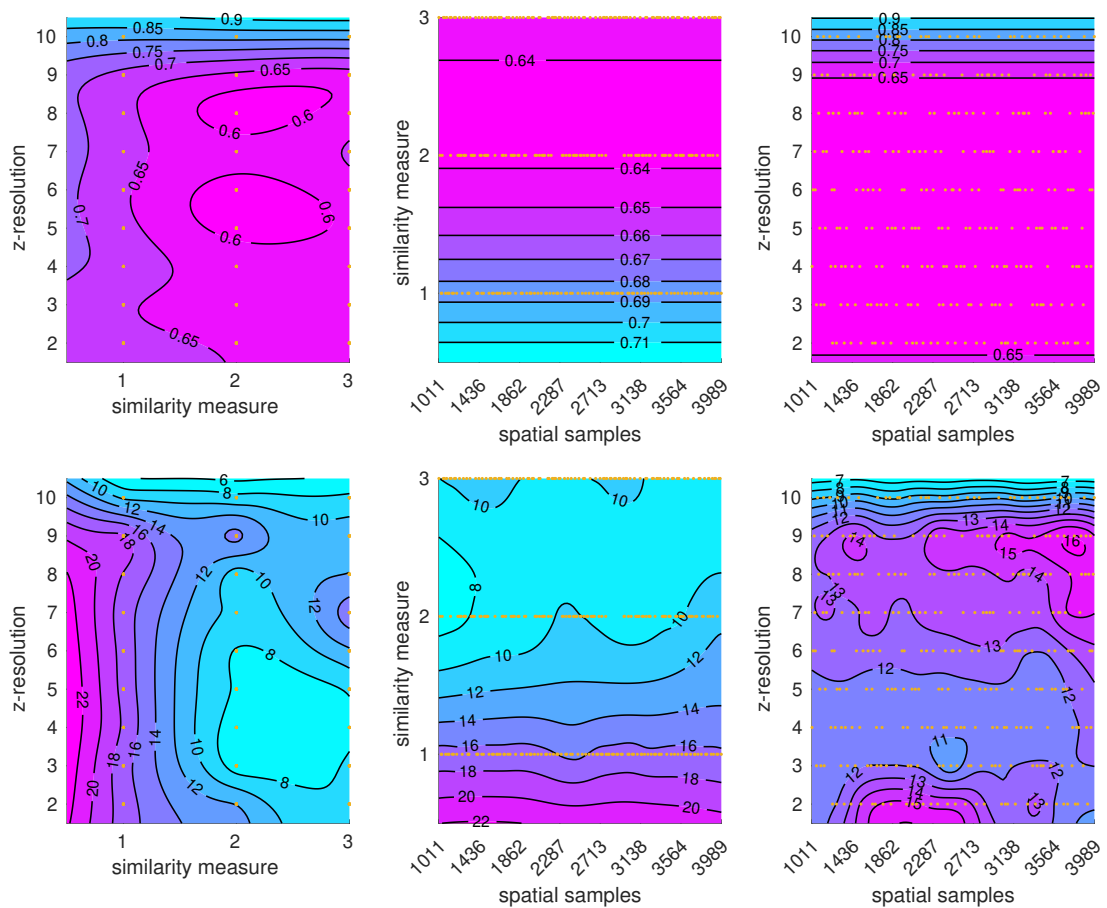


Figure 5.3: Optimisation of the initial registration: surface plots of the DC (top row) and HD (bottom row, in [mm]) for the three most influencing parameters of the *elastix* method. Yellow dots represent the query points. Best performance is represented with lighter colours, that is, higher values of DC and lower values of HD. Similarity measures tested were SSD (number 1 in the plot), MI (number 2 in the plot) and CC (number 3 in the plot).

Affine over similarity and rigid transformations was the best scoring transformation, probably due to the higher DoF and the beneficial effect on compensating for residual distortions between scans [90, 92]. The optimal resolution along the  $z$ -direction was the original one, as deconvolution with no orthogonal scans is known to introduce intensity averaging and partial-volume errors [131].

A limitation of the study was the absence of the evaluation of the inter- or intra-rater variability in the segmentations. This made it impossible to distinguish between error due to improper manual segmentation (proved to be difficult by the coarse  $z$ -resolution)

and the one caused by inaccuracy in the registration [76]. Any further attempt to improve the quality of the segmentations was considered out of scope: ultimately, registration calls were based on intensity values and the ROI only used to restrict the registration area.

### 5.3 Deformable Registration: Optimisation

As previously introduced in Section 3.4, once the initial conditions of deformation are carefully set, the warp field as output of the deformable registration should depict the desired displacement field. The sections aims to quantify the accuracy in capturing the large deformation of the buttock due to sitting, which are affected by approximations in the calculations leading to inaccuracies in the estimated warp field [24].

**Methods** The same three best performing elastic registration methods as in Section 3.4 were optimised and compared. These were identified in Section 2.4 as DRAMMS [35], SyN [69] and *elastix* [191].

Optimisation was carried out against two biomechanically plausible displacement fields generated via a simplified FE model of the buttock (detailed below). The fields were extracted to represent the deformation captured in the dataset used in Chapter 6. The first simulated field depicted the transition from non-WB condition to partial-WB, which was replicated during acquisition by removing one of three 10 mm thick wooden boards that were placed under the left buttock. The second field, instead, represented the transition from non-WB to full-WB conditions, where all three boards were removed (further details in Section 6.2.1). These ground truths were then applied to the non-WB scan of one subject and the resulting images registered back to the original.

Minimising discrepancies between the estimated displacement field  $\mathbf{T}_e$  and the ground truth  $\mathbf{T}_{gt}$  gave the best performing method alongside its optimal parameter set. The

error metric used was the mean norm of the error vector (MNE) [120, 131]:

$$MNE = E_{\mathbf{x}} [\| \mathbf{T}_{gt}(\mathbf{x}) - \mathbf{T}_e(\mathbf{x}) \|], \quad (5.4)$$

where  $\mathbf{x}$  is the original position of voxels in a region of interest and  $E_{\mathbf{x}}[\cdot]$  the expected value over the voxels.

A linear tetrahedral mesh was extracted from the segmentations of the fat and muscle areas of the subject showing average BMI [1] via *Simpleware ScanIP* (Figure 5.4). A Neo-Hookean constitutive model was used for both the fat and muscle layers, with a Poisson's ratio of 0.49 and equivalent Young moduli of 30 kPa and 100 kPa, respectively [192]. A tied/non-slip contact was assigned to the fat–muscle interface. Two loading conditions of 10 mm (simulating non-WB to partial-WB) and 30 mm (simulating non-WB to full-WB) were imposed as fixed displacements on the nodes at the buttock-seat interface. Only in-plane displacement was allowed at the lateral surfaces, with a zero-displacement condition at the internal (muscle-pelvis interface) surface. Simulations were run with the FEBio suite (Version 2.0), obtaining the vector fields in Figure 5.5. Linear interpolation onto the voxel grid of nodal displacements was carried out.

The focus of the optimisation was on parameters controlling for the transformation model and the similarity measure. Range of parameters tested are reported in Table 5.2. For all methods, cross-correlation was chosen as a similarity measure, given the simple monomodal and intra-subject nature of the registration task. Three interpolation methods (linear, sinc and B-spline) were applied to the warped scans to gauge the influence of intensity interpolation after initial registration of the skeletal elements. Given the coarse resolution of the images along the  $z$ -direction ( $0.78 \times 0.78 \times 10 \text{ mm}^3$ ), image deconvolution via software NiftyMIC [190] was used to decrease the voxel spacing along the same direction. The sagittal scans available in the dataset [1] (resolution  $10 \times 0.78 \times 0.78 \text{ mm}^3$ ) could not be used in the deconvolution call, due to them being affected by strong MR distortions. Resolution along  $z$  after deconvolution was varied



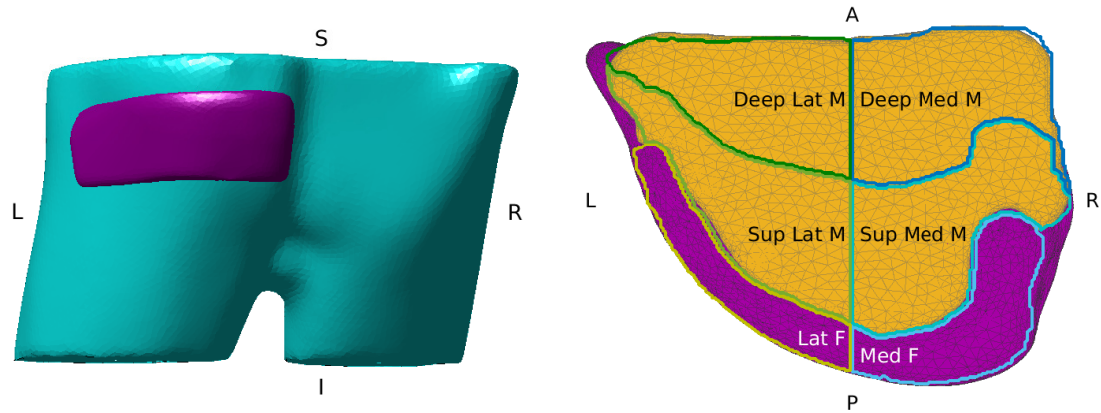


Figure 5.4: Simplified FE model of the buttock. On the left, the position of the segmented area is reported over the acquired field of vision. On the right, axial view of the generated mesh. Fat tissue is here depicted in orange, whereas muscle in yellow. For reference, nomenclature for anatomical locations used in the present study is reported on the mesh: Deep Medial Muscle, Deep Lateral Muscle, Superficial Lateral Muscle, Superficial Medial Muscle, Lateral Fat, Medial Fat

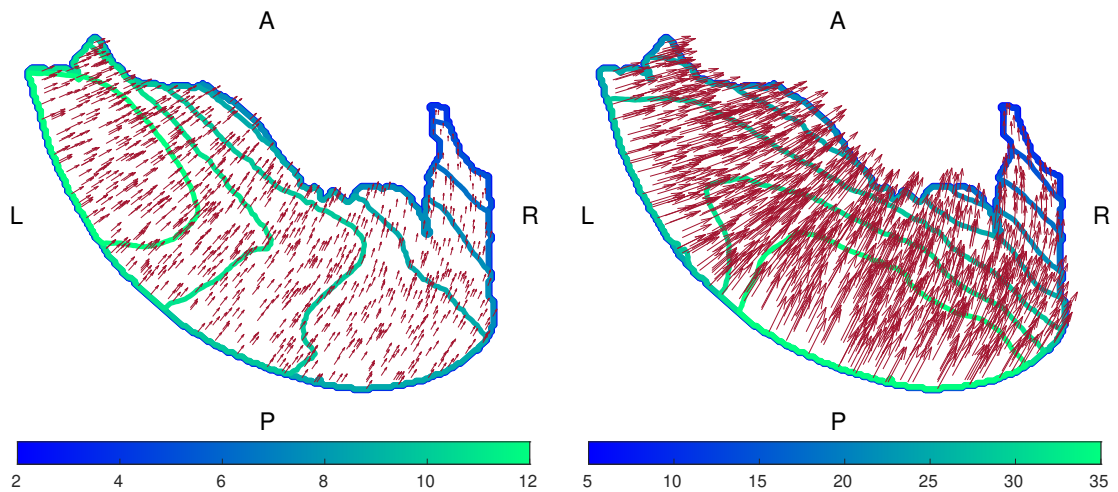


Figure 5.5: Axial views of the generated ground truths: on the left, vector field given by a fixed displacement of 10 mm (azimuth angle of  $43.25 \pm 21.77^\circ$ , elevation angle of  $-0.77 \pm 1.53^\circ$  and magnitude of  $7.30 \pm 3.15$  mm), whereas given by a fixed displacement of 30 mm on the right (azimuth angle of  $45.07 \pm 25.44^\circ$ , elevation angle of  $0.26 \pm 1.02^\circ$  and magnitude of  $19.37 \pm 9.58$  mm). Lengths of vectors have been scaled for visualisation purposes: their magnitude is represented by the underlying contour plots.

between half the resolution on the  $xy$ -plane and the original resolution.

Specific to the call to DRAMMS, regularisation weights were varied between 0.1 (aggressive fitting) and 0.25 (smoother deformations). Knot spacing for the free form

deformation model [49] was varied between 3 and 33 voxels on the X-Y plane (i.e., between 2.34 mm and 33.78 mm) and between 1 and 30 along the Z direction (with spacing depending on the  $z$ -resolution after deconvolution). Trilinear and B-spline models were tested for the interpolation of the displacement field from the control points to the voxel grid. Between 3 and 7 samples were drawn in the optimisation process, where larger values are associated with higher accuracy at a higher computational cost. These samples are selected along each direction and their diagonal, giving a total of 55 and 127 samples (in a neighbour that depends on the selected Gabor scales), respectively.

Regarding the call to SyN, knot spacing of the B-spline transformation model [80] at the top of the four multiresolution levels was varied between 16 and 33 mm on the  $xy$ -plane (final knot spacing between 2 mm and 4.125 mm at original resolution), whereas between 16 and 33 mm along the  $z$  direction (final knot spacing between 2 mm and 4.125 mm); first, second and third orders of the spline model were tested. Similarly to the call for ANTs, gradient step controlling for the extent of movement of control points during optimisation was varied between 0.05 (small advancements) and 0.29 (large advancements). Cross-correlation was used as similarity measure, with a radius ranging from 1 to 6 voxels (that is, defining regions of 26 and 2196 voxels), respectively.

Finally, for *elastix* different final grid spacing were tried (2 - 30 mm on  $xy$ -plane and 2 - 30 mm along  $z$ -direction), with scaling factors of 8, 4, 2, 1 over the four resolution levels. First, second and third order B-spline models were tested. Advanced normalised correlation was used with between 1000 and 4000 random samples drawn from a region with side length between 30 mm and 70 mm, with a third of the samples along the  $z$ -direction.

Grid points for the optimisation were generated with the Sobol quasi-random sequence with the Simulink Design Optimization package in MATLAB, giving a total of 2400 runs per method. Sensitivity analysis via Gaussian emulation [85] (GEM-SA software [132]) was performed to evaluate the main influence of parameters on the error metric, as well

as the pairwise interactions. Surfaces of the pairwise interaction of parameters on the MNE were generated by fitting a Gaussian process regression model to the MNE values given the input parameters via MATLAB, where best values of hyperparameters were automatically optimised during the call for optimal fit.

Method	Parameter	Values
All	$z$ -resolution [mm] interpolation	0.4, 0.78, 2 - 10 linear, sinc, BSpline
DRAMMS	final knot $xy$ -spacing [vxls] final knot $z$ -spacing [vxls] interpolation to voxel grid samples in optimisation regularisation weight	3 - 33 1 - 30 1 - 3 3 - 10 0 - 1
SyN	base knot $xy$ -spacing [mm] base knot $z$ -spacing [mm] spline order neighbourhood radius [vxls] step update	3 - 33 16 - 33 1 - 3 1 - 6 0.05 - 0.29
<i>elastix</i>	final grid $xy$ -spacing [mm] final grid $z$ -spacing [mm] spline order spatial samples region size [mm]	2 - 30 2 - 30 1 - 3 $1e3 - 4e3$ 40 - 90

Table 5.2: Ranges of parameters tested for the three deformable registration methods tested.

**Results** Similar optimal performance was shown by the methods in following the 10 mm ground truth, whereas diverse were the optimal values for the 30 mm simulation (Figure 5.6). In the 10 mm simulation, 5<sup>th</sup> percentiles of errors were 0.792 mm, 1.036 mm and 0.849 mm for DRAMMS, SyN and *elastix*, respectively. For the 30 mm, the same values were 2.905 mm, 6.563 mm and 1.398 mm, respectively.

Figures are grouped by registration methods, showing first heatmaps of the sensitivity analyses (Fig. 5.7, 5.10, and 5.13). These allowed the identification of the three most influencing parameters, whose pair-wise interaction on the error metric are shown in the

surface plots of Fig. 5.8, 5.11 and 5.14. Each group of plots ends with the histogram of the frequency of parameters' values in optimal registration calls, that is, calls leading to MNE below its 5<sup>th</sup>-percentile (Fig. 5.9, 5.12 and 5.15). Choice of optimal parameter set was based on both the individual frequency of parameters in the optimal calls as well as their pairwise interactions from surface plots of the average MNE.

Optimisation was fundamental for all methods, even for SyN which showed the smallest difference between unsuccessful and successful calls. In the 10 mm simulation, inter-quartile ranges of MNE values were 1.815 mm for DRAMMS (25% of the average simulated displacement), 1.271 mm for SyN (17%) and 1.549 mm for *elastix* (21%); whereas 6.549 mm (34% of the average simulated displacement), 2.443 mm (13%) and 3.830 mm (20%) in the 30 mm one, respectively.

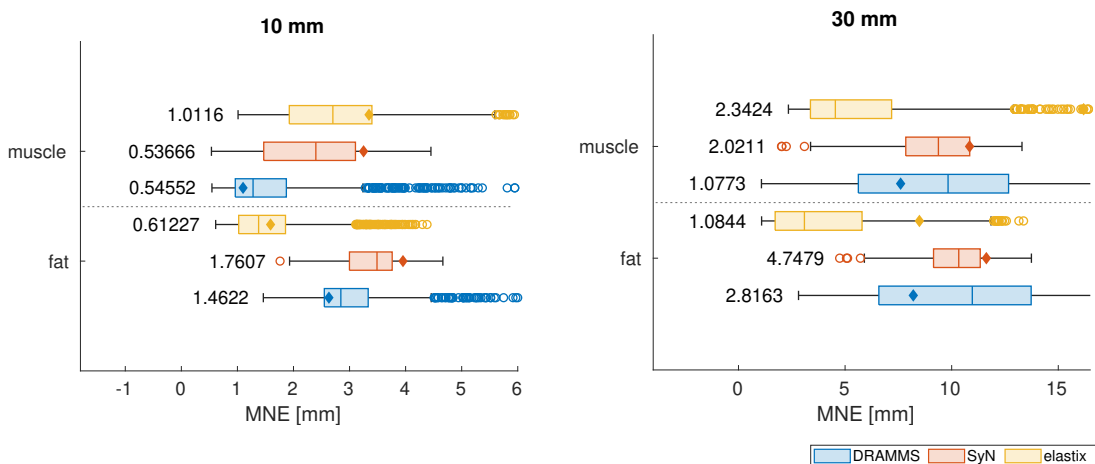


Figure 5.6: Boxplots showing the distribution of MNE values on the left for the 10 mm results, on the right for the 30 mm results. Boxplots are reported for each method: that is, DRAMMS, SyN and *elastix*. Annotated values display the best performance, that is, the minimum MNE value. Top row show results in the muscle area, whereas for the muscle areas at the bottom. For reference, diamonds indicate the performance of the methods with their specific default parameters.

*elastix* showed a more desirable distribution of the MNE in both simulations and was therefore chosen for the DVC measurements in Chapter 6. Although surfaces do not show a global minimum, a plateau of comparable values of MNE can be noticed: the optimal set was therefore chosen as the one that was associated with lower degrees of

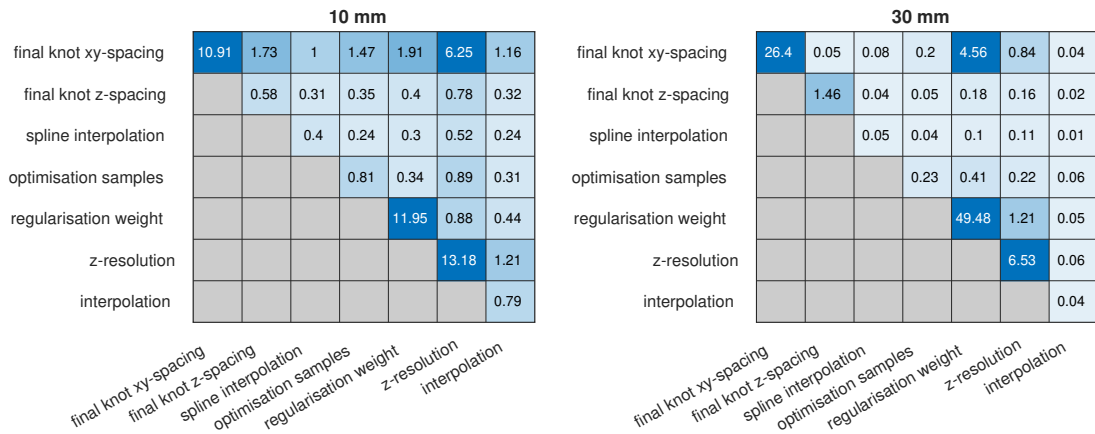


Figure 5.7: DRAMMS: heatmap of the individual and joint sensitivity on the error metric (MNE). On the left, percentages relative to the total variance in the 10 mm simulation, whereas on the right for the 30 mm simulation (0.992304 mm<sup>2</sup> for the 10 mm simulation, and 15.5281 mm<sup>2</sup> for the 30 mm one).

freedom [17] or that was closer to the recommended parameters. Final parameter sets are reported in Table 5.3, with the corresponding values of MNE in Table 5.4

To gauge the effect of the coarser resolution along  $z$  and the consequent reconstruction on the accuracy of the measurements, elevation angles of the vector errors were extracted. Larger values of the elevation angle represent an overall larger deviation along the  $z$ -direction than the deviation on the  $xy$ -plane. For the 10 mm simulation, values for DRAMMS, SyN and *elastix* were, respectively  $59 \pm 22^\circ$ ,  $52 \pm 24^\circ$  and  $44 \pm 24^\circ$ . For the 30 mm simulation, instead, values were  $59 \pm 25^\circ$ ,  $35 \pm 30^\circ$  and  $48 \pm 25^\circ$ . Values were overall above  $45^\circ$ , which can be considered the threshold above which the error along the  $z$ -direction is larger than the projection of the error onto the  $xy$ -plane. This shows that accuracy was on average affected by the uncertainty in the reconstruction of the displacement along the coarser  $z$ -direction.

**Discussion** *elastix* showed a preferable performance in following the ground truth representing the large deformations of the buttock due to sitting. The optimal parameter set in Table 5.3 was used for the DVC measurements in Chapter 6, which lead to an error of 0.989 mm in following the 10 mm simulation field whereas 1.777 mm in following

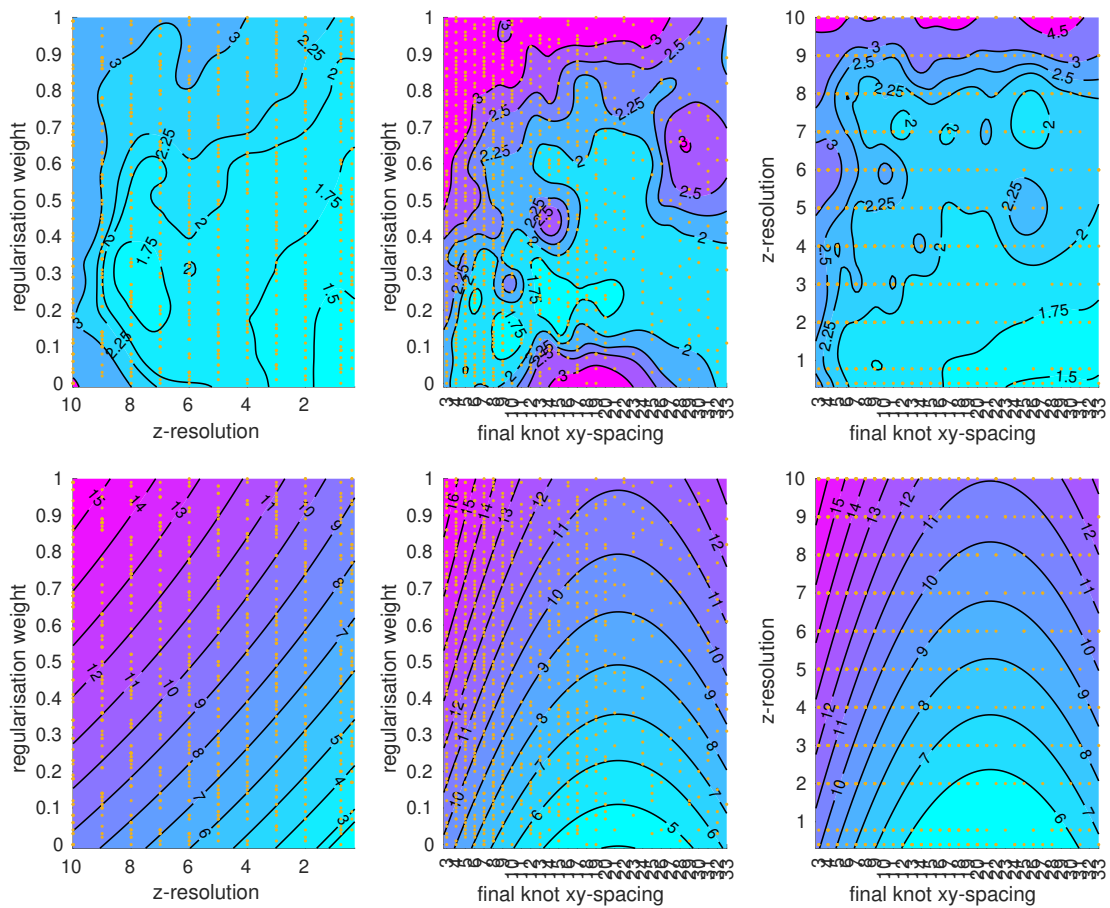


Figure 5.8: DRAMMS: surface plots showing the pair-wise distribution of the error metric (MNE, in [mm]) between the three most influencing parameters. On the top, results for the 10 mm; at the bottom, results for the 30 mm simulation. Yellow dots represent query points

the 30 mm one. The performance was considered acceptable as optimal values of the error metric were below 10% of the imposed displacement loads applied.

The three best performing elastic registration methods compared in this study showed overall similar optimal performance in the smaller 10 mm simulation, whereas differences were more marked in the larger 30 mm simulation. The optimisation was a decisive step especially in the 30 mm simulation, where the inter-quartile range of MNE values between parameter sets was 2.44 mm for the best performing method, showing a large difference between a successful and an unsuccessful registration call. The results show the importance of optimising the parameter to the specific deformation field to

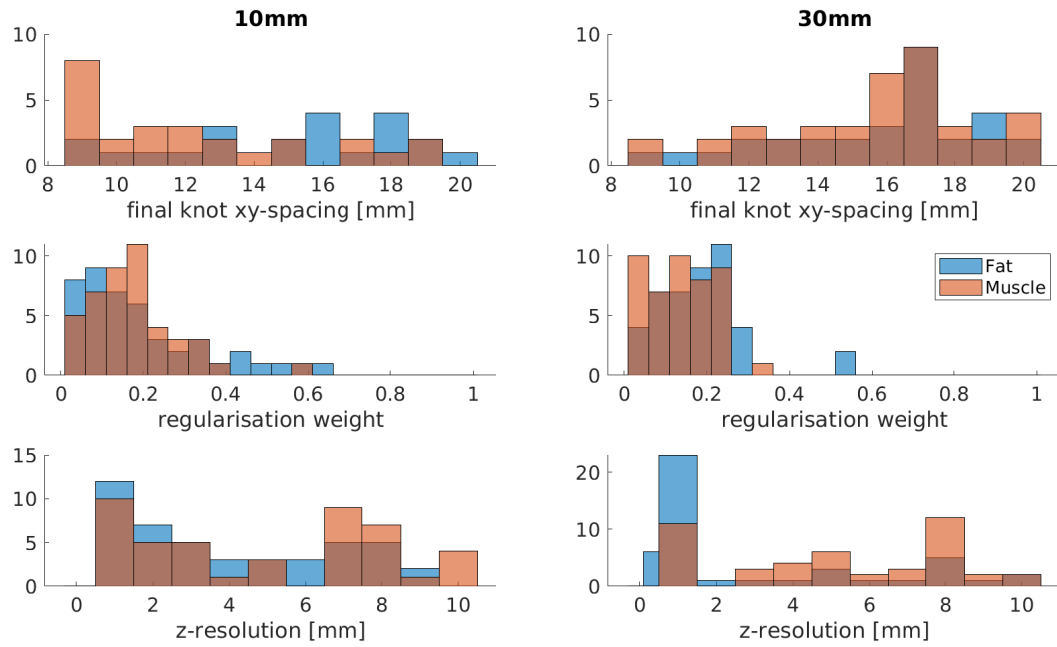


Figure 5.9: DRAMMS: histogram of the number of registration calls leading to MNE values below its 5<sup>th</sup>-percentile. On the left, results for the 10 mm simulation, whereas for the 30 mm simulations on the right. Histograms are reported for the three most influencing parameters, in blue in the fat area and in orange in the muscle

acquire, more so in the presence of large displacements.

Similar results were obtained by Schnabel et al. [120], where they applied a surface displacement field of 10 mm to MR breast images. Their results show an average MNE of 0.4 mm with maximum error between 2.4 and 10 mm. The top six algorithms evaluated in the EMPIRE10 challenge [71] showed average landmark distance scores of less than 1 mm, with a range from 0.66 to 0.99 mm, on different challenges including deformation of the lungs due to inspiration / expiration tests.

Similarly to Section 3.4, the sensitivity analysis showed primary importance of parameters controlling for grid spacing of the transformation model on the  $xy$ -plane in all the methods, explaining around 32% of the variability in the error metric. Comparing the two simulations, DRAMMS and *elastix* showed better performance with wider spacing in the  $xy$ -plane, more so in the 30 mm simulation. Opposite was the behaviour of SyN, whose best performance was associated to smaller spacing between control points.

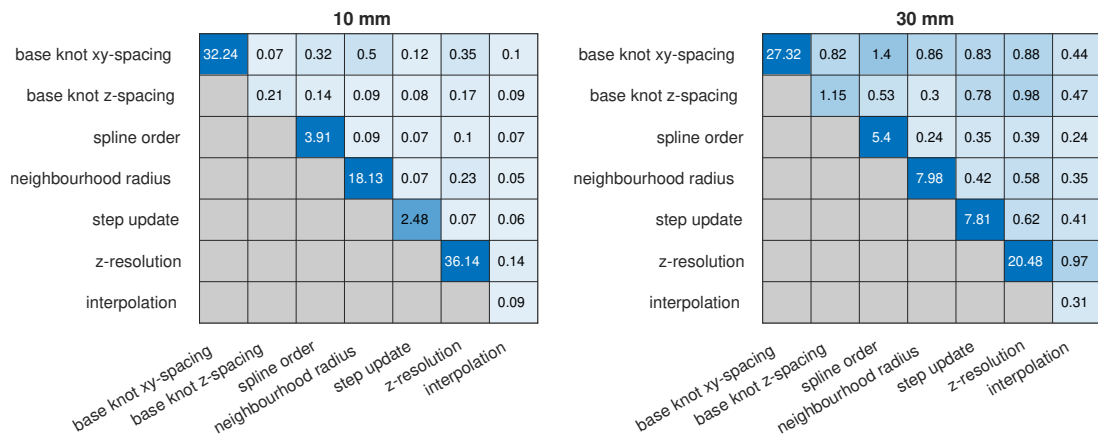


Figure 5.10: SyN: heatmap of the individual and joint sensitivity on the error metric (MNE). On the left, percentages relative to the total variance in the 10 mm simulation, whereas on the right for the 30 mm simulation ( $0.518632 \text{ mm}^2$  for the 10 mm simulation, and  $3.16815 \text{ mm}^2$  for the 30 mm one).

As expected, larger spacing between grid points was noticeable in the large displacements due to the deformation of the buttock under sitting load than the sub-millimetre redistribution of the brain tissue under the effect of gravity.

Resolution along  $z$  after deconvolution was the second most important parameter in all methods. This was confirmed by the larger component of the error along the  $z$ -direction relative to its projection onto the  $xy$ -plane. Without additional scans on an orthogonal plane, the ill-posed problem of image deconvolution degenerates into a trade-off between spatial (density of voxels) and intensity (sharpness of features) resolution, as the problem of reconstruction is bounded by the original dynamic intensity range of the images [193–195]. The very aggressive increase in resolution most likely introduced intensity averaging and partial-volume error [131]. However, the optimisation carried out showed that the quality or sharpness of features along  $z$  was of secondary importance in following smooth deformation fields such as the ones simulated from scans that were already well aligned together. The adverse effect of averaging and partial-volume error on the accuracy were clear with finer resolutions: this is showed in the surface plots for *elastix* (Fig. 5.14) and in the 10 mm simulation of DRAMMS (Fig. 5.8), where MNE increased with values of  $z$ -resolution below 2 mm. Regarding DRAMMS and SyN,



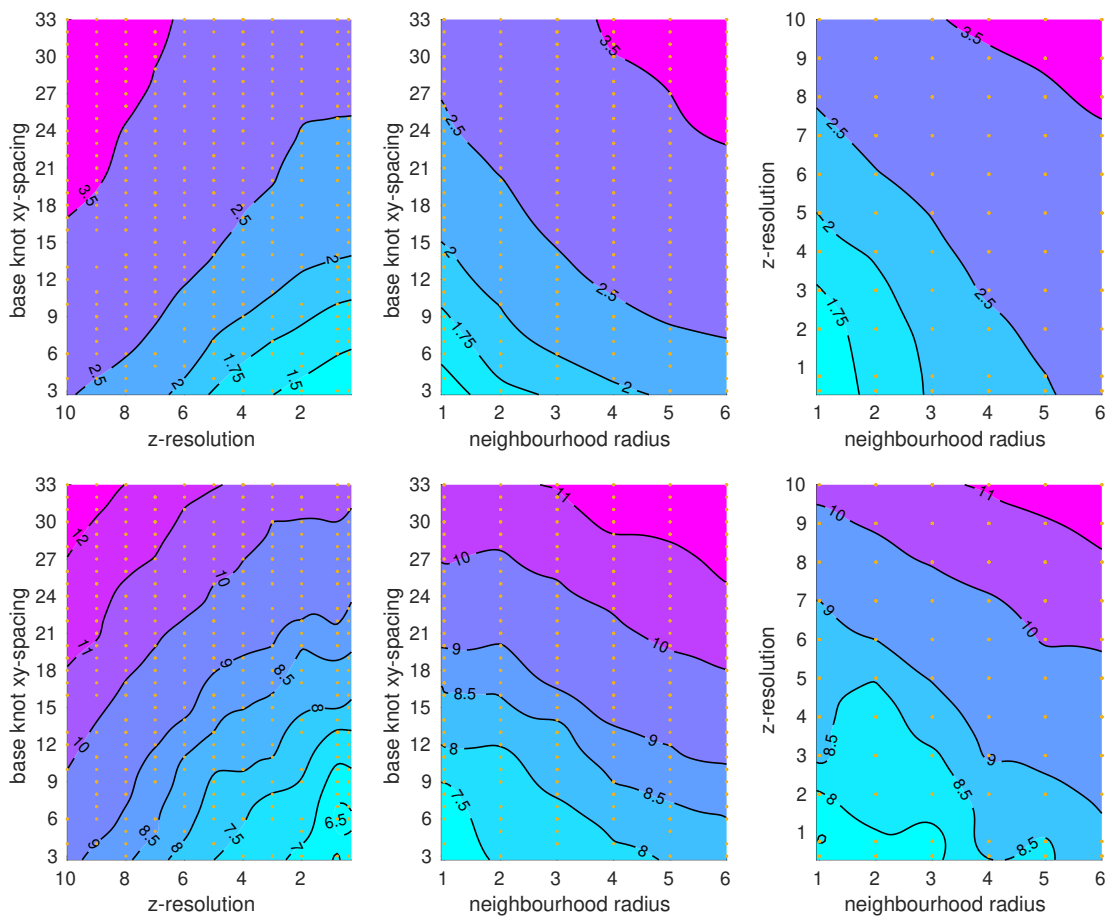


Figure 5.11: SyN: surface plots showing the pair-wise distribution of the error metric (MNE, in [mm]) between the three most influencing parameters. On the top, results for the 10 mm; at the bottom, results for the 30 mm simulation. Yellow dots represent query points

simulating finer resolutions resulted too demanding even for the cluster, with individual calls taking more than a week to complete.

Optimal values for  $z$ -resolution were around 4 mm for DRAMMS and *elastix*, whereas SyN showed better performance with smaller resolutions than the ones tested. This is contrast with the initial affine registration, where the original resolution proved to be the optimal spacing. As mentioned in the previous discussion section, the quality of the affine registration was greatly affected by any averaging of partial-volume effects introduced in the deconvolution process; this step greatly relied on the quality of the features to match, to limit the uncertainty in the correspondences and improve the

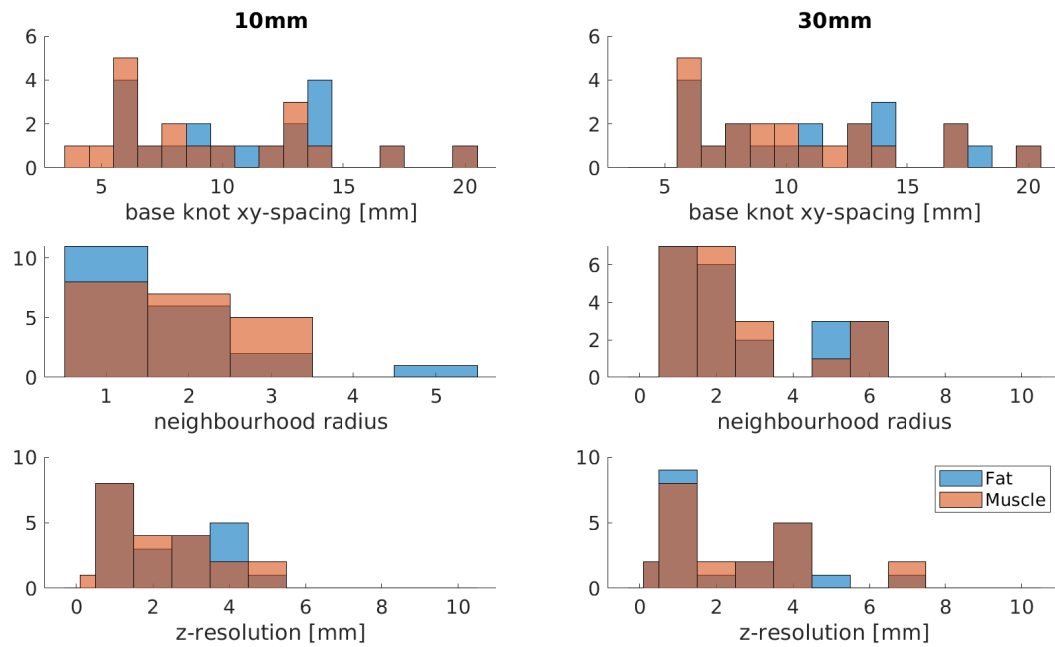


Figure 5.12: SyN: histogram of the number of registration calls leading to MNE values below its 5<sup>th</sup>-percentile. On the left, results for the 10 mm simulation, whereas for the 30 mm simulations on the right. Histograms are reported for the three most influencing parameters, in blue in the fat area and in orange in the muscle

accuracy of the alignment.

Sensitivity analysis showed that the coarser resolution of the images along  $z$  affected more the in-plane component of the transformation model than the components in the  $xy$ -plane: it is not surprising giving that the B-spline model depends on the three-dimensional distance of the voxels from the control points [196]. A denser voxel grid along  $z$  aided the registration methods in capturing the high spatial frequencies of in-plane components (that is,  $x$ - and  $y$ -components), more so in the presence of the larger displacements of the 30 mm simulation. Little was the interaction between  $z$ -resolution after deconvolution and the  $z$ -spacing of control points, showing that for the type of deformation investigated, the voxel spacing along  $z$  was enough to reconstruct the low spatial variability of the deformation field along the same direction (standard deviation in elevation angle of the 10 mm simulated field of  $1.53^\circ$  whereas  $1.02^\circ$  for the 30 mm one). The results therefore showed the importance of the off-axis resolution to the evaluation of in-plane components of deformation.

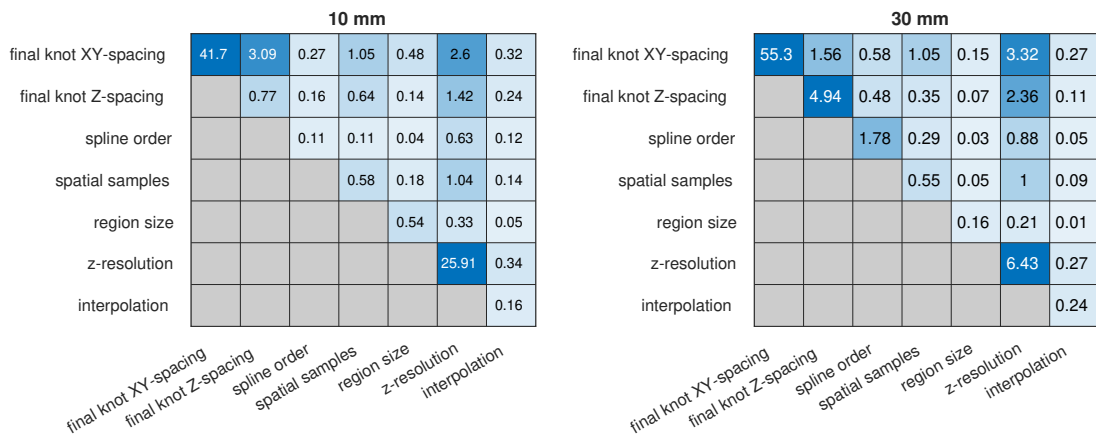


Figure 5.13: *elastix*: heatmap of the individual and joint sensitivity on the error metric (MNE). On the left, percentages relative to the total variance in the 10 mm simulation, whereas on the right for the 30 mm simulation ( $0.577863 \text{ mm}^2$  for the 10 mm simulation, and  $4.73588 \text{ mm}^2$  for the 30 mm one).

Although based on similar transformation models, the registration methods investigated showed differences in their behaviour. First, no penalty term on the transformation model was used in the calls to *elastix*. This made the parameters controlling for the B-spline grid spacing of *elastix* more decisive. DRAMMS showed better performance with lower values of regularisation weight, more so in the 30 mm simulation. This shows that regularisation constraints on the optimisation needs to be loose to let the transformation model free to follow the high variations of the deformation field tested. Finally, SyN showed worst performance in following the larger 30 mm displacement field, although being the best method for the DVC measurements of PBS. SyN did not have the flexibility to follow such deformation, as performance improved with decreasing values of *xy*-spacing, radius of the similarity window and *z*-resolution. Better performance was noticed with larger values of step update (not plotted), showing that larger advancements were needed to follow the large deformation fields, in particular the 30 mm one: higher values of the parameter should be included in the optimisation in future investigations. However, the computational cost of registration calls with low control grid spacing and high resolution were prohibitive even for the cluster.

Specifically for *elastix*, optimal grid spacing in the 30 mm simulation was associated

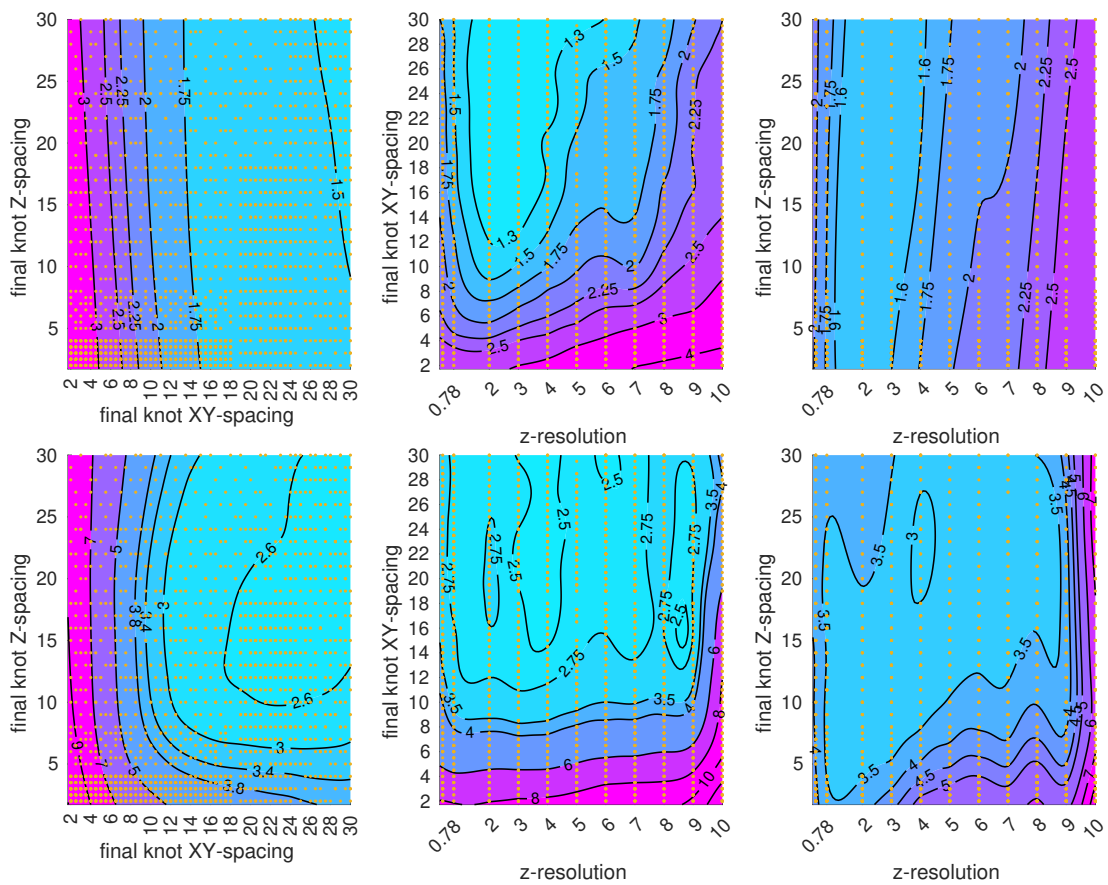


Figure 5.14: *elastix*: surface plots showing the pair-wise distribution of the error metric (MNE, in [mm]) between the three most influencing parameters. On the top, results for the 10 mm; at the bottom, results for the 30 mm simulation. Yellow dots represent query points

with larger spacings in both fat and muscle areas. In the 10 mm simulation, if on one hand the fat showed lower optimal grid spacing in particular along the  $z$ -direction, on the other, the muscle showed larger optimal spacing: stronger smoothness of the transformation model was needed to constrain its fluctuations given the lack of clear features in the area. Only blurred connective tissue surrounding muscle fascicles and blood vessels can be noticed.

Although the comprehensive optimisation, a limitation of the investigation is the representation of a single subject. This was done primarily to limit the number of registration calls to run. Moreover, anatomical differences were considered negligible relative to the large deformations simulated. To support this assumption, subject differences

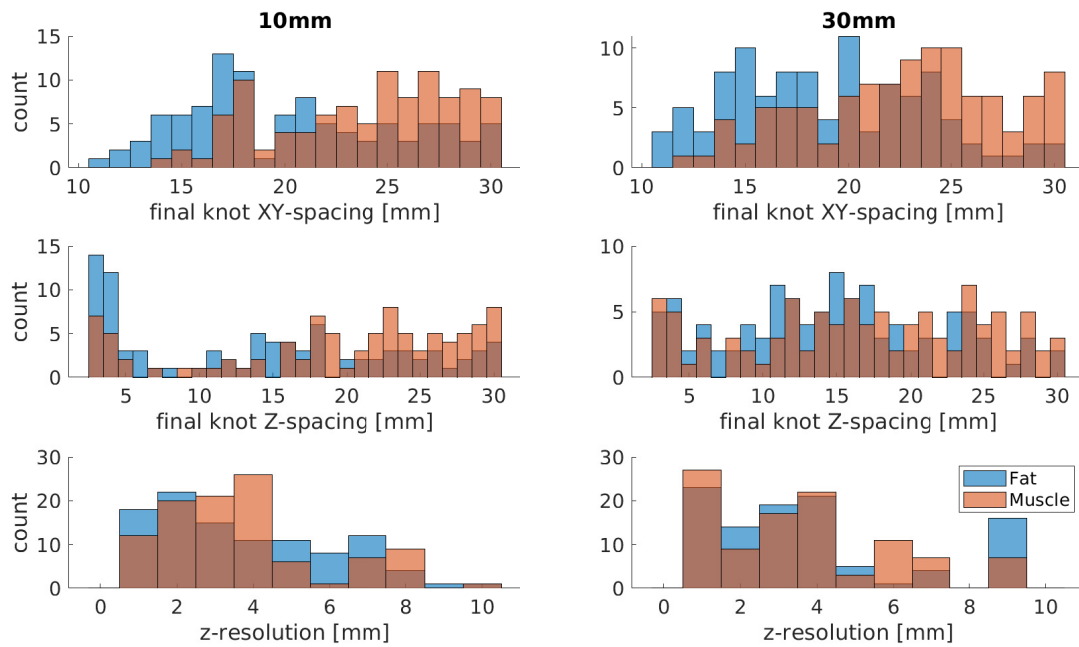


Figure 5.15: *elastix*: histogram of the number of registration calls leading to MNE values below its 5<sup>th</sup>-percentile. On the left, results for the 10 mm simulation, whereas for the 30 mm simulations on the right. Histograms are reported for the three most influencing parameters, in blue in the fat area and in orange in the muscle

in MNE values between the three modelled patients were almost negligible in the experimentation by Schnabel et al. [120] on breast tissue deformation. However, inter-subject variability affected the success of the registration calls in Section 3.4. Further investigation is therefore needed to quantify the effect of inter-subject variability on the performance of registration parameters.

## Summary

The chapter has aimed to evaluate the sources of inaccuracies related to the DVC measurements that will be investigated further in Chapter 6. These were identified as, similarly to Chapter 3, initial registration of skeletal elements and final deformable registration.

Regarding the initial registration of the pelvic elements, three affine registration methods

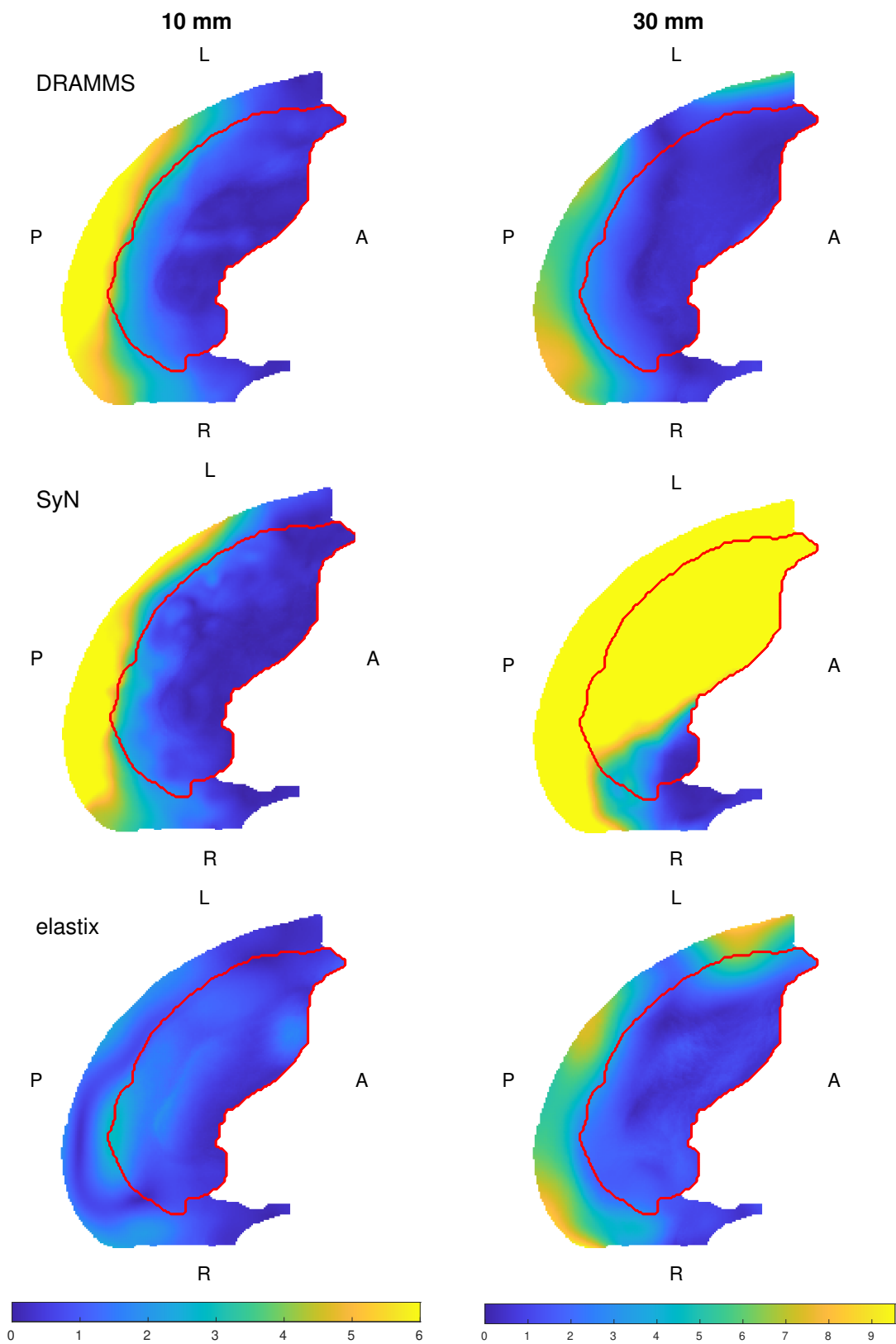


Figure 5.16: Distribution of the magnitude of the error vectors (in [mm]). On the left column, results from the 10 mm simulation; on the right column, from the 30 mm simulation. From top row to bottom, DRAMMS, SyN and *elastix*. The muscle area is outlined in red.

Parameter	10 mm	30 mm
	DRAMMS	
final knot $xy$ -spacing [mm]	9	17
$z$ -resolution [mm]	1	1
final knot $z$ -spacing [mm]	3	3
regularisation weight	0.25	0
samples in optimisation [mm]	3	8
interpolation to voxel grid	2	2
interpolation	BSpline	BSpline
	SyN	
base knot $xy$ -spacing [mm]	6	6
$z$ -resolution [mm]	1	1
base knot $z$ -spacing [mm]	25	22
neighbourhood radius	1	1
step update [mm]	0.28	.28
spline order	2	3
interpolation	BSpline	BSpline
	<i>elastix</i>	
final grid $xy$ -spacing [mm]	17	20
$z$ -resolution [mm]	3	4
final grid $z$ -spacing [mm]	3	20
spatial samples	$3.4e3$	$3.6e3$
region size [mm]	82	58
spline order	3	3
interpolation	BSpline	sinc

Table 5.3: Optimal parameter set for each deformable registration method tested.

were optimised in order to obtain the best alignment between segmentations of the pelvis in two different stages of deformation in 10 subjects. Results differed mostly between subjects, with similar performance of the methods: optimal parameters led to a maximum DC value of 0.92%, whereas a minimum of 0.70%; minimum HD values, instead, was 3.98 mm, whereas 6.99 mm for the maximum.

Regarding the DVC measurements, instead, three deformable registration methods for medical imaging were optimised against two ground truths representing the deformation of the human buttock under sitting loads. The optimal parameter set led to a final accuracy of 0.989 mm in following the smaller 10 mm simulation field whereas 1.777 mm

Regions		10 mm	30 mm
Fat	Ground truth	$6.0061 \pm 2.6942$	$15.0986 \pm 8.3525$
	DRAMMS	$2.4920 \pm 2.3732$	$3.0561 \pm 3.3613$
	SyN	$2.3780 \pm 2.4367$	$7.6140 \pm 8.0717$
	<i>elastix</i>	$1.3302 \pm 1.2548$	$2.8347 \pm 2.9244$
Superficial muscle	Ground truth	$6.2870 \pm 2.0925$	$17.1096 \pm 6.8749$
	DRAMMS	$1.3345 \pm 1.4924$	$1.3643 \pm 1.0765$
	SyN	$1.0682 \pm 1.3120$	$6.8645 \pm 7.6530$
	<i>elastix</i>	$1.1684 \pm 0.9498$	$1.4405 \pm 0.9990$
Deep muscle	Ground truth	$4.3940 \pm 3.1363$	$11.0040 \pm 7.5872$
	DRAMMS	$0.3373 \pm 0.2873$	$0.9853 \pm 0.9437$
	SyN	$0.2712 \pm 0.3039$	$5.9120 \pm 7.8942$
	<i>elastix</i>	$0.4693 \pm 0.4381$	$1.0556 \pm 0.8755$

Table 5.4: MNE values corresponding to the optimal parameter set, for each registration method. Values are extracted in the following ROIs: fat, superficial muscle and deep muscle. Values of the ground truth are also reported for comparison.

against the larger 30 mm one. Although not satisfying the recommended accuracy for DVC measurements in the biomedical field [17], inaccuracies were below 10% of the simulated displacement fields applied.



# Deep Tissue Injury: Digital Volume Correlation

## Overview

This chapter describes the measurements taken from a dataset depicting two stages of the progressive deformation of the buttocks under body load via digital volume correlation (DVC). Measurements were taken from MR data acquired in a previous study on healthy individuals in a semi-recumbent position [1]. To the best of the author's knowledge, this is the first study capturing the local and global distribution as well as the three-dimensional nature of such deformation. Previous studies depicted only but a limited representation of the complexity of the phenomenon, by way of thickness measurements from MR scans [1, 10, 11, 13, 184], motion capture data [188] and digital image correlation on ultrasound images [189]. This dataset is invaluable for the thorough design and verification of FE models simulating sitting positions and ultimately for the advancement of systems for the prevention and control of DTIs.

The work presented in this chapter will be part of the main body of the following draft to be submitted soon to the Journal of Biomechanics:

Zappalà, S., Bethany E. K., Marshall, D., Wu J., Evans S. L. & Al-Dirini M. A. R.. Volumetric redistribution of the soft tissues in the human buttock captured from MR *in-vivo* scans: accuracy of measurements and analysis of deformation.

Section 6.2 describes the registration pipeline, beginning with the affine alignment to set the initial conditions of deformations, followed by the DVC measurements based on the optimal method and parameter set identified in Chapter 5.

Finally, results of the analysis of deformation is shown in Section 6.3, which clinical implications are then discussed in Section 6.4.

## 6.1 Introduction

The accuracy and reliability of computational models replicating the large deformations of the buttock due to sitting relies on the availability of volumetric measurements to represent the complexity of the phenomenon, by providing dense measurements of displacement to identify appropriate parameter values against or to validate the accuracy of the prediction of computational.

The pattern of deformation is reported to be mostly displacement and redistribution of tissues rather than volumetric deformation, given their incompressibility [185]. Muscle thickness was reported to greatly reduce under the effect of load in the study by Son-enblum et al. [12], by sliding away from the ischium under sitting loads, increasing the thickness of the tissues in surrounding areas (lesser trochanter and femoral head) [185]. This slide, which was measured to happen along both the I-S and R-L directions [185, 197], leaves very little of the gluteus maximus under the ischium during sitting [13], leading to the fat tissue holding the pressure of the IT. This results was afterwards confirmed by other studies [169, 185].

Large variations in the mechanical response due to differences in anatomy were reported, both between genders [198] and between able-bodied and SCI individuals [199]. Strong variability between subjects due to differences in anatomy such as tissue composition and bone shape [169], fat thickness [184] and body weight [10, 185] were identified. The study by Harry et al. [188] showed that mass, waist depth, hip depth, hip breadth,

hip girth and percentage of fat had moderate to strong correlation with 12 compression variables acquired with motion sensors.

Imaging studies that aimed at capturing the deformation were based on volume change in a specific ROI [169, 184], or tissue thickness between loaded and unloaded conditions [1]. Experimental *ex-vivo* tissue testing [10, 180, 200, 201] or inverse identification on deformation data on localised measurements [181, 187] were used to identify parameters; finally, validations of computational models were mostly based on alignment of prediction to MR scan [197, 202], tissue thickness between loaded and unloaded conditions [181] or pressure distribution at the seating interface [10]. The need for a rich set of 3D measurements has been reported in many studies [1, 184–186], as the aforementioned measurements cannot fully represent the deformation at more internal structures [187].

## 6.2 Methods

### 6.2.1 MR Dataset

As part of a previous study [1], magnetic resonance (MR) scans depicting the quasi-static deformation of gluteal soft tissues of ten healthy male subjects (aged 19-39, BMI =  $28.02 \pm 4.71 \text{ kg/m}^2$ ) sitting in a 1.5 T scanner in a semi-recumbent position were acquired. A schematic of the acquisition protocol is reported in Figure 6.1, taken from Al-Dirini et al. [1]. The buttocks of each subject were scanned in an undeformed, partially deformed and deformed state. The right side of the buttock remained in a weight bearing position, whilst three 10 mm inserts were removed from beneath the left buttock to capture the deformation of the soft tissues. The following states of deformation were therefore simulated: non-, partial- and full-weight bearing (WB) loads. Further details can be found in Al-Dirini et al. [1].

Proton density weighted spin echo scans (TR=4542 ms, TE=32.18 ms), with an an-

isotropic resolution of  $0.78 \times 0.78 \times 10 \text{ mm}^3$  over a field of view of  $401 \times 400 \times 481 \text{ mm}^3$  including the hips and part of the thighs were analysed in this study. A single observer manually segmented (*Simpleware ScanIP*) the gluteus maximus and subcutaneous fat, which were considered regions of interest (ROIs).

## 6.2.2 DVC Measurements

Initial conditions of deformation were imposed by aligning the femoral head on the side undergoing deformation (to include the left greater trochanter (GT)), as well as both the left and right inferior pubic rami (to include the left ischial tuberosity (IT)). The aim was to compensate for the residual pelvic tilt in the dataset, reported to be below  $6^\circ$  [1]: any residual misalignment between these skeletal elements was captured as an additional component of deformation by the deformable registration. Affine registration was carried out with *elastix*: details of the optimisation of this step can be found in Section 5.2. The full-WB scans were chosen as subject references, given the consistency in the posture between subjects. The progressive deformation was extracted by morphing the non-WB scan of each subject to the partial-WB and the latter then to the full-WB scan.

A linear approximation of the deformation gradient,  $\mathbf{F}$ , was evaluated using maximum likelihood estimation [66] with a radius of the strain windows matching the optimal B-spline spacing after optimisation. The Green-Lagrange strain tensor,  $\mathbf{E}$ , was extracted as [153]:

$$\mathbf{E} = \frac{1}{2} (\mathbf{F}^T \mathbf{F} - I) \quad (6.1)$$

where  $I$  is the identity matrix.

The maximum compressive strain and maximum shear strain ( $\gamma_{max}$ ) were extracted as the minimum eigenvalue of the strain and the absolute difference between the maximum and minimum principal strains, respectively [15, 176]. Both are considered as indicators of tissue damage, with  $\gamma_{max}$  having shown a monotonic relationship with tissue damage

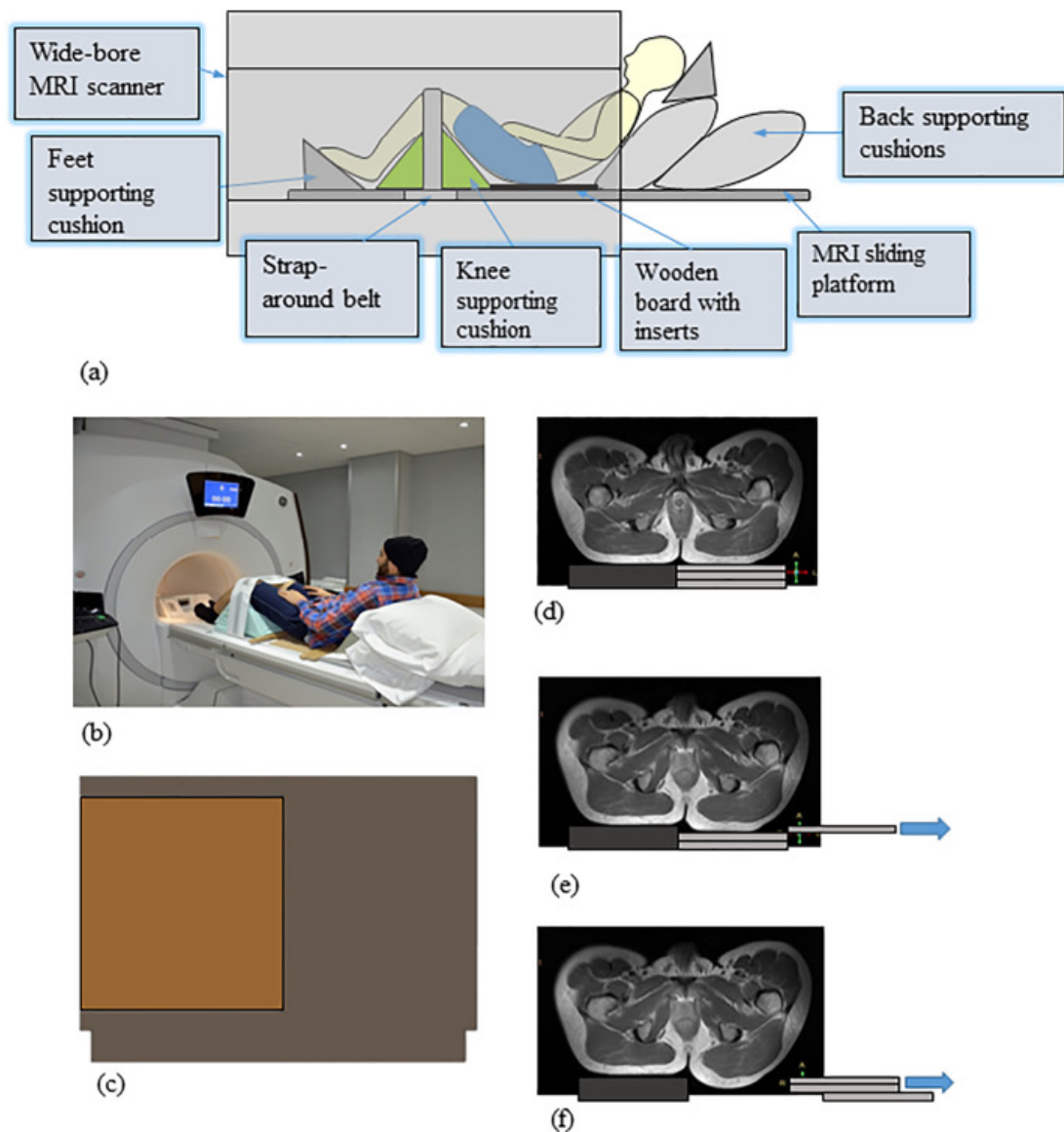


Figure 6.1: Illustration of the acquisition set-up. On the top (a), schematic representation of the positioning of the subject in the bore of the scanner during acquisition; below on the left (b), photograph from one of the scanning sessions. An axial view of the wooden board used to support the buttocks is reported in (c): the 10 mm removable inserts used to reproduce the progressive stages of deformation are represented in light brown colour. Coronal views of the MR scans for the full-WB (d), partial-WB (e) and non-WB (f) conditions are reported on the right. Taken from Al-Dirini et al. [1]

after initiation [203].

## 6.3 Results

**Analysis of deformation** Results presented throughout the paper are in anatomical space: right-left (R-L) represents the medial-lateral direction, posterior-anterior (P-A) the ventral-dorsal and finally inferior-superior (I-S) the caudal-cranial direction. Figure 6.2 shows the initial conditions of deformation, as results of the registration of the pelvic elements. Average Dice coefficients (representing the percentage intersection between the aligned masks) were 80% in the alignment of the pelvic elements between partial-WB and full-WB and 79% for the non-WB to full-WB (where 60% and 80% can be considered acceptable for small and large structures, respectively [79]).

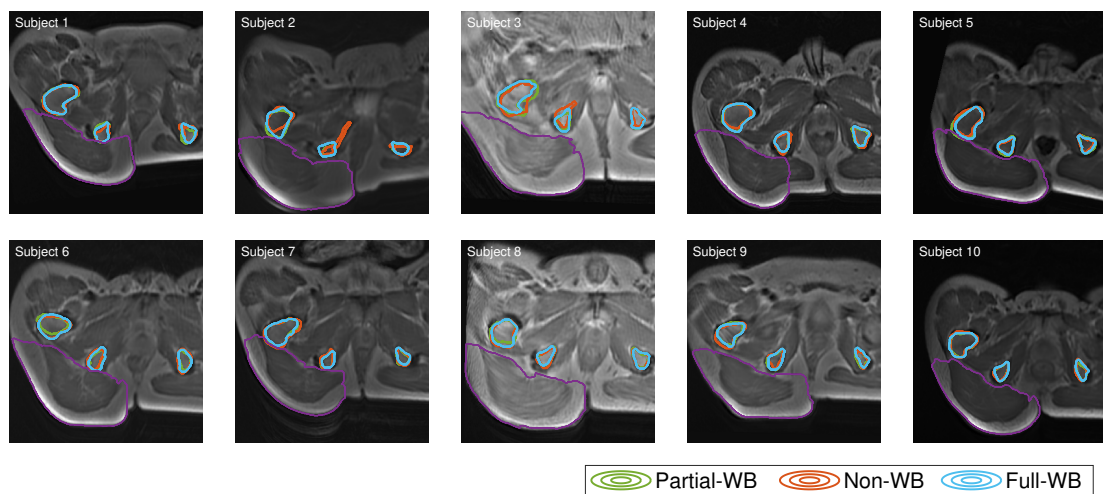


Figure 6.2: Axial views of the initial alignment of the pelvic elements. The masks of the pelvis for the full-WB condition are delineated in blue, in green for the partial-WB and in orange for the non-WB scans. In purple, the muscle and fat areas are delineated as reference.

Displacement maps for each subject are reported in Figure 6.3, with average and standard deviation values in a few selected ROIs in Figure 6.4. The most prominent component was the P-A one, which occurred predominantly in the first stage of deformation (non- to partial-WB). Displacement was bigger below the I-T than below the GT in both stages of deformation. Displacement along the R-L and I-S directions were noticeable, in particular in the superficial medial ROIs. Patterns of deformation were very different between subjects, in particular alongside the R-L and I-S directions.

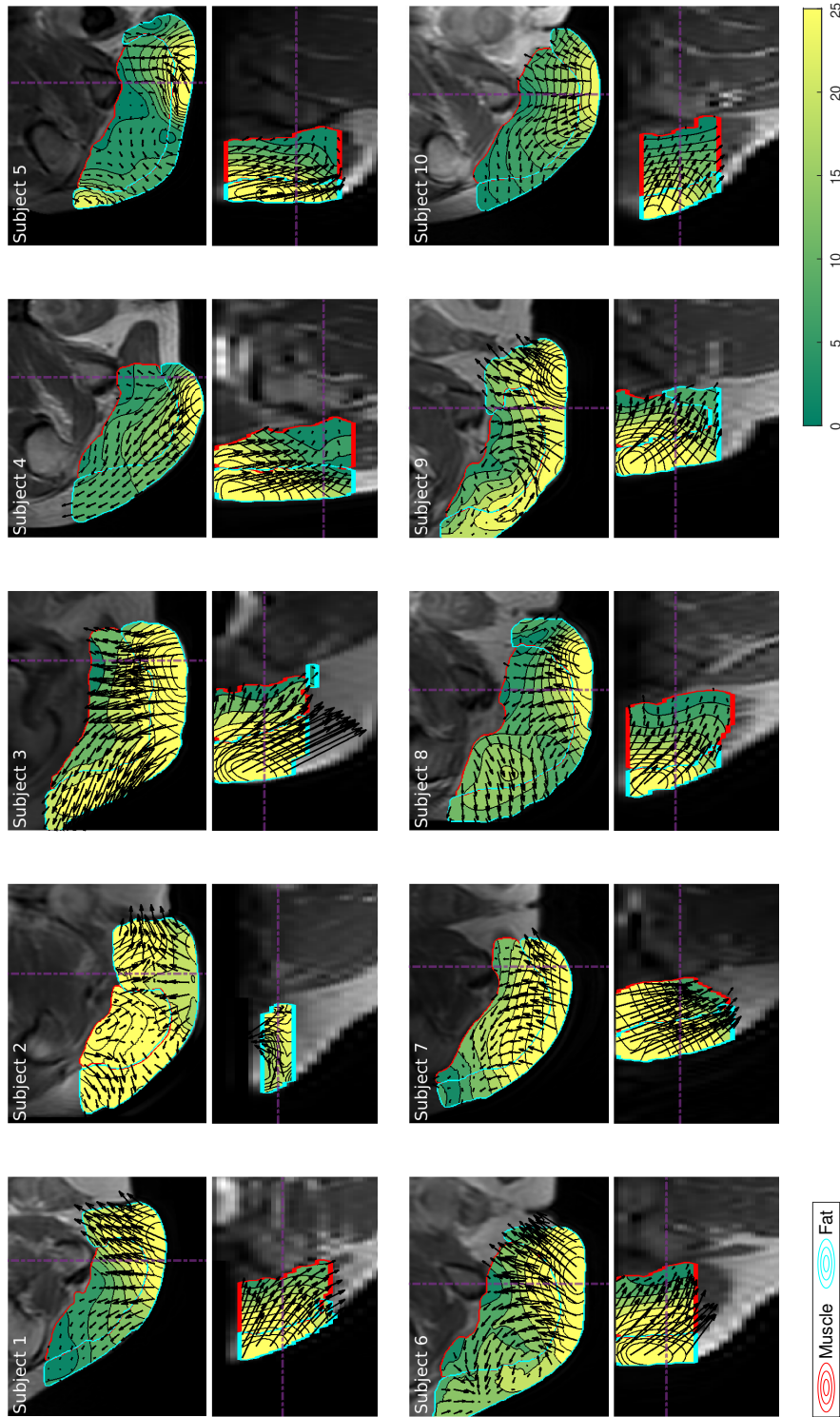


Figure 6.3: Axial (top) and sagittal (bottom) views of the displacement field for all the analysed subjects. Arrows show the direction of displacement vectors for both stages of deformation, that is, non-WB to partial-WB and partial-WB to full-WB. Length of vectors is scaled for visualisation purposes: the magnitude of the deformation from non-WB to full-WB is represented by the colormap. Fat and muscle ROIs are reported for reference. Axial and sagittal slices are located at the centre of the IT: for reference, the purple dotted line in the axial views show the location of the corresponding sagittal slice and vice-versa for the sagittal views.

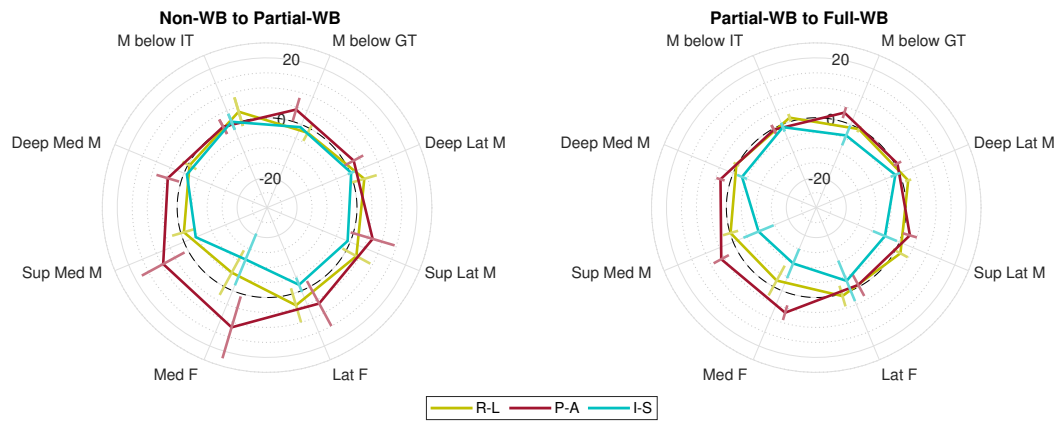


Figure 6.4: Polar plot of the main components of the displacement field (right-left (R-L), posterior-anterior (P-A) and inferior-superior (I-S)) for the two stages of deformation analysed. Average values (here reported in [mm]) were evaluated over few ROIs (alongside their standard deviation between subjects): Medial Fat, Superficial Medial Muscle, Deep Medial Muscle, Muscle below IT, Muscle below GT, Deep Lateral Muscle, Superficial Lateral Muscle, Lateral Fat.

Figure 6.5 shows the distribution of compressive strain for the overall deformation (non-to full-WB). Polar plots of the components of the strain tensors (Figure 6.6) show an overall higher compression state of the tissues in the first stage of deformation. The P-A component of strain was predominant, with corresponding expansion in the other directions. Compression state of the deep muscle closer to the GT was generally higher than the compression below the IT.



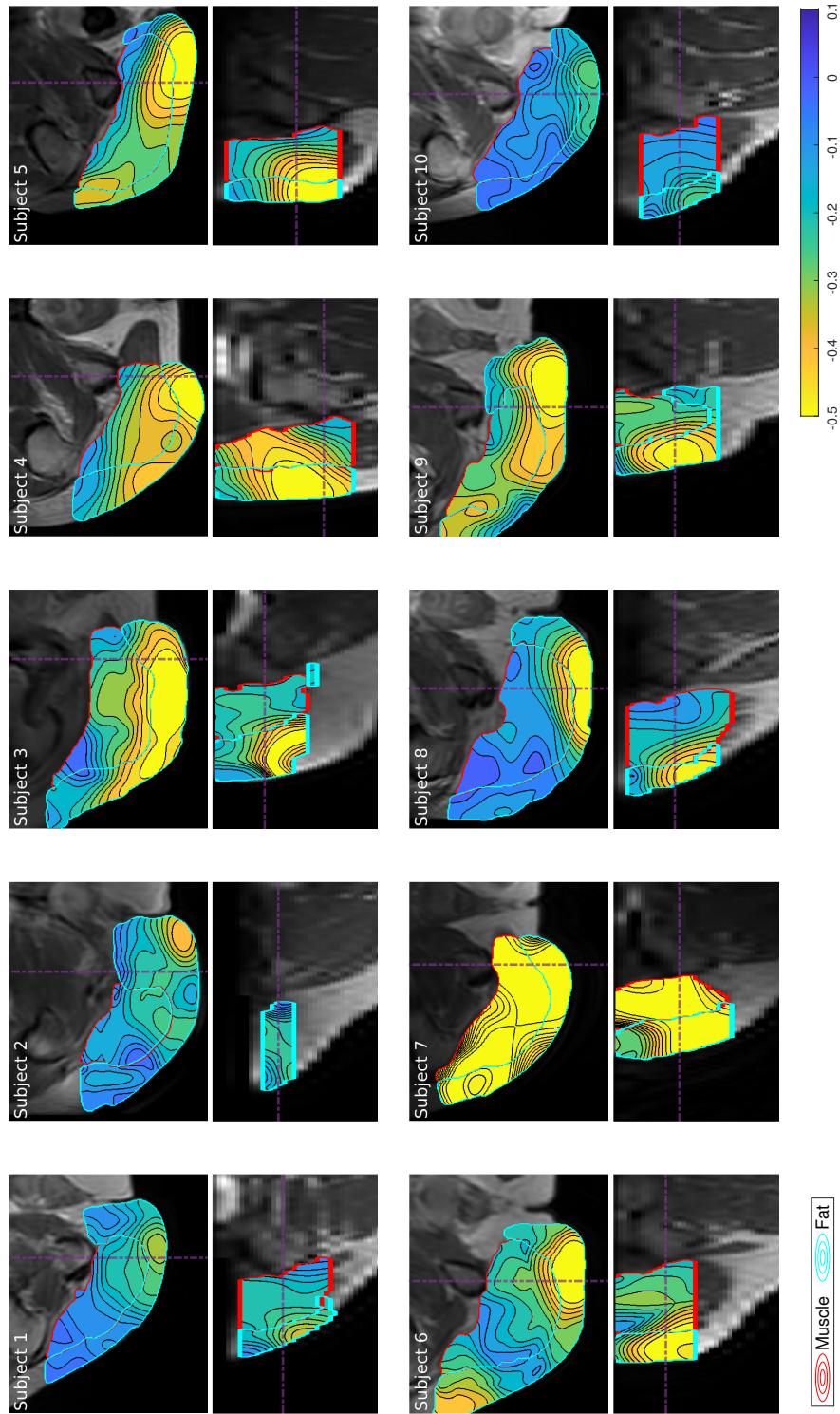


Figure 6.5: Axial (top) and sagittal (bottom) views of the distribution of the maximum compressive strain for the full deformation (non- to full-WB). Fat and muscle ROIs are delineated in turquoise and red, respectively, for reference. Axial and sagittal slices are located at the centre of the IT: for reference, the purple dotted line in the axial views show the location of the corresponding sagittal slice and vice-versa for the sagittal views.

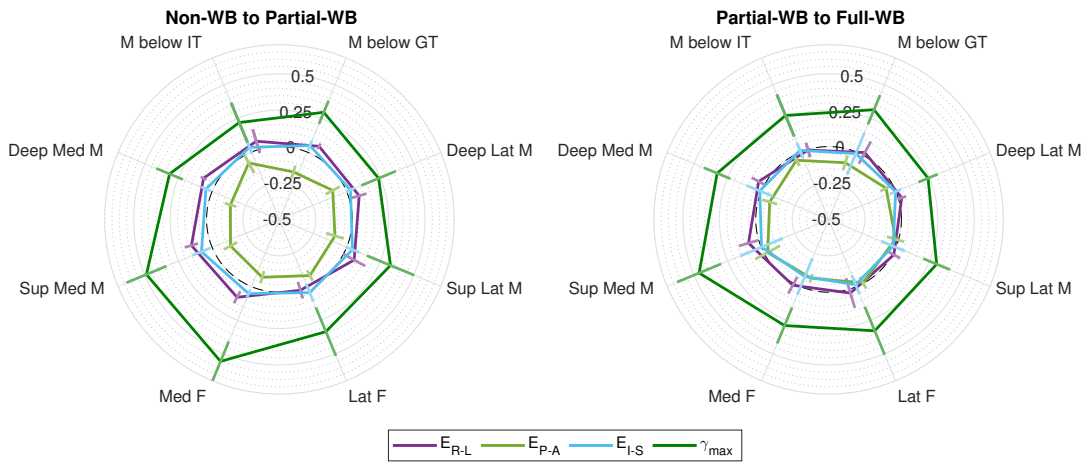


Figure 6.6: Polar plot of the main components of the Lagrangian strain tensor ( $E_{L-R}$ ,  $E_{P-A}$ ,  $E_{I-S}$ ) and the maximum shear strain ( $\gamma_{max}$ ) averaged over few ROIs: Medial Fat, Superficial Medial Muscle, Deep Medial Muscle, Muscle below IT, Muscle below GT, Deep Lateral Muscle, Superficial Lateral Muscle, Lateral Fat.

The average spatial evolution of  $\gamma_{max}$  between subjects was evaluated along a vertical line from the IT and to the seat interface (Figure 6.7). The first stage of deformation showed a peak in the fat area, which was 1.6 times the peak of the second stage. Moreover, the latter was located more towards the superficial muscle. After the peak, values monotonically decreased towards the IT.

## 6.4 Discussion

The aim of the study was to further expand the work by Al-Dirini et al. [1] by extracting the three-dimensional distribution of the progressive deformation of the buttock due to sitting in 10 healthy individuals. The obtained measurements add novelty to existing experimental values in the literature [1, 10, 184, 188, 189, 197, 201, 202] by depicting *in-vivo* the volumetric deformation field of the whole buttock area, providing useful insight into the global and local compression state of the soft tissues. The accuracy of such measurements was assessed by optimising three deformable registration methods against two biomechanically plausible ground truths representing large deformations (10 mm and 30 mm displacement load), generated via a simplified FE model (Section 5.3). The

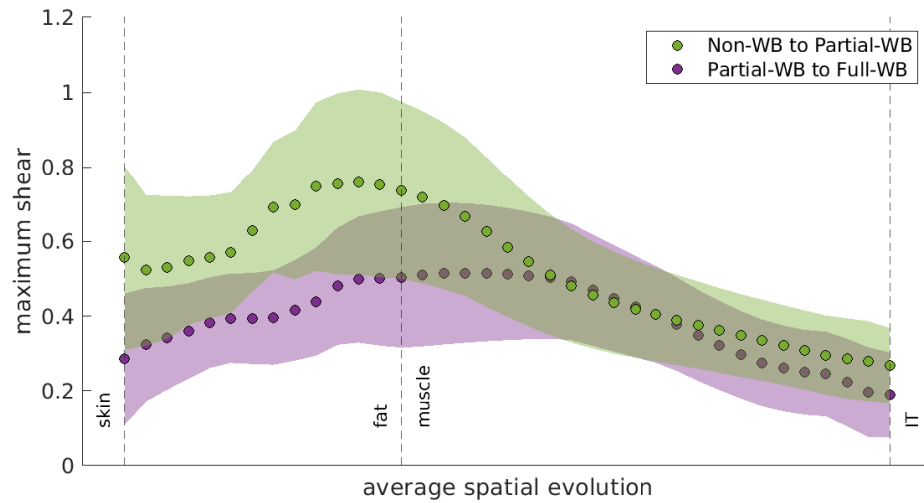


Figure 6.7: Spatial evolution of  $\gamma_{max}$  in the first (non- to partial-WB) and second (partial- to full-WB) stage of deformation. Curves represent average between subjects, whereas shaded areas the corresponding inter-subject variability.

best registration method alongside its optimal parameter set gave an overall accuracy of 0.99 mm against the 10 mm simulation, whereas 1.78 against the 30 mm one. The acquired pattern of deformation was in line with the previous literature: a prevalent redistribution of the tissue was captured, with larger deformation below the IT than below the GT [1, 204, 205], and a noticeable off-axis shift of the gluteal muscle [184, 189].

Below the IT, the superficial muscle showed both displacement and compression along the P-A direction in the first stage of deformation. The fat, instead, alongside the same sagittal compression, showed a slide of the tissue (approximately 11 mm) towards the inferior direction that was not associated with any compression state. In the second stage of deformation (partial- to full-WB), the overall P-A displacement was smaller, with now both fat and superficial muscle showing a noticeable shift towards inferior direction. In this stage, however, the fat showed I-S compression, probably caused by redistribution of surrounding tissue that restricted the fat laterally. The superficial muscle showed no increase in its compression state, depicting a sliding of tissue of around 7 mm away from the IT.

The deformation below the GT showed a general compression along the P-A direction in the first stage of deformation, with high values located at the muscle just below the GT. The second stage of deformation showed again a slide of the superficial muscle with no noticeable compression state. The measured shift of the superficial muscle below both the IT and GT confirms and quantifies the lateral and posterior sliding of the gluteal muscle tissue reported in the literature, which led to it being little if not loaded by the IT during scanning (especially in wheelchair users), leaving fat, ligaments and tendons to withstand the load [12, 13, 169, 184, 189]. The muscle did not slide completely off the IT in the present study due to the semi-recumbent posture imaged [13, 189]: this result suggests that semi-recumbent and lying positions might be preferable over a sitting one to redistribute the load over a thicker layer of tissues [186]. The complexity of the deformation evaluated in the present study showed the limit of simplified FE models disregarding off-axis deformation, representing only but a small part of the buttocks, or missing an adequate characterisation of the interaction between tissues [13, 181].

Although comparison is limited by methodological differences, acquired values of  $\gamma_{max}$  suitably fit between the literature on the deformation of the human buttock due to sitting and due to lying: Doridam et al. [189] reported values of shear strain above 75% on average from DIC measurements on ultrasound data of 7 healthy subjects sitting on a stool; Linder-Ganz et al. [186] reported average  $\gamma_{max}$  strain around 90% and 41% in the fat and muscle layers, respectively, in sitting healthy participants; finally, a MR-validated FE simulation of healthy subjects lying on a hard spine board generated values up to 0.8 [202]. In our study, the muscle area showed a consistent  $\gamma_{max}$  of around 0.4 in both stages of deformation, with an average peak of 0.8. The fat layer, instead, appeared to take most of the shear strain in the first stage of deformation, possibly responding to load with an increased stress state during the second stage [1].

The spatial evolution of the  $\gamma_{max}$  on the path from the skin to the IT showed a similar trend to the FE prediction by Oomens et al. [176]. Differently from the simulations, the peak in the second stage shifted towards the superficial muscle and curves monotonically

decreased towards the IT. The peak in the first stage of deformation was 1.6 times the one in the second, suggesting that onset of damage could be associated more to the initial redistribution of soft tissues under the effect of partial weight than due to the compressive effect of the full-weight load.

Values of shear strain the present study, alongside other works on human subjects [176, 186, 189], exceeded the thresholds of 45% max compressive strain and 75%  $\gamma_{max}$  based on mechanical indentation of the tibialis-anterior of a rat model [203]. Although a comparison is limited by the lack of evaluation of the state of the tissue after scanning and by the differences in the duration of the load, these results point towards an adjustment of those thresholds for human subjects [189].

Results showed the complexity of the phenomenon affected by differences in posture and anatomy. Subjects 1 and 5 dropped the left side of the hips after boards were removed, leading to different directions of gravity between scans; subjects 3, 6 and 9 touched the seat in the non-WB position, resulting in residual load on the left buttock; subject 8 showed fat infiltration [1], which affected the overall mechanical response of the surrounding tissue [201]. Moreover, the population sample was characterised by diverse BMI values, partly explaining the anatomical differences between subjects found in the estimated fields. The study shows the importance of the effort in isolating the effect of each of these factors on the deformation of the buttock area, with improved repeatability of experimental set-ups or with more selective recruitment.

The spurious fluctuations captured in the displacement and strain fields can be associated to inaccuracies in the calculations, which left the transformation model relying on its smoothness constraints. First, high-frequency content of large displacements can be lost in the cross-correlation process due to the low-pass effect (that is, averaging effect) of its formulation [24]. The window formulated by Nogueira et al. [63] has been shown to improve the reconstruction of high-frequency spatial components. Second, a first order approximation of the deformation gradients (used in the present study) was shown to be inaccurate in the presence of high strain gradients or at edges and corners, relative to a

second-order approximation including quadratic terms of the gradient expansion [66].

Finally, the semi-recumbent position chosen for the scanning had the limitation that the pelvis was not located at the isocentre of the scanner. MR distortions are known to affect scans by introducing a spurious warping, which magnitude increases further away from the isocentre [86, 87, 89, 90]: studies on 1.5T scanners reported distortions after correction below 2 mm [86, 88, 119]. MR distortions were evident at the top slices of the scans at the level of the superior pubic rami, even after distortion correction.

## 6.5 Data Availability

The dataset generated during and/or analysed during the current study is going to be made available in the following OSF repository. Displacement and the strain maps extracted in the present work are going to be available for other researchers to use.

### Summary

This chapter demonstrated the complexity of the deformation of the buttock due to semi-recumbent sitting: the captured three-dimensional measurements extensively depicted the local and global deformation of the subcutaneous tissues, affected by differences in anatomy and posture.

On a global scale, the analysis of deformation allowed the quantification the slide of the gluteus maximus that was reported in the literature: the muscle displaced downwards away from both IT and GT of about 11 mm in the second stage of deformation, whereas the fat shifted inferiorly from the IT of about 12 mm in both stages of deformation.

On a local scale, the maximum shear  $\gamma_{max}$  showed maximum value at the fat-muscle interface in a path from the skin to the pelvis at the level of the IT. After the peak,  $\gamma_{max}$  monotonically decreased towards the IT. The same behaviour was shown in both stages

of deformation, with a peak in the first that was 1.6 times the peak in the second stage; this showed that high values of maximum shear (as predictor of tissue damage) were more related to the initial tissue redistribution under the effect of partial-weight, than to the shear caused by the effect of full body load.

The study showed the complexity of the deformation, composed by a large component of tissue shifting and tissue deformation. Results showed the limitation of simplified FE models disregarding off-axis deformation, representing only but a small part of the buttocks, or missing an adequate representation of the soft tissues involved in the deformation.

The study provides a selection of rich and comprehensive displacement fields of 11 healthy subjects (that will be made freely available) for the verification of FE models. Considerable effort was therefore made to keep assumptions on the estimated deformation field as minimal as possible, alongside quantifying the margin of error of the measurements. It is hoped that such an unbiased dataset can be crucial for the verification of FE models aimed at providing a straight answer towards the usability of such models in a clinical practice.

## Conclusions and Future Work

In this chapter, the research questions will be restated and reflected upon, relating them to the corresponding contributions described in the above chapters. Limitations of the work will be discussed to suggest some directions for future development. Finally, the chapter ends with overall observations and conclusion of the thesis.

### 7.1 Research Questions and Contributions

The following overarching hypothesis was presented in Chapter 1: *deformable registration methods for medical imaging have the accuracy and flexibility to capture, on a global and local scale, the small and large displacement of soft tissues in physiological conditions.*

The availability of rich data representing the global and local mechanical response of soft tissues can improve our understanding of their behaviour and point towards further advancements of surgical and preventive clinical systems. Considerable effort was made to keep minimal assumptions on the estimated displacement field, alongside optimising the measurements to the specific deformation. The datasets of full-field DVC measurements based on minimal assumptions are a valuable benchmark for the unbiased design and validation of biomechanical computational models to use in a clinical setting [14, 16, 17].

The benefit of datasets of DVC measurements and the reliability of any conclusions



drawn from these deformation maps depends on the accuracy of the calculations. The assessment of accuracy of DVC calculations capturing the deformation of soft tissues *in-vivo* has not been explored completely [16, 17]. As a first step towards understanding the error related to such measurements, the suitability of deformable registration methods for medical imaging was initially investigated, as these have been designed to capture the small and large differences in anatomy due to inter-subject variability mostly from *in-vivo* MR scans.

Accuracy was assessed against both the small deformations of the brain tissue under the effect of gravity and the large deformations of the buttock due to sitting. As introduced in Chapter 1, *in-vivo* MR DVC calculations are complicated by the limited resolution of the images that can be acquired *in-vivo* without compromising the comfort of the subject or without them being affected by image blurring due to subject motion. Moreover, capturing displacements smaller than the voxel spacing relies on suitable *a-priori* constraints on the search strategy and the deformation model. When capturing large deformations, on the other hand, the approximations and the assumptions which the deformable methods rely on can introduce inaccuracies in the estimated displacement field. First, measures of similarity between scans to align can attenuate high spatially varying components of the deformation field, leading to a sub-optimal alignment of local details of the images [24]. Second, high flexibility of the transformation model given by higher complexity of its formulation allows for higher accuracy in the measurements; however, higher complexity leads to lower precision due to spurious variations that need to be controlled by the regularisation constraint on the deformation model [25]. The optimal balance between complexity of the deformation model (that is, accuracy) and the constraints its smoothness (that is, precision) is application-specific, and requires individual investigation given the characteristics of the phenomenon to capture.

How the research questions were addressed and to what extent they have been achieved are now summarised. The most significant findings in each chapter are highlighted, alongside the main contributions.

## Research Question 1

*What is the accuracy of in-vivo MR DVC measurements of biomechanically induced small and large deformation fields?*

Chapters 3 and 5 addressed the suitability of medical image registration methods in capturing, respectively, the small (that is, smaller than the resolution of the images) and large (that is, corresponding features several voxels apart from each other, with large spatial gradients in the displacement field) synthetic deformations applied to *in-vivo* MR scans. Biomechanically plausible deformation fields were generated via finite element simulations, representing deformation of the brain tissue due to gravity and the deformation of the buttock due to sitting. Final accuracy  $\pm$  precision of the DVC measurements in the former scenario was  $0.050 \pm 0.038$  mm against a ground truth with magnitude of  $0.60 \pm 0.26$  mm. For the deformation of the buttock area, performance was investigated first against a simulated field representing partial-weight bearing load with a magnitude of  $7.30 \pm 3.15$  mm, giving an accuracy of  $0.989 \pm 0.943$  mm; secondly, it was tested against a field representing the effect of full-weight load with magnitude of  $19.37 \pm 9.58$  mm, giving an accuracy of  $1.777 \pm 1.854$  mm.

First and foremost, the measurements were affected by the limited resolution of *in-vivo* scans used in the calculations, acquired from MR scans of compliant healthy participants. For both small and large deformations, only wavelengths larger than twice the resolution of the images could be reliably reconstructed, suppressing the distribution of the deformation at strain concentrations, that is, areas of high spatial variations [24]. This is a critical limitation that affect the injury localisation of any risk factor based on such measurements.

Moreover, the study quantified larger margin of error that needs to be accepted when capturing the large deformations of soft tissues relative to other applications of DVC for material science or mechanics of materials [17, 20], in particular when the resolution is limited by *in-vivo* scanning. Only the measurements of positional brain shift (PBS)

satisfied the the recommended accuracy of at least less than  $10^{-1}$  voxel-size reported in Buljac et al. [17].

Optimisation was a critical step for all the experiments on small and large displacements giving different sets of optimal parameters. Better performance in the case of PBS was associated with both smaller spacing of control points of the transformation model and smaller similarity windows. Larger spacing and windows were preferable for the simulation of the buttock deformation due to sitting. These differences are to be related to the magnitude of the displacement fields, as well as the quality of the features represented in the images. For example, higher regularisation was needed in the muscle area of the buttock due to the large deformations that the area underwent, as well as due to the lack of clear features, showing just blurred connective tissue surrounding muscle fascicles and blood vessels. The study showed the importance of optimising these flexible and multi-purpose methods for the specific deformation field to capture via DVC, whose accuracy is of critical importance for any further interpretation of results.

The results from Chapters 3 and 5 addressed **Research question 1** and formed the following two contributions:

**Contribution 1:** *Deformable registration methods for medical imaging showed accuracy which was one order of magnitude smaller than the resolution of the images in following a deformation field characterised by the small displacements representing positional brain shift.*

**Contribution 3:** *Deformable registration methods for medical imaging showed accuracy which was around 10% of the average magnitude of the simulated deformation fields representing the large deformation of the buttock due to sitting.*

## Research Question 2

*Can in-vivo MR DVC measurements characterise the small displacements due to*

*brain shift on a local and global scale, strengthening our understanding of the phenomenon?*

In Chapter 4, the best deformable registration method alongside its optimal parameter set identified in Chapter 3 was used to capture PBS on a population sample of 11 young healthy subjects. For the first time, an average volumetric vector field with the corresponding inter-subject variability was extracted, allowing tissue displacement within surgically relevant ROI to be characterised.

Results showed that even in the healthy brain without any surgical manipulation, the magnitude of PBS can be comparable to the margin of error for the success of stereotactic intervention, with a significant displacement ranging from 0.52 mm to 0.77 mm at surgically relevant structures.

Although likely confounded by MR distortions, strain analysis confirmed both the reported softer response of the brain tissue in tension ( $0.44 \pm 0.64$  % volume preserving and  $0.52 \pm 1.02$  % volume change) and its near incompressibility ( $-0.48 \pm 1.14$  % volume preserving,  $-0.25 \pm 0.76$  % volume change).

Analysis of correlation revealed that in subjects where cranial breadth is larger than 10 mm, the shift was  $20.66^\circ$  more to the left and  $29.17^\circ$  more downwards, with a decrease in magnitude by 0.12 mm (the latter, with weak correlation). On the other hand, head tilt  $10^\circ$  more downwards induced a shift 0.18 mm smaller and  $20.86^\circ$  more downwards.

The chapter gave a measure of the influence of tissue compressibility, intra-cranial geometry and head orientation on PBS: depending on the margin of error allowed for the specific application, these factors need to be addressed when modelling such complex phenomenon. For the case of deep brain stimulation, drug delivery and tissue biopsy, the stringent 1 mm margin of error necessitates patient- and intervention-specific correction of surgical trajectories to integrate into IGNS before further improving the accuracy of other components. The full vector field extracted in the study is of critical

value for the initial validation in simple physiological conditions of any correction to integrate into IGNS, before moving to the more complex deformation induced by surgical manipulation.

These results addressed **Research question 2** and lead to:

**Contribution 2:** *An average volumetric vector field with the corresponding inter-subject variability was extracted in-vivo, allowing tissue displacement within surgically relevant regions of interest to be characterised.*

### **Research Question 3**

*Can in-vivo MR DVC measurements characterise the large displacements of the tissues of the buttock due to sitting on a local and global scale, strengthening our understanding of the phenomenon?*

Chapter 6 showed the measurements of the deformation of the buttock due to semi-recumbent sitting in ten healthy subjects taken from the database by Al-Dirini et al. [1]. The best deformable registration method and its optimal parameter set identified in Chapter 5 were used: the three-dimensional measurements taken extensively depicted the local and global deformation of the subcutaneous tissues, affected by differences in anatomy and posture.

On a global scale, the analysis of deformation permitted to quantify the off-axis slide of the gluteus maximus reported in the literature [13, 189]: the muscle displaced downwards away from both IT and GT of about 11 mm in the second stage of deformation, whereas the fat shifted inferiorly of about 12 mm in both stages of deformation. These results showed the limitations of simplified FE models disregarding off-axis deformation, representing only but a small part of the buttocks, or missing an adequate representation of the soft tissues involved in the deformation.

On a local scale, the spatial evolution of the maximum shear  $\gamma_{max}$  (that has been associated to tissue damage [203]) in a path from the skin to the IT showed a peak of values at the fat-muscle interface and a monotonic decrease towards the IT. Peak value in the first stage of deformation was 1.6-fold the peak in the second stage suggesting that high values of  $\gamma_{max}$  were associated more to the initial redistribution of the tissues under the effect of partial weight than to the effect of the full-body load.

Results from Chapter 6 addressed **Research question 3** and formed:

**Contribution 4:** *For the first time, the three-dimensional displacement field depicting the deformation of the buttock due to sitting in 10 healthy subjects was successfully extracted in-vivo on a local and global scale, giving an extensive depiction of the pattern of deformation.*

## 7.2 Future Work

This section presents some key directions for future development as result of the limitations of the work carried out.

**Optimisation** The optimisation carried out in the study is limited to two applications. This is only but the first step towards quantifying the general accuracy and precision of these methods: a larger variety of deformation fields needs to be tested to assess the overall accuracy of these methods and infer the effect of each parameter on the performance.

In the present work, ground truths were generated via FE simulations, as a cost-effective solution to obtain full-field deformation fields that could be considered biomechanically plausible. The accuracy of such predictions was not investigated and it is to be considered a limitation of the study [120]. The error in their prediction is affected by, among others, geometry of the represented anatomy as well as realistic boundary and loading

conditions [20]. Obtaining distortion-free ground truths that can reliably represent the anisotropic, inhomogeneous and non-linear mechanical response of biological tissues is challenging. Mask and landmark alignment, apart from needing expert drawing from a trained rater, are but a reduced representation of the conformation of tissues, that cannot fully capture the error associated to a dense set of measurements.

With further investigation, better understanding of the accuracy and spatial resolution of strain fields could improve the definition of risk factors to use in a clinical context. Many are the factors influencing such measurements: for instance, strain calculation [66], type of filtering [59], size of the strain window [50], voxel spacing of original images [20] and quality of the features [58]. Independent measures (such as strain gauges on ex-vivo testing), 0-strain measures (repeated scans) or using specimens with known material properties are the most common ways to test accuracy of strain measurements [16]. Among these, 0-strain measures would be ideal in the case of imaging deforming tissues *in-vivo*. However, they cannot represent the complexity of the strain distribution in biological tissues even under simple physiological loads [20, 59]. FE modelling can predict such strain distributions; however, as previously introduced, these systems need prior verification and validation in replicating the complexity of the deformation of most biological tissues [20]. Moreover, high spatial resolution in the strain maps would allow the accurate localisation of areas undergoing deformation above some injury threshold and ultimately predict the location of damage. The feasibility of such calculation in the more challenging *in-vivo* conditions needs further investigation, as the study by Dall'Ara et al. [20] showed that the same strain error ( $200\mu$ ) could be achieved *in-vivo* on an anaesthetised animal model only with a strain window 2.8-times bigger than the same but on *ex-vivo* measurements, due to moving artefacts, lower contrast and lower radiation energy.

Finally, the number of freely available software packages for deformable image registration is very large [40, 71, 72, 76]. Only three of these were compared in this study, but many more could have been analysed (such as NiftyReg [206]). Another important

point of comparison would be testing the performance of conventional deformable registration methods against deep learning-based methods in their use for DVC. Ground truth via FE simulations can be used as training sets for these methods, imposing good properties to the output warp field [45]. Investigation will be needed also to compare the accuracy with the state-of-the-art for DVC measurements in material science or mechanics of material [20].

**Positional Brain Shift** Regarding the influence of brain shift on the success of stereotactic neurosurgery, further understanding of the time evolution of such deformation is needed. Knowing the time it takes for the tissue to stabilise would be critical for the surgeon when re-positioning is needed during a surgical procedure: imaging the distribution of the tissue while it still deforms would give a wrong representation of the actual location of surgical targets. Schnaudigel et al. [5] showed that PBS was still developing even after 24 mins, whereas we identified no tissue deformation after 8 mins during the pilot study. Characterising the time evolution of the deformation is therefore paramount. As briefly mentioned in Section 4.2, fast 2D axial, sagittal and coronal slices were acquired capturing the deformation of the brain tissue in the first 8 mins of deformation. This information, although limited to only four slices, can be coupled with FE modelling [27] to infer the full-field three-dimensional distribution and ultimately confirming the viscoelastic properties of the various regions of the brain.

Future development will also include the analysis of the older population sample investigated, which comparison with the younger sample will inform surgeons on the effect of ageing on PBS. Monea et al. [4] reported that age led to a decrease in displacement amplitude, due to a reduction of brain tissue elasticity and deformability with age, result confirmed with *in-vivo* elastography measurements [207, 208]. Material properties can be investigated from a dense set of displacement with the virtual fields method, informing on the increased stiffness of the brain tissue with age. These methods rely on the use of isostatic displacement fields, where stress distribution can be extracted independently from the material properties, allowing for the identification of material



properties [18]. The method has already been successfully applied to the data on the younger population sample, showing promising directions in the comparison with the older group.

Moreover, diffusion weighted scans were also acquired, in order to investigate the role of white matter tracts on brain shift. The recommended pipeline for diffusion weighted scans in CUBRIC will be followed, implementing the necessary processing such as denoising, gibbs ringing correction, drift correction, etc. The recommended models for tractography, such as spherical deconvolution [209], will be applied in order to then reliably extract the distribution of fibres even in the complex cases of fibre crossing, bending and fanning [210]. The fibre distributions in prone and supine positions will be compared, showing the effect of PBS on white matter tracts.

**Deep Tissue Injury** Regarding the problem of pressure ulcers, as mentioned in Chapter 6, a better acquisition set-up is needed, in order to extract better population statistics by way of a stricter participant recruitment to isolate the individual effects and improve the understanding of such complex deformation. At first, a thorough understanding of the deformation in healthy tissues is paramount, before moving on to pathological cases complicated by impaired mobility or pain sensitivity, as well as scarred or wounded tissue.

A further expansion of the work carried out would consist in the use sitting MR systems such as the Open and Upright MRI Scanner in Wales at the European Scanning Centre. Such a system would allow a simpler acquisition process, giving more repeatable and reliable results [184, 186]. The effect of cushions on the deformation of the buttock is another critical aspect in a clinical setting; the impact of cushioning on the full-field deformation of the tissues in the buttock has not been characterised *in-vivo* yet [169].

Finally, work will be carried out on the design and verification of a finite element model of the human buttock using the results from the study. Material properties will be inversely identified and the performance of the model compared to the state of the art.

The previously mentioned investigation on the spatial resolution and the accuracy of strain field would have here a straightforward application: a reliable way to predict the location of areas of tissues that undergo high strains can be a critical factor in the further development of the prevention of deep tissue injury.

### **7.3 Final Remarks**

The investigation of the accuracy of DVC methods capturing displacement fields from *in-vivo* MR scans has not been explored completely. The richness of the information that can be extracted is invaluable for the further understanding of the complexity of the deformation of soft tissues and the conditions leading to injury.

Verification and validation of both computational models would greatly benefit from the availability of such accurate full-field measurements, in order to predict and simulate the mechanical response of soft tissues.

Designed and developed to tackle inter-subject anatomical differences for MR imaging, deformable registration methods for medical imaging proved to have the flexibility and accuracy to capture the physiological deformation of soft tissues prior to appropriate optimisation. The thesis gave a measure of the error associated to measurements of deformation from such scans.

Future directions of work include first a thorough understanding of the accuracy and spatial resolution of strain measurements, to move to the more challenging cases of tissue deformation in pathological and injurious conditions.

---

## Bibliography

- [1] Rami M.A. Al-Dirini, John Nisyrios, Matthew P. Reed, and Dominic Thewlis. Quantifying the in vivo quasi-static response to loading of sub-dermal tissues in the human buttock using magnetic resonance imaging. *Clinical Biomechanics*, 50(September):70–77, 2017. ISSN 18791271. doi: 10.1016/j.clinbiomech.2017.09.017. URL <https://doi.org/10.1016/j.clinbiomech.2017.09.017>.
- [2] Xiaowei Dong. Current strategies for brain drug delivery. *Theranostics*, 8(6): 1481–1493, 2018. ISSN 18387640. doi: 10.7150/thno.21254.
- [3] Miltiadis Georgiopoulos, John Ellul, Elisabeth Chroni, and Constantine Constantoyannis. Efficacy, Safety, and Duration of a Frameless Fiducial-Less Brain Biopsy versus Frame-based Stereotactic Biopsy: A Prospective Randomized Study. *Journal of Neurological Surgery, Part A: Central European Neurosurgery*, 79(1):31–38, 2018. ISSN 21936323. doi: 10.1055/s-0037-1602697.
- [4] Aida Georgeta Monea, Ignaas Verpoest, Jos Vander Sloten, Georges Van Der Perre, Jan Goffin, and Bart Depreitere. Assessment of relative brain-skull motion in quasistatic circumstances by magnetic resonance imaging. *Journal of Neurotrauma*, 29(13):2305–2317, 2012. ISSN 08977151. doi: 10.1089/neu.2011.2271. URL <http://www.ncbi.nlm.nih.gov/pubmed/22663153>.
- [5] Sonja Schnaudigel, Christoph Preul, Tarik Ugur, Hans Joachim Mentzel, Otto W. Witte, Marc Tittgemeyer, and Georg Hagemann. Positional brain deformation visualized with magnetic resonance morphometry. *Neurosurgery*, 66(2):376–384, 2010. ISSN 0148396X. doi: 10.1227/01.NEU.0000363704.74450.B4.
- [6] Derek L.G. Hill, Calvin R. Maurer, Robert J. Maciunas, John A. Barwise, J. Michael Fitzpatrick, and Matthew Y. Wang. Measurement of intraoperative brain surface deformation under a craniotomy. *Neurosurgery*, 43(3):514–526, 1998. ISSN 0148396X. doi: 10.1097/00006123-199809000-00066.
- [7] Justin K. Rice, Christopher Rorden, Jessica S. Little, and Lucas C. Parra. Subject position affects EEG magnitudes, 2013. ISSN 10538119.
- [8] Yoichi Yokoyama, Yoshitake Yamada, Kenzo Kosugi, Minoru Yamada, Keiichi Narita, Takehiro Nakahara, Hirokazu Fujiwara, Masahiro Toda, and

- Masahiro Jinzaki. Effect of gravity on brain structure as indicated on upright computed tomography. *Scientific Reports*, 11(1):1–9, 2021. ISSN 20452322. doi: 10.1038/s41598-020-79695-z. URL <https://doi.org/10.1038/s41598-020-79695-z>.
- [9] Julian F. Guest, Graham W. Fuller, and Peter Vowden. Cohort study evaluating the burden of wounds to the UK’s National Health Service in 2017/2018: Update from 2012/2013. *BMJ Open*, 10(12):1–15, 2020. ISSN 20446055. doi: 10.1136/bmjopen-2020-045253.
- [10] Eran Linder-Ganz, Noga Shabshin, Yacov Itzchak, and Amit Gefen. Assessment of mechanical conditions in sub-dermal tissues during sitting: A combined experimental-MRI and finite element approach. *Journal of Biomechanics*, 40(7):1443–1454, 2007. ISSN 00219290. doi: 10.1016/j.jbiomech.2006.06.020.
- [11] Mohsen Makhsous, Fang Lin, Andrew Cichowski, Iris Cheng, Charles Fasanati, Thomas Grant, and Ronald W. Hendrix. Use of MRI images to measure tissue thickness over the ischial tuberosity at different hip flexion. *Clinical Anatomy*, 24(5):638–645, 2011. ISSN 08973806. doi: 10.1002/ca.21119.
- [12] Sharon Eve Sonenblum, Stephen H. Sprigle, John Mc Kay Cathcart, and Robert John Winder. 3-dimensional buttocks response to sitting: A case report. *Journal of Tissue Viability*, 22(1):12–18, feb 2013. ISSN 0965206X. doi: 10.1016/j.jtv.2012.11.001.
- [13] Sharon E. Sonenblum, Davin Seol, Stephen H. Sprigle, and John Mc Kay Cathcart. Seated buttocks anatomy and its impact on biomechanical risk. *Journal of Tissue Viability*, 29(2):69–75, 2020. ISSN 18764746. doi: 10.1016/j.jtv.2020.01.004. URL <https://doi.org/10.1016/j.jtv.2020.01.004>.
- [14] Bethany E. Keenan, Sam L. Evans, and Cees W.J. Oomens. A review of foot finite element modelling for pressure ulcer prevention in bedrest: Current perspectives and future recommendations, feb 2022. ISSN 18764746.
- [15] Ferdinand P. Beer, E. Russell Johnston, John T. DeWolf, and David F. Mazurek. *Mechanics of materials*. McGraw-Hill Higher Education, New York ;, 5th ed. edition, 2009. ISBN 9780071284226.
- [16] Marco Palanca, Gianluca Tozzi, and Luca Cristofolini. The use of digital image correlation in the biomechanical area: A review. *International Biomechanics*, 3(1):1–21, 2016. ISSN 23335432. doi: 10.1080/23335432.2015.1117395. URL <http://dx.doi.org/10.1080/23335432.2015.1117395>.
- [17] A. Buljac, C. Jailin, A. Mendoza, J. Neggens, T. Taillandier-Thomas, A. Bouterf, B. Smaniotto, F. Hild, and S. Roux. Digital Volume Correlation: Review of Progress and Challenges. *Experimental Mechanics*, 58(5):661–708, 2018. ISSN 17412765. doi: 10.1007/s11340-018-0390-7.

- [18] Stéphane Avril and Sam Evans. *Material Parameter Identification and Inverse Problems in Soft Tissue Biomechanics*. CISM International Centre for Mechanical Sciences, 2017. ISBN 9783319450711. URL <https://link.springer.com/content/pdf/10.1007/978-3-319-45071-1.pdf><http://link.springer.com/10.1007/978-3-319-45071-1>.
- [19] V. M. Mai. *Hyperpolarized gas and oxygen-enhanced magnetic resonance imaging.*, volume 124. Humana Press, 2006. ISBN 1597450103. doi: 10.1385/1-59745-010-3:323.
- [20] Enrico Dall’Ara, Marta Peña-Fernández, Marco Palanca, Mario Giorgi, Luca Cristofolini, and Gianluca Tozzi. Precision of digital volume correlation approaches for strain analysis in bone imaged with micro-computed tomography at different dimensional levels. *Frontiers in Materials*, 4(November), 2017. ISSN 22968016. doi: 10.3389/fmats.2017.00031.
- [21] Saman Taviana, Jeffrey N. Clark, Nicolas Newell, James D. Calder, and Ulrich Hansen. In vivo deformation and strain measurements in human bone using digital volume correlation (Dvc) and 3t clinical mri. *Materials*, 13(23):1–15, 2020. ISSN 19961944. doi: 10.3390/ma13235354. URL [www.mdpi.com/journal/materials](http://www.mdpi.com/journal/materials).
- [22] Daniel Gallichan, Jos P Marques, and Rolf Gruetter. Retrospective Correction of Involuntary Microscopic Head Movement Using Highly Accelerated Fat Image Navigators (3D FatNavs) at 7T. *Magn Reson Med*, 75:1030–1039, 2016. doi: 10.1002/mrm.25670. URL <http://web>.
- [23] J. Nogueira, A. Lecuona, and P. A. Rodríguez. Local field correction PIV, implemented by means of simple algorithms, and multigrid versions. *Measurement Science and Technology*, 12(11):1911–1921, 2001. ISSN 09570233. doi: 10.1088/0957-0233/12/11/321.
- [24] E. Bar-Kochba, J. Toyjanova, E. Andrews, K.-S S. Kim, C. Franck, · J Toyjanova, · E Andrews, K.-S S. Kim, and · C Franck. A Fast Iterative Digital Volume Correlation Algorithm for Large Deformations. *Experimental Mechanics*, 55(1): 261–274, 2015. ISSN 17412765. doi: 10.1007/s11340-014-9874-2.
- [25] Nico P. van Dijk, Dan Wu, Cecilia Persson, and Per Isaksson. A global digital volume correlation algorithm based on higher-order finite elements: Implementation and evaluation. *International Journal of Solids and Structures*, 168: 211–227, 2019. ISSN 00207683. doi: 10.1016/j.ijsolstr.2019.03.024. URL <https://doi.org/10.1016/j.ijsolstr.2019.03.024>.
- [26] Aristeidis Sotiras, Christos Davatzikos, and Nikos Paragios. Deformable medical image registration: A survey. *IEEE Transactions on Medical Imaging*, 32(7): 1153–1190, 2013. ISSN 02780062. doi: 10.1109/TMI.2013.2265603.

- [27] Nicholas J. Bennion. *Computational modelling of brain shift in stereotactic neurosurgery*. PhD thesis, Cardiff University, 2020. URL <http://orca.cf.ac.uk/id/eprint/133632>.
- [28] Francisco P.M. M Oliveira and Joao Manuel R.S. S Tavares. Medical image registration: a review. *Computer Methods in Biomechanics and Biomedical Engineering*, 17(10):73–93, 2014. ISSN 1476-8259. doi: 10.1080/10255842.2012.670855. URL <http://www.ncbi.nlm.nih.gov/pubmed/22435355><http://dx.doi.org/10.1080/10255842.2012.670855>.
- [29] András P. Keszei, Benjamin Berkels, and Thomas M. Deserno. Survey of Non-Rigid Registration Tools in Medicine. *Journal of Digital Imaging*, 30(1):102–116, 2017. ISSN 1618727X. doi: 10.1007/s10278-016-9915-8. URL <http://dx.doi.org/10.1007/s10278-016-9915-8>.
- [30] Patra Dipti Pradhan Smita, Dipti Patra, Smita Pradhan, Patra Dipti Pradhan Smita, Dipti Patra, Smita Pradhan, Patra Dipti Pradhan Smita, Dipti Patra, and Smita Pradhan. Enhanced Mutual Information Based Medical Image Registration. *IET Image Processing*, 10(5):418–427, 2016. ISSN 1751-9659. doi: 10.1049/iet-ipr.2015.0346. URL <http://digital-library.theiet.org/content/journals/10.1049/iet-ipr.2015.0346>.
- [31] Gary K L Tam, Zhi Quan Cheng, Yu Kun Lai, Frank C. Langbein, Yonghuai Liu, David Marshall, Ralph R. Martin, Xian Fang Sun, and Paul L. Rosin. Registration of 3d point clouds and meshes: A survey from rigid to Nonrigid. *IEEE Transactions on Visualization and Computer Graphics*, 19(7):1199–1217, 2013. ISSN 10772626. doi: 10.1109/TVCG.2012.310.
- [32] Babak A. Ardekani, Stephen Guckemus, Alvin Bachman, Matthew J. Hoptman, Michelle Wojtaszek, and Jay Nierenberg. Quantitative comparison of algorithms for inter-subject registration of 3D volumetric brain MRI scans. *Journal of Neuroscience Methods*, 142(1):67–76, 2005. ISSN 01650270. doi: 10.1016/j.jneumeth.2004.07.014.
- [33] J P W Pluim, J B a Maintz, and M a Viergever. Mutual information based registration of medical images: a survey. *IEEE Transactions on medical imaging*, XX(Y):1–21, 2003. ISSN 0278-0062. doi: 10.1109/TMI.2003.815867.
- [34] P. Markelj, D. Tomaževič, B. Likar, and F. Pernuš. A review of 3D/2D registration methods for image-guided interventions. *Medical Image Analysis*, 16(3):642–661, 2012. ISSN 13618415. doi: 10.1016/j.media.2010.03.005.
- [35] Yangming Ou, Aristeidis Sotiras, Nikos Paragios, and Christos Davatzikos. DRAMMS: Deformable registration via attribute matching and mutual-saliency weighting. *Medical Image Analysis*, 15(4):622–639, 2011. ISSN 13618415. doi: 10.1016/j.media.2010.07.002. URL <http://dx.doi.org/10.1016/j.media.2010.07.002>.

- [36] Mark Holden. A review of geometric transformations for nonrigid body registration. *IEEE Transactions on Medical Imaging*, 27(1):111–128, 2008. ISSN 02780062. doi: 10.1109/TMI.2007.904691.
- [37] Uli Bürgel, Katrin Amunts, Lars Hoemke, Hartmut Mohlberg, Joachim M. Gilsbach, and Karl Zilles. White matter fiber tracts of the human brain: Three-dimensional mapping at microscopic resolution, topography and intersubject variability. *NeuroImage*, 29(4):1092–1105, 2006. ISSN 10538119. doi: 10.1016/j.neuroimage.2005.08.040.
- [38] J P Thirion. Image matching as a diffusion process: an analogy with Maxwell’s demons. *Medical image analysis*, 2(3):243–260, 1998. ISSN 13618415. doi: 10.1016/S1361-8415(98)80022-4.
- [39] Tom Vercauteren, Xavier Pennec, Aymeric Perchant, and Nicholas Ayache. Diffeomorphic demons: efficient non-parametric image registration. *NeuroImage*, 45(1 Suppl):S61–S72, 2009. ISSN 10959572. doi: 10.1016/j.neuroimage.2008.10.040. URL <http://dx.doi.org/10.1016/j.neuroimage.2008.10.040>.
- [40] Yangming Ou, Hamed Akbari, Michel Bilello, Xiao Da, and Christos Davatzikos. Comparative evaluation of registration algorithms in different brain databases with varying difficulty: Results and insights. *IEEE Transactions on Medical Imaging*, 33(10):2039–2065, 2014. ISSN 1558254X. doi: 10.1109/TMI.2014.2330355.
- [41] Julia A. Schnabel, Mattias P. Heinrich, Bartłomiej W. Papież, and Sir J. Michael Brady. Advances and challenges in deformable image registration: From image fusion to complex motion modelling. *Medical Image Analysis*, 33:145–148, 2016. ISSN 13618423. doi: 10.1016/j.media.2016.06.031.
- [42] Nicholas J. Tustison and James C. Gee. Generalized n-D Ck B-spline scattered data approximation with confidence values. In Guang-Zhong Yang, TianZi Jiang, Dinggang Shen, Lixu Gu, and Jie Yang, editors, *Lecture Notes in Computer Science (including subseries Lecture Notes in Artificial Intelligence and Lecture Notes in Bioinformatics)*, volume 4091 LNCS, pages 76–83, Berlin, Heidelberg, 2006. Springer Berlin Heidelberg. ISBN 3540372202. doi: 10.1007/11812715\_10.
- [43] D. Rueckert. Nonrigid registration using free-form deformations: Application to breast mr images. *IEEE Transactions on Medical Imaging*, 18(8):712–721, 1999. ISSN 02780062. doi: 10.1109/42.796284.
- [44] Stefan Klein, Marius Staring, Keelin Murphy, Max A. Viergever, and Josien P.W. Pluim. Elastix: A toolbox for intensity-based medical image registration. *IEEE Transactions on Medical Imaging*, 29(1):196–205, 2010. ISSN 02780062. doi: 10.1109/TMI.2009.2035616.

- [45] Yabo Fu, Yang Lei, Tonghe Wang, Walter J. Curran, Tian Liu, and Xiaofeng Yang. Deep learning in medical image registration: A review. *Physics in Medicine and Biology*, 65(20), 2020. ISSN 13616560. doi: 10.1088/1361-6560/ab843e.
- [46] Haonan Xiao, Xinzhi Teng, Chenyang Liu, Tian Li, Ge Ren, Ruijie Yang, Dinggang Shen, and Jing Cai. A review of deep learning-based three-dimensional medical image registration methods. *Quantitative Imaging in Medicine and Surgery*, 11(12):4895–4916, 2021. ISSN 22234306. doi: 10.21037/qims-21-175.
- [47] M. Faisal Beg, Michael I. Miller, Alain Trouvé, and Laurent Younes. Computing large deformation metric mappings via geodesic flows of diffeomorphisms. *International Journal of Computer Vision*, 61(2):139–157, 2005. ISSN 09205691. doi: 10.1023/B:VISI.0000043755.93987.aa.
- [48] Avants, Brian B., Nicholas J. Tustison, Gang Song, Cook Philip, Arno Klein, and James C. Gee. A Reproducible Evaluation of ANTs Similarity Metric Performance in Brain Image Registration Brian. *Bone*, 23(1):1–7, 2011. ISSN 15378276. doi: 10.1161/CIRCULATIONAHA.110.956839.
- [49] Daniel Rueckert, Paul Aljabar, Rolf A Heckemann, Joseph V Hajnal, and Alexander Hammers. Diffeomorphic registration using B-splines. *Medical image computing and computer-assisted intervention : MICCAI ... International Conference on Medical Image Computing and Computer-Assisted Intervention*, 9(Pt 2):702–9, 2006. ISSN 03029743. doi: 10.1007/11866763. URL <http://www.ncbi.nlm.nih.gov/pubmed/17354834>.
- [50] Bryant C. Roberts, Egon Perilli, and Karen J. Reynolds. Application of the digital volume correlation technique for the measurement of displacement and strain fields in bone: A literature review. *Journal of Biomechanics*, 47(5): 923–934, 2014. ISSN 18732380. doi: 10.1016/j.jbiomech.2014.01.001. URL <http://dx.doi.org/10.1016/j.jbiomech.2014.01.001>.
- [51] M. Liu, J. Guo, C. Y. Hui, and A. T. Zehnder. Application of Digital Image Correlation (DIC) to the Measurement of Strain Concentration of a PVA Dual-Crosslink Hydrogel Under Large Deformation. *Experimental Mechanics*, 59(7): 1021–1032, 2019. ISSN 17412765. doi: 10.1007/s11340-019-00520-4.
- [52] Marta Peña Fernández, Enrico Dall’Ara, Andrew J. Bodey, Rachna Parwani, Asa H. Barber, Gordon W. Blunn, and Gianluca Tozzi. Full-Field Strain Analysis of Bone-Biomaterial Systems Produced by the Implantation of Osteoregenerative Biomaterials in an Ovine Model. *ACS Biomaterials Science and Engineering*, 5 (5):2543–2554, 2019. ISSN 23739878. doi: 10.1021/acsbiomaterials.8b01044.
- [53] Marta Peña Fernández, F Witte, and G Tozzi. Applications of X-ray computed tomography for the evaluation of biomaterial-mediated bone regeneration in critical-sized defects. *Journal of Microscopy*, 277(3):179–196, 2020. ISSN 13652818. doi: 10.1111/jmi.12844.



- [54] Ian J. Gerard, Marta Kersten-Oertel, Kevin Petrecca, Denis Sirhan, Jeffery A. Hall, and D. Louis Collins. Brain shift in neuronavigation of brain tumors: A review, 2017. ISSN 13618423.
- [55] Department of Health. Justification of Computed Tomography (CT) for Individual Health Assessment. *Expert Working Party Report*, (July), 2014. URL [https://www.gov.uk/government/uploads/system/uploads/attachment\\_data/file/326572/IHA\\_-\\_June\\_Report.pdf](https://www.gov.uk/government/uploads/system/uploads/attachment_data/file/326572/IHA_-_June_Report.pdf).
- [56] Hugo Leclerc, Jean Noël Périé, François Hild, and Stéphane Roux. Digital volume correlation: What are the limits to the spatial resolution? *Mechanics and Industry*, 13(6):361–371, 2012. ISSN 22577777. doi: 10.1051/meca/2012025.
- [57] E. Dall’Ara, D. Barber, and M. Viceconti. About the inevitable compromise between spatial resolution and accuracy of strain measurement for bone tissue: A 3D zero-strain study. *Journal of Biomechanics*, 47(12):2956–2963, 2014. ISSN 18732380. doi: 10.1016/j.jbiomech.2014.07.019. URL <http://dx.doi.org/10.1016/j.jbiomech.2014.07.019>.
- [58] Marco Palanca, Andrew J. Bodey, Mario Giorgi, Marco Viceconti, Damien Lacroix, Luca Cristofolini, and Enrico Dall’Ara. Local displacement and strain uncertainties in different bone types by digital volume correlation of synchrotron microtomograms. *Journal of Biomechanics*, 58:27–36, 2017. ISSN 18732380. doi: 10.1016/j.jbiomech.2017.04.007. URL <http://dx.doi.org/10.1016/j.jbiomech.2017.04.007>.
- [59] M. Peña Fernández, A. H. Barber, G. W. Blunn, and G. Tozzi. Optimization of digital volume correlation computation in SR-microCT images of trabecular bone and bone-biomaterial systems. *Journal of Microscopy*, 272(3):213–228, 2018. ISSN 13652818. doi: 10.1111/jmi.12745.
- [60] Gary E. Christensen, Richard D. Rabbitt, and Michael I. Miller. Deformable templates using large deformation kinematics. *IEEE Transactions on Image Processing*, 5(10):1435–1447, 1996. ISSN 10577149. doi: 10.1109/83.536892.
- [61] Zhengzong Tang, Jin Liang, Zhenzhong Xiao, and Cheng Guo. Large deformation measurement scheme for 3D digital image correlation method. *Optics and Lasers in Engineering*, 50(2):122–130, 2012. ISSN 01438166. doi: 10.1016/j.optlaseng.2011.09.018. URL <http://dx.doi.org/10.1016/j.optlaseng.2011.09.018>.
- [62] Caterina Casavola, Lucia Del Core, Vincenzo Moramarco, Giovanni Pappaletta, and Marika Patronelli. Full-field mechanical characterization of polyurethane foams under large deformations by digital image correlation. *Mechanics of Advanced Materials and Structures*, 2021. ISSN 15376532. doi: 10.1080/15376494.2021.1905915. URL <https://www.tandfonline.com/action/journalInformation?journalCode=umcm20>.

- [63] J. Nogueira, A. Lecuona, P. A. Rodríguez, J. A. Alfaro, and A. Acosta. Limits on the resolution of correlation PIV iterative methods. Practical implementation and design of weighting functions. *Experiments in Fluids*, 39(2):314–321, 2005. ISSN 07234864. doi: 10.1007/s00348-005-1017-1.
- [64] Sam Evans. Practical Soft Tissue Mechanics. *Manuscript in preparation*, 2022.
- [65] W. H. Peters and W. F. Ranson. Digital imaging techniques in experimental stress analysis Digital imaging techniques in experimental stress analysis W. *Optical Engineering*, 21(3):427–431, 1982.
- [66] M. G.D. Geers, R. De Borst, and W. A.M. Brekelmans. Computing strain fields from discrete displacement fields in 2d-solids. *International Journal of Solids and Structures*, 1996. ISSN 00207683. doi: 10.1016/0020-7683(95)00240-5.
- [67] P. Lava, S. Cooreman, and D. Debruyne. Study of systematic errors in strain fields obtained via DIC using heterogeneous deformation generated by plastic FEA. *Optics and Lasers in Engineering*, 48(4):457–468, 2010. ISSN 01438166. doi: 10.1016/j.optlaseng.2009.08.013. URL <http://dx.doi.org/10.1016/j.optlaseng.2009.08.013>.
- [68] Ronald W K So and Albert C S Chung. A novel learning-based dissimilarity metric for rigid and non-rigid medical image registration by using Bhattacharyya Distances. *Pattern Recognition*, 62:161–174, 2016. ISSN 00313203. doi: 10.1016/j.patcog.2016.09.004. URL <http://dx.doi.org/10.1016/j.patcog.2016.09.004>.
- [69] Brian B. Avants, Nicholas J. Tustison, and Gang Song. Advanced Normalization Tools (ANTS). *Insight Journal*, pages 1–35, 2009. ISSN 09255273. URL <ftp://ftp3.ie.freesebsd.org/pub/sourceforge/a/project/ad/advants/Documentation/ants.pdf>.
- [70] Catriona D. Good, Ingrid Johnsrude, John Ashburner, Richard N.A. Henson, Karl J. Friston, and Richard S.J. Frackowiak. Cerebral asymmetry and the effects of sex and handedness on brain structure: A voxel-based morphometric analysis of 465 normal adult human brains. *NeuroImage*, 14(3):685–700, sep 2001. ISSN 10538119. doi: 10.1006/nimg.2001.0857. URL <http://www.sciencedirect.com/science/article/pii/S1053811901908572>.
- [71] Keelin Murphy, Bram Van Ginneken, Joseph M. Reinhardt, Sven Kabus, Kai Ding, Xiang Deng, Kunlin Cao, Kaifang Du, Gary E. Christensen, Vincent Garcia, Tom Vercauteren, Nicholas Ayache, Olivier Commowick, Grgoire Malandain, Ben Glocker, Nikos Paragios, Nassir Navab, Vladlena Gorbunova, Jon Sporring, Marleen De Bruijne, Xiao Han, Mattias P. Heinrich, Julia A. Schnabel, Mark Jenkinson, Cristian Lorenz, Marc Modat, Jamie R. McClelland, Sebastien Ourselin, Sascha E.A. Muenzing, Max A. Viergever, Dante De Nigris, D. Louis Collins,

- Tal Arbel, Marta Peroni, Rui Li, Gregory C. Sharp, Alexander Schmidt-Richberg, Jan Ehrhardt, René Werner, Dirk Smeets, Dirk Loeckx, Gang Song, Nicholas Tustison, Brian Avants, James C. Gee, Marius Staring, Stefan Klein, Berend C. Stoel, Martin Urschler, Manuel Werlberger, Jef Vandemeulebroucke, Simon Rit, David Sarrut, and Josien P.W. Pluim. Evaluation of registration methods on thoracic CT: The EMPIRE10 challenge. *IEEE Transactions on Medical Imaging*, 30(11):1901–1920, 2011. ISSN 02780062. doi: 10.1109/TMI.2011.2158349.
- [72] Zhoubing Xu, Christopher P. Lee, Mattias P. Heinrich, Marc Modat, Daniel Rueckert, Sebastien Ourselin, Richard G. Abramson, and Bennett A. Landman. Evaluation of six registration methods for the human abdomen on clinically acquired CT. *IEEE Transactions on Biomedical Engineering*, 63(8):1563–1572, 2016. ISSN 15582531. doi: 10.1109/TBME.2016.2574816.
- [73] Yabo Fu, Yang Lei, Tonghe Wang, Kristin Higgins, Jeffrey D. Bradley, Walter J. Curran, Tian Liu, and Xiaofeng Yang. LungRegNet: An unsupervised deformable image registration method for 4D-CT lung. *Medical Physics*, 47(4):1763–1774, apr 2020. ISSN 00942405. doi: 10.1002/mp.14065.
- [74] Zhuoran Jiang, Fang Fang Yin, Yun Ge, and Lei Ren. A multi-scale framework with unsupervised joint training of convolutional neural networks for pulmonary deformable image registration. *Physics in Medicine and Biology*, 65(1), jan 2020. ISSN 13616560. doi: 10.1088/1361-6560/ab5da0.
- [75] Minh Q Tran, Tuong Do, Huy Tran, Erman Tjiputra, Quang D Tran, and Anh Nguyen. Light-weight Deformable Registration using Adversarial Learning with Distilling Knowledge. *IEEE TRANSACTIONS ON MEDICAL IMAGING*, XX: 1–10, 2020. URL <https://github.com/aioz-ai/LDR>.
- [76] Arno Klein, Jesper Andersson, Babak A. Ardekani, John Ashburner, Brian Avants, Ming Chang Chiang, Gary E. Christensen, D. Louis Collins, James Gee, Pierre Hellier, Joo Hyun Song, Mark Jenkinson, Claude Lepage, Daniel Rueckert, Paul Thompson, Tom Vercauteren, Roger P. Woods, J. John Mann, and Ramin V. Parsey. Evaluation of 14 nonlinear deformation algorithms applied to human brain MRI registration. *NeuroImage*, 46(3):786–802, 2009. ISSN 10538119. doi: 10.1016/j.neuroimage.2008.12.037. URL <http://dx.doi.org/10.1016/j.neuroimage.2008.12.037>.
- [77] Mark Jenkinson and Stephen Smith. A global optimisation method for robust affine registration of brain images. *Medical Image Analysis*, 5(2):143–156, jun 2001. ISSN 1361-8415. doi: 10.1016/S1361-8415(01)00036-6.
- [78] Mark Jenkinson, Peter Bannister, Michael Brady, and Stephen Smith. Improved Optimization for the Robust and Accurate Linear Registration and Motion Correction of Brain Images. *NeuroImage*, 17(2):825–841, 2002. ISSN 10538119. doi: 10.1006/nimg.2002.1132.

- [79] B. B. Avants, C. L. Epstein, M. Grossman, and J. C. Gee. Symmetric diffeomorphic image registration with cross-correlation: Evaluating automated labeling of elderly and neurodegenerative brain. *Medical Image Analysis*, 12(1):26–41, 2008. ISSN 13618415. doi: 10.1016/j.media.2007.06.004.
- [80] Nicholas J. Tustison and Brian B. Avants. Explicit B-spline regularization in diffeomorphic image registration. *Frontiers in Neuroinformatics*, 7(DEC):1–13, 2013. ISSN 16625196. doi: 10.3389/fninf.2013.00039.
- [81] Yongchoel Choi and Seungyong Lee. Injectivity conditions of 2D and 3D uniform cubic B-spline functions. *Graphical Models*, 62(6):411–427, 2000. ISSN 15240703. doi: 10.1006/gmod.2000.0531.
- [82] Emanuele Borgonovo and Elmar Plischke. Sensitivity analysis: A review of recent advances. *European Journal of Operational Research*, 248(3):869–887, 2016. ISSN 03772217. doi: 10.1016/j.ejor.2015.06.032. URL <http://dx.doi.org/10.1016/j.ejor.2015.06.032>.
- [83] Andrea Saltelli, Paola Annoni, Ivano Azzini, Francesca Campolongo, Marco Ratto, and Stefano Tarantola. Variance based sensitivity analysis of model output. Design and estimator for the total sensitivity index. *Computer Physics Communications*, 181(2):259–270, 2010. ISSN 00104655. doi: 10.1016/j.cpc.2009.09.018. URL <http://dx.doi.org/10.1016/j.cpc.2009.09.018>.
- [84] Francesca Campolongo, Jessica Cariboni, and Andrea Saltelli. An effective screening design for sensitivity analysis of large models. *Environmental Modelling and Software*, 22(10):1509–1518, 2007. ISSN 13648152. doi: 10.1016/j.envsoft.2006.10.004.
- [85] Jeremy E. Oakley and Anthony O’Hagan. Probabilistic sensitivity analysis of complex models: A Bayesian approach. *Journal of the Royal Statistical Society. Series B: Statistical Methodology*, 66(3):751–769, 2004. ISSN 13697412. doi: 10.1111/j.1467-9868.2004.05304.x.
- [86] Jan Oliver Neumann, Henrik Giese, Armin Biller, Armin M. Nagel, and Karl Kiening. Spatial Distortion in MRI-Guided Stereotactic Procedures: Evaluation in 1.5-, 3- and 7-Tesla MRI Scanners. *Stereotactic and Functional Neurosurgery*, 93(6):380–386, 2015. ISSN 14230372. doi: 10.1159/000441233.
- [87] Yoichi Watanabe, Chung K. Lee, and Bruce J. Gerbi. Geometrical accuracy of a 3-tesla magnetic resonance imaging unit in Gamma Knife surgery. *Journal of neurosurgery*, 105(Supplement):190–193, 2006. ISSN 00223085. doi: 10.3171/sup.2006.105.7.190.
- [88] Christian P. Karger, Angelika Höss, Rolf Bendl, Valer Canda, and Lothar Schad. Accuracy of device-specific 2D and 3D image distortion correction algorithms for magnetic resonance imaging of the head provided by a manufacturer. *Physics*

- in Medicine and Biology*, 51(12):N253–61, 2006. ISSN 00319155. doi: 10.1088/0031-9155/51/12/N04.
- [89] Philipp Dammann, Oliver Kraff, Karsten H. Wrede, Neriman Özkan, Stephan Orzada, Oliver M. Mueller, I. Erol Sandalcioglu, Ulrich Sure, Elke R. Gizewski, Mark E. Ladd, and Thomas Gasser. Evaluation of Hardware-related Geometrical Distortion in Structural MRI at 7 Tesla for Image-guided Applications in Neurosurgery. *Academic Radiology*, 18(7):910–916, 2011. ISSN 10766332. doi: 10.1016/j.acra.2011.02.011.
- [90] Yuval Duchin, Aviva Abosch, Essa Yacoub, Guillermo Sapiro, and Noam Harel. Feasibility of using ultra-high field (7 T) MRI for clinical surgical targeting. *PLoS ONE*, 7(5):1–10, 2012. ISSN 19326203. doi: 10.1371/journal.pone.0037328. URL <https://doi.org/10.1371/journal.pone.0037328>.
- [91] Thilaka S. Sumanaweera, John R. Adler, Gary H. Glover, Paul F. Hemler, Petra A. van den Elsen, David Martin, and Sandy Napel. Method for correcting magnetic resonance image distortion for frame-based stereotactic surgery, with preliminary results. *Computer Aided Surgery*, 1(3):151–157, 1995. ISSN 10929088. doi: 10.3109/10929089509105689.
- [92] Jonathan C. Lau, Ali R. Khan, Tony Y. Zeng, Keith W. MacDougall, Andrew G. Parrent, and Terry M. Peters. Quantification of local geometric distortion in structural magnetic resonance images: Application to ultra-high fields. *NeuroImage*, 168(July 2016):141–151, 2018. ISSN 10959572. doi: 10.1016/j.neuroimage.2016.12.066.
- [93] Jeffrey Mark Treiber, Nathan S. White, Tyler Christian Steed, Hauke Bartsch, Dominic Holland, Nikdokht Farid, Carrie R. McDonald, Bob S. Carter, Anders Martin Dale, and Clark C. Chen. Characterization and correction of geometric distortions in 814 Diffusion Weighted Images. *PLoS ONE*, 11(3):1–9, 2016. ISSN 19326203. doi: 10.1371/journal.pone.0152472.
- [94] W. Jeffrey Elias, Kai-Ming Fu, and Robert C. Frysinger. Cortical and subcortical brain shift during stereotactic procedures. *Journal of Neurosurgery*, 107(5): 983–988, 2007. ISSN 1933-0693. doi: 10.3171/jns.2007.107.5.983.
- [95] Vitor Mendes Pereira, Iris Smit-Ockeloen, Olivier Brina, Drazenko Babic, Marcel Breeuwer, Karl Schaller, Karl Olof Lovblad, and Daniel Ruijters. Volumetric measurements of brain shift using intraoperative cone-beam computed tomography: Preliminary study. *Operative Neurosurgery*, 12(4):4–12, 2016. ISSN 23324252. doi: 10.1227/NEU.0000000000000999.
- [96] Caio M. Matias, Leonardo A. Frizon, Fadi Asfahan, Juan D. Uribe, and Andre G. Machado. Brain shift and pneumocephalus assessment during frame-based deep brain stimulation implantation with intraoperative magnetic resonance imaging.

- Operative Neurosurgery*, 14(6):668–674, 2018. ISSN 23324260. doi: 10.1093/ons/opx170. URL <https://academic.oup.com/ons/article-lookup/doi/10.1093/ons/opx170>.
- [97] M. H.T. Reinges, H. H. Nguyen, T. Krings, B. O. Hütter, V. Rohde, J. M. Gilsbach, Peter Mc L. Black, K. Takakura, and David W. Roberts. Course of brain shift during microsurgical resection of supratentorial cerebral lesions: Limits of conventional neuronavigation. *Acta Neurochirurgica*, 146(4):369–377, 2004. ISSN 00016268. doi: 10.1007/s00701-003-0204-1.
- [98] Zhe Li, Jian Guo Zhang, Yan Ye, and Xiaoping Li. Review on Factors Affecting Targeting Accuracy of Deep Brain Stimulation Electrode Implantation between 2001 and 2015. *Stereotactic and Functional Neurosurgery*, 94(6):351–362, 2017. ISSN 14230372. doi: 10.1159/000449206.
- [99] Alastair J. Martin, Paul S. Larson, Jill L. Ostrem, W. Keith Sootsman, Pekka Talke, Oliver M. Weber, Nadja Levesque, Jeffrey Myers, and Philip A. Starr. Placement of deep brain stimulator electrodes using real-time high-field interventional magnetic resonance imaging. *Magnetic Resonance in Medicine*, 54(5):1107–1114, 2005. ISSN 07403194. doi: 10.1002/mrm.20675.
- [100] Philip A. Starr, Alastair J. Martin, Jill L. Ostrem, Pekka Talke, Nadja Levesque, and Paul S. Larson. Subthalamic nucleus deep brain stimulator placement using high-field interventional magnetic resonance imaging and a skull-mounted aiming device: Technique and application accuracy - Clinical article. *Journal of Neurosurgery*, 112(3):479–490, 2010. ISSN 00223085. doi: 10.3171/2009.6.JNS081161.
- [101] Daniel Von Langsdorff, Philippe Paquis, and Denys Fontaine. In vivo measurement of the frame-based application accuracy of the Neuromate neurosurgical robot. *Journal of Neurosurgery*, 122(1):191–194, 2015. ISSN 19330693. doi: 10.3171/2014.9.JNS14256. URL <http://www.ncbi.nlm.nih.gov/pubmed/25361490>.
- [102] Hani J. Marcus, Vejay N. Vakharia, Sebastien Ourselin, John Duncan, Martin Tisdall, and Kristian Aquilina. Robot-assisted stereotactic brain biopsy: Systematic review and bibliometric analysis. *Child's Nervous System*, 34(7):1299–1309, 2018. ISSN 14330350. doi: 10.1007/s00381-018-3821-y.
- [103] Francesco Cardinale, Michele Rizzi, Piergiorgio D’Orto, Giuseppe Casaceli, Gabriele Arnulfo, Massimo Narizzano, Davide Scorza, Elena De Momi, Michele Nichelatti, Daniela Redaelli, Maurizio Sberna, Alessio Moscato, and Laura Castana. A new tool for touch-free patient registration for robot-assisted intracranial surgery: Application accuracy from a phantom study and a retrospective surgical series. *Neurosurgical Focus*, 42(5):E8, 2017. ISSN 10920684. doi: 10.3171/2017.2.FOCUS16539.

- [104] T. Hartkens, D. L.G. Hill, A. D. Castellano-Smith, D. J. Hawkes, C. R. Maurer, A. J. Martin, W. A. Hall, H. Liu, and C. L. Truwit. Measurement and analysis of brain deformation during neurosurgery. *IEEE Transactions on Medical Imaging*, 22(1):82–92, 2003. ISSN 02780062. doi: 10.1109/TMI.2002.806596.
- [105] Ruben Geevarghese, Ruth Ogorman Tuura, Daniel E. Lumsden, Michael Samuel, and Keyoumars Ashkan. Registration Accuracy of CT/MRI Fusion for Localisation of Deep Brain Stimulation Electrode Position: An Imaging Study and Systematic Review. *Stereotactic and Functional Neurosurgery*, 94(3):159–163, 2016. ISSN 14230372. doi: 10.1159/000446609.
- [106] Tanmoy K. Maiti, Subhas Konar, Shyamal Bir, Piyush Kalakoti, and Anil Nanda. Intra-operative micro-electrode recording in functional neurosurgery: Past, present, future. *Journal of Clinical Neuroscience*, 32(October 2016): 166–172, 2016. ISSN 15322653. doi: 10.1016/j.jocn.2016.03.028. URL <http://dx.doi.org/10.1016/j.jocn.2016.03.028>.
- [107] Casey H. Halpern, Shabbar F. Danish, Gordon H. Baltuch, and Jurg L. Jaggi. Brain shift during deep brain stimulation surgery for Parkinson’s disease. *Stereotactic and Functional Neurosurgery*, 86(1):37–43, 2007. ISSN 10116125. doi: 10.1159/000108587.
- [108] Alim Louis Benabid. Deep brain stimulation of the subthalamic nucleus for the treatment of Parkinson’s disease. *Current Opinion in Neurobiology*, 13(6): 696–706, 2003. ISSN 09594388. doi: 10.1016/j.conb.2003.11.001.
- [109] Michael I. Miga, Kay Sun, Ishita Chen, Logan W. Clements, Thomas S. Pfeiffer, Amber L. Simpson, and Reid C. Thompson. Clinical evaluation of a model-updated image-guidance approach to brain shift compensation: experience in 16 cases. *International Journal of Computer Assisted Radiology and Surgery*, 11(8): 1467–1474, 2016. ISSN 18616429. doi: 10.1007/s11548-015-1295-x.
- [110] Yasushi Miyagi, Fumio Shima, and Tomio Sasaki. Brain shift: an error factor during implantation of deep brain stimulation electrodes. *Journal of neurosurgery*, 107(5):989–97, 2007. ISSN 0022-3085. doi: 10.3171/JNS-07/11/0989. URL <http://www.ncbi.nlm.nih.gov/pubmed/17977272>.
- [111] Prashanth Dumpuri, Reid C. Thompson, Benoit M. Dawant, A. Cao, and Michael I. Miga. An atlas-based method to compensate for brain shift: Preliminary results. *Medical Image Analysis*, 11(2):128–145, 2007. ISSN 13618415. doi: 10.1016/j.media.2006.11.002.
- [112] Grand Roman Joldes, Adam Wittek, Mathieu Couton, Simon K. Warfield, and Karol Miller. Real-time prediction of brain shift using nonlinear finite element algorithms. In *Lecture Notes in Computer Science (including subseries Lecture Notes in Artificial Intelligence and Lecture Notes in Bioinformatics)*, volume 5762 LNCS, pages 300–307, 2009. ISBN 3642042708. doi:

- 10.1007/978-3-642-04271-3\_37. URL <http://link.springer.com/10.1007/978-3-642-04271-3>.
- [113] Kay Sun, Thomas S. Pheiffer, Amber L. Simpson, Jared A. Weis, Reid C. Thompson, and Michael I. Miga. Near Real-Time Computer Assisted Surgery for Brain Shift Correction Using Biomechanical Models. *IEEE Journal of Translational Engineering in Health and Medicine*, 2(March):1–13, 2014. ISSN 21682372. doi: 10.1109/JTEHM.2014.2327628.
- [114] Amrollah Mohammadi, Alireza Ahmadian, Shahram Rabbani, Ehsan Fattahi, and Shapour Shirani. A combined registration and finite element analysis method for fast estimation of intraoperative brain shift; phantom and animal model study. *International Journal of Medical Robotics and Computer Assisted Surgery*, 13(4): 1–8, 2017. ISSN 1478596X. doi: 10.1002/rcs.1792. URL <http://doi.wiley.com/10.1002/rcs.1792>.
- [115] Revanth Reddy Garlapati, Aditi Roy, Grand Roman Joldes, Adam Wittek, Ahmed Mostayed, Barry Doyle, Simon Keith Warfield, Ron Kikinis, Neville Knuckey, Stuart Bunt, and Karol Miller. Biomechanical modeling provides more accurate data for neuronavigation than rigid registration. *Journal of Neurosurgery*, 120(6): 1477–1483, 2014. ISSN 0022-3085. doi: 10.3171/2013.12.JNS131165. URL <http://thejns.org/doi/10.3171/2013.12.JNS131165>.
- [116] Christopher Nimsky, Oliver Ganslandt, Simon Cerny, Peter Hastreiter, Rudolf Fahlbusch, Günther Greiner, and Rudolf Fahlbusch. Quantification of, visualization of, and compensation for brain shift using intraoperative magnetic resonance imaging. *Neurosurgery*, 47(5):1070–1080, 2000. ISSN 0148396X. doi: 10.1097/00006123-200011000-00008. URL <http://www.ncbi.nlm.nih.gov/pubmed/11063099><https://academic.oup.com/neurosurgery/article/47/5/1070/2754911>.
- [117] Matthew F. Glasser, Stamatios N. Sotiropoulos, J. Anthony Wilson, Timothy S. Coalson, Bruce Fischl, Jesper L. Andersson, Junqian Xu, Saad Jbabdi, Matthew Webster, Jonathan R. Polimeni, David C. Van Essen, and Mark Jenkinson. The minimal preprocessing pipelines for the Human Connectome Project. *NeuroImage*, 80:105–124, 2013. ISSN 10538119. doi: 10.1016/j.neuroimage.2013.04.127. URL <http://dx.doi.org/10.1016/j.neuroimage.2013.04.127>.
- [118] Jorge Jovicich, Silvester Czanner, Douglas Greve, Elizabeth Haley, Andre Van Der Kouwe, Randy Gollub, David Kennedy, Franz Schmitt, Gregory Brown, James MacFall, Bruce Fischl, and Anders Dale. Reliability in multi-site structural MRI studies: Effects of gradient non-linearity correction on phantom and human data. *NeuroImage*, 30(2):436–443, 2006. ISSN 10538119. doi: 10.1016/j.neuroimage.2005.09.046.



- [119] Wagner Malagó Tavares, Francisco Tustumi, Claudia Da Costa Leite, Lionel Fernel Gamarra, Edson Amaro, Manoel Jacobsen Teixeira, and Erich Talamoni Fonoff. An image correction protocol to reduce distortion for 3-T stereotactic MRI. *Neurosurgery*, 74(1):121–126, 2014. ISSN 0148396X. doi: 10.1227/NEU.0000000000000178.
- [120] Julia A. Schnabel, Christine Tanner, Andy D. Castellano-Smith, Andreas Degenhard, Martin O. Leach, D. Rodney Hose, Derek L.G. Hill, and David J. Hawkes. Validation of nonrigid image registration using finite-element methods: Application to breast MR images. *IEEE Transactions on Medical Imaging*, 22(2):238–247, 2003. ISSN 02780062. doi: 10.1109/TMI.2002.808367.
- [121] Lee R. Dice. Measures of the Amount of Ecologic Association Between Species. *Ecology*, 26(3):297–302, 1945. ISSN 0012-9658. doi: 10.2307/1932409.
- [122] Stephen M. Smith. Fast robust automated brain extraction. *Human Brain Mapping*, 17(3):143–155, 2002. ISSN 10659471. doi: 10.1002/hbm.10062.
- [123] Torsten Rohlfing. Image similarity and tissue overlaps as surrogates for image registration accuracy: Widely used but unreliable. *IEEE Transactions on Medical Imaging*, 31(2):153–163, 2012. ISSN 02780062. doi: 10.1109/TMI.2011.2163944.
- [124] Zachary Danziger. Hausdorff Distance, 2021. URL <https://www.mathworks.com/matlabcentral/fileexchange/26738-hausdorff-distance>.
- [125] Martin Visser, Jan Petr, Dominique M J Müller, Roelant S Eijgelaar, Eef J Hendriks, Marnix Witte, Frederik Barkhof, Marcel van Herk, Henk J M M Mutsaerts, Hugo Vrenken, Jan C de Munck, and Philip C De Witt Hamer. Accurate MR Image Registration to Anatomical Reference Space for Diffuse Glioma, 2020. URL <https://www.frontiersin.org/article/10.3389/fnins.2020.00585>.
- [126] Stefano Zappalá, Nicholas J. Bennion, Matthew R. Potts, Jing Wu, Slawomir Kusmia, Derek K. Jones, Sam L. Evans, and David Marshall. Full-field MRI measurements of in-vivo positional brain shift reveal the significance of intracranial geometry and head orientation for stereotactic surgery. *Scientific Reports*, 11(1):17684, dec 2021. doi: 10.1038/S41598-021-97150-5. URL <https://www.nature.com/articles/s41598-021-97150-5>.
- [127] Günther Grabner, Andrew L. Janke, Marc M. Budge, David Smith, Jens Pruessner, and D. Louis Collins. Symmetric atlasing and model based segmentation: An application to the hippocampus in older adults. *Lecture Notes in Computer Science (including subseries Lecture Notes in Artificial Intelligence and Lecture Notes in Bioinformatics)*, LNCS(4191):58–66, 2006. ISSN 16113349. doi: 10.1007/11866763\_8.

- [128] G R Liu. *The finite element method : a practical course*. Elsevier, Amsterdam, second edi edition. ISBN 0-08-099441-5.
- [129] Adam Wittek and Karol Miller. *Computational biomechanics for medical image analysis*. Elsevier Inc., 2019. ISBN 9780128161760. doi: 10.1016/B978-0-12-816176-0.00044-2. URL <https://doi.org/10.1016/B978-0-12-816176-0.00044-2>.
- [130] D. C. Alexander, C. Pierpaoli, P. J. Basser, and J. C. Gee. Spatial transformations of diffusion tensor magnetic resonance images. *IEEE Transactions on Medical Imaging*, 20(11):1131–1139, 2001. ISSN 02780062. doi: 10.1109/42.963816. URL <http://www.ncbi.nlm.nih.gov/pubmed/11700739><http://ieeexplore.ieee.org.www2.lib.ku.edu:2048/ielx5/42/20807/00963816.pdf?tp=&arnumber=963816&isnumber=20807><http://www.ncbi.nlm.nih.gov/pubmed/11700739>.
- [131] Ali Gholipour, Judy A. Estroff, and Simon K. Warfield. Robust super-resolution volume reconstruction from slice acquisitions: Application to fetal brain MRI. *IEEE Transactions on Medical Imaging*, 29(10):1739–1758, 2010. ISSN 02780062. doi: 10.1109/TMI.2010.2051680.
- [132] Marc C. Kennedy, Anthony O’Hagan, and Neil Higgins. Bayesian Analysis of Computer Code Outputs. *Quantitative Methods for Current Environmental Issues*, pages 227–243, 2002. doi: 10.1007/978-1-4471-0657-9\_11.
- [133] Josien P.W. Pluim, Sascha E.A. Muenzing, Koen A.J. Eppenhof, and Keelin Murphy. The truth is hard to make: Validation of medical image registration. In *Proceedings - International Conference on Pattern Recognition*, volume 0, pages 2294–2300, 2016. ISBN 9781509048472. doi: 10.1109/ICPR.2016.7899978.
- [134] Hubert W. Schreier. Systematic errors in digital image correlation caused by intensity interpolation. *Optical Engineering*, 39(11):2915, 2000. ISSN 0091-3286. doi: 10.1117/1.1314593.
- [135] M.R. Potts. A Phantom for the Study of Positional Brain Shift. 2021.
- [136] Arash A. Sabet, Eftychios Christoforou, Benjamin Zatlin, Guy M. Genin, and Philip V. Bayly. Deformation of the human brain induced by mild angular head acceleration. *Journal of Biomechanics*, 41(2):307–315, 2008. ISSN 00219290. doi: 10.1016/j.jbiomech.2007.09.016.
- [137] Y. Feng, T. M. Abney, R. J. Okamoto, R. B. Pless, G. M. Genin, and P. V. Bayly. Relative brain displacement and deformation during constrained mild frontal head impact. *Journal of the Royal Society Interface*, 7(53):1677–1688, 2010. ISSN 17425662. doi: 10.1098/rsif.2010.0210. URL <http://rsif.royalsocietypublishing.org/content/7/53/1677>.

- [138] Songbai Ji, Qiliang Zhu, Lawrence Dougherty, and Susan S. Margulies. In Vivo Measurements of Human Brain Displacement. *SAE Technical Papers*, 48 (November):527–539, 2004. ISSN 01487191. doi: 10.4271/2004-22-0010.
- [139] Catriona D Good, Ingrid S Johnsrude, John Ashburner, Richard N.A. Henson, Karl J Friston, and Richard S.J. Frackowiak. A voxel-based morphometric study of ageing in 465 normal adult human brains. *NeuroImage*, 14(1 I):21–36, 2001. ISSN 10538119. doi: 10.1006/nimg.2001.0786.
- [140] Anastasia Yendiki, Patricia Panneck, Priti Srinivasan, Allison Stevens, Lilla Zöllei, Jean Augustinack, Ruopeng Wang, David Salat, Stefan Ehrlich, Tim Behrens, Saad Jbabdi, Randy Gollub, and Bruce Fischl. Automated probabilistic reconstruction of white-matter pathways in health and disease using an atlas of the underlying anatomy. *Frontiers in Neuroinformatics*, 5(October):1–12, 2011. ISSN 16625196. doi: 10.3389/fninf.2011.00023. URL <http://journal.frontiersin.org/article/10.3389/fninf.2011.00023/abstract><http://www.pubmedcentral.nih.gov/articlerender.fcgi?artid=3193073&tool=pmcentrez&rendertype=abstract>.
- [141] J Xu, S Kobayashi, S Yamaguchi, K Iijima, K Okada, and K Yamashita. Gender effects on age-related changes in brain structure. *AJNR. American journal of neuroradiology*, 21(1):112–8, 2000. ISSN 0195-6108. URL <http://www.ajnr.org/content/21/1/112.abstract>.
- [142] John P. Mugler and James R. Brookeman. Rapid three-dimensional T1-weighted MR imaging with the MP-RAGE sequence. *Journal of Magnetic Resonance Imaging*, 1(5):561–567, 1991. ISSN 15222586. doi: 10.1002/jmri.1880010509. URL <https://onlinelibrary.wiley.com/doi/pdf/10.1002/jmri.1880010509>.
- [143] Amanda Bischoff-Grethe, I. Burak Ozyurt, Evelina Busa, Brian T. Quinn, Christine Fennema-Notestine, Camellia P. Clark, Shaunna Morris, Mark W. Bondi, Terry L. Jernigan, Anders M. Dale, Gregory G. Brown, and Bruce Fischl. A technique for the deidentification of structural brain MR images. *Human Brain Mapping*, 28(9):892–903, 2007. ISSN 10659471. doi: 10.1002/hbm.20312. URL <http://www.hhs.gov/ocr/hipaa/>.
- [144] John Ashburner and Karl J. Friston. Unified segmentation. *NeuroImage*, 26(3): 839–851, 2005. ISSN 10538119. doi: 10.1016/j.neuroimage.2005.02.018.
- [145] Marco Ganzetti, Nicole Wenderoth, and Dante Mantini. Quantitative Evaluation of Intensity Inhomogeneity Correction Methods for Structural MR Brain Images. *Neuroinformatics*, 14(1):5–21, 2016. ISSN 15392791. doi: 10.1007/s12021-015-9277-2.
- [146] C. Spearman. The proof and measurement of association between two things. By C. Spearman, 1904. *The American journal of psychology*, 100(3-4):441–471,

1987. ISSN 00029556. doi: 10.2307/1422689. URL <http://www.jstor.org/stable/1422689>.
- [147] Rahul S. Desikan, Florent Ségonne, Bruce Fischl, Brian T. Quinn, Bradford C. Dickerson, Deborah Blacker, Randy L. Buckner, Anders M. Dale, R. Paul Maguire, Bradley T. Hyman, Marilyn S. Albert, and Ronald J. Killiany. An automated labeling system for subdividing the human cerebral cortex on MRI scans into gyral based regions of interest. *NeuroImage*, 31(3):968–980, 2006. ISSN 10538119. doi: 10.1016/j.neuroimage.2006.01.021.
- [148] Max C. Keuken and Birte U. Forstmann. A probabilistic atlas of the basal ganglia using 7 T MRI. *Data in Brief*, 4(September 2015):577–582, 2015. ISSN 23523409. doi: 10.1016/j.dib.2015.07.028. URL <http://dx.doi.org/10.1016/j.dib.2015.07.028>.
- [149] J. Mazziotta, A. Toga, A. Evans, P. Fox, J. Lancaster, K. Zilles, R. Woods, T. Paus, G. Simpson, B. Pike, C. Holmes, L. Collins, P. Thompson, D. MacDonald, M. Iacoboni, T. Schormann, K. Amunts, N. Palomero-Gallagher, S. Geyer, L. Parsons, K. Narr, N. Kabani, G. Le Goualher, D. Boomsma, T. Cannon, R. Kawashima, and B. Mazoyer. A probabilistic atlas and reference system for the human brain: International Consortium for Brain Mapping (ICBM). *Philosophical Transactions of the Royal Society B: Biological Sciences*, 356(1412):1293–1322, 2001. ISSN 09628436. doi: 10.1098/rstb.2001.0915.
- [150] Constance Hammond, Rachida Ammari, Bernard Bioulac, and Liliana Garcia. Latest view on the mechanism of action of deep brain stimulation. *Movement Disorders*, 23(15):2111–2121, 2008. ISSN 08853185. doi: 10.1002/mds.22120.
- [151] Morten L. Kringelbach, Ned Jenkinson, Sarah L.F. Owen, and Tipu Z. Aziz. Translational principles of deep brain stimulation. *Nature Reviews Neuroscience*, 8(8):623–635, 2007. ISSN 1471003X. doi: 10.1038/nrn2196.
- [152] E. Garbayo, E. Ansorena, and M.J. Blanco-Prieto. Brain Drug Delivery Systems for Neurodegenerative Disorders. *Current Pharmaceutical Biotechnology*, 13(12):2388–2402, 2012. ISSN 13892010. doi: 10.2174/138920112803341761.
- [153] Gerhard Holzapfel. *Nonlinear Solid Mechanics: A Continuum Approach for Engineering Science*, 2002. ISSN 0025-6455. URL <http://scholar.google.com/scholar?hl=en&btnG=Search&q=intitle:Nonlinear+Solid+Mechanics#6%5Cnhttp://scholar.google.com/scholar?hl=en&btnG=Search&q=intitle:Nonlinear+solid+mechanics%236%5Cnhttp://www.citeulike.org/group/2006/article/1044720%5Cnhttp://www.cit>.
- [154] Michael E. Ivan, Jay Yarlagadda, Akriti P. Saxena, Alastair J. Martin, Philip A. Starr, W. Keith Sootsman, and Paul S. Larson. Brain shift during bur hole-based procedures using interventional MRI: Clinical article. *Journal of*

- Neurosurgery*, 121(1):149–160, 2014. ISSN 19330693. doi: 10.3171/2014.3.JNS121312. URL <http://www.ncbi.nlm.nih.gov/pubmed/24785326><http://thejns.org/doi/10.3171/2014.3.JNS121312>.
- [155] Songbai Ji and Susan S. Margulies. In vivo pons motion within the skull. *Journal of Biomechanics*, 40(1):92–99, 2007. ISSN 00219290. doi: 10.1016/j.jbiomech.2005.11.009.
- [156] Satoshi Tsutsumi, Hideo Ono, and Yukimasa Yasumoto. Immobile cerebral veins in the context of positional brain shift: an undescribed risk factor for acute subdural hemorrhage. *Surgical and Radiologic Anatomy*, 39(10):1063–1067, 2017. ISSN 12798517. doi: 10.1007/s00276-017-1837-8. URL <http://link.springer.com/10.1007/s00276-017-1837-8>.
- [157] Ryuichi Takahashi, Kazunari Ishii, Tatsuya Kakigi, and Kazumasa Yokoyama. Gender and age differences in normal adult human brain: Voxel-based morphometric study. *Human Brain Mapping*, 32(7):1050–1058, 2011. ISSN 10659471. doi: 10.1002/hbm.21088.
- [158] Karol Miller and Kiyoyuki Chinzei. Mechanical properties of brain tissue in tension. *Journal of Biomechanics*, 35(4):483–490, 2002. ISSN 00219290. doi: 10.1016/S0021-9290(01)00234-2.
- [159] F. Velardi, F. Fraternali, and M. Angelillo. Anisotropic constitutive equations and experimental tensile behavior of brain tissue. *Biomechanics and Modeling in Mechanobiology*, 5(1):53–61, 2006. ISSN 16177959. doi: 10.1007/s10237-005-0007-9.
- [160] Karol Miller and Kiyoyuki Chinzei. Constitutive modelling of brain tissue: Experiment and theory. *Journal of Biomechanics*, 30(11-12):1115–1121, 1997. ISSN 00219290. doi: 10.1016/S0021-9290(97)00092-4.
- [161] S. Budday, G. Sommer, C. Birkl, C. Langkammer, J. Haybaeck, J. Kohnert, M. Bauer, F. Paulsen, P. Steinmann, E. Kuhl, and G. A. Holzapfel. Mechanical characterization of human brain tissue. *Acta Biomaterialia*, 48:319–340, 2017. ISSN 18787568. doi: 10.1016/j.actbio.2016.10.036. URL <http://dx.doi.org/10.1016/j.actbio.2016.10.036>.
- [162] V. Libertiaux, F. Pascon, and S. Cescotto. Experimental verification of brain tissue incompressibility using digital image correlation. *Journal of the Mechanical Behavior of Biomedical Materials*, 4(7):1177–1185, 2011. ISSN 17516161. doi: 10.1016/j.jmbbm.2011.03.028. URL <http://dx.doi.org/10.1016/j.jmbbm.2011.03.028>.
- [163] G. Franceschini, D. Bigoni, P. Regitnig, and G. A. Holzapfel. Brain tissue deforms similarly to filled elastomers and follows consolidation theory. *Journal of the*

- Mechanics and Physics of Solids*, 54(12):2592–2620, 2006. ISSN 00225096. doi: 10.1016/j.jmps.2006.05.004.
- [164] Adam Wittek, Trent Hawkins, and Karol Miller. On the unimportance of constitutive models in computing brain deformation for image-guided surgery. *Bio-mechanics and Modeling in Mechanobiology*, 8(1):77–84, 2009. ISSN 16177959. doi: 10.1007/s10237-008-0118-1.
- [165] Naftali Raz, Faith M. Gunning, Denise Head, James H. Dupuis, John McQuain, Susan D. Briggs, Wendy J. Loken, Allen E. Thornton, and James D. Acker. Selective aging of the human cerebral cortex observed in Vivo: Differential vulnerability of the prefrontal gray matter. *Cerebral Cortex*, 7(3):268–282, 1997. ISSN 10473211. doi: 10.1093/cercor/7.3.268. URL <http://www.ncbi.nlm.nih.gov/pubmed/9143446>.
- [166] Arthur W. Toga and Paul M. Thompson. Mapping brain asymmetry. *Nature Reviews Neuroscience*, 4(1):37–48, 2003. ISSN 14710048. doi: 10.1038/nrn1009.
- [167] Amit Gefen. How much time does it take to get a pressure ulcer? Integrated evidence from human, animal, and in vitro studies. *Ostomy Wound Management*, 54(10), 2008. ISSN 08895899.
- [168] Tal Zeevi, Ayelet Levy, Neima Brauner, and Amit Gefen. Effects of ambient conditions on the risk of pressure injuries in bedridden patients—multi-physics modelling of microclimate. *International Wound Journal*, 15(3):402–416, 2018. ISSN 1742481X. doi: 10.1111/iwj.12877.
- [169] David Brienza, Jaxon Vallely, Patricia Karg, Jonathan Akins, and Amit Gefen. An MRI investigation of the effects of user anatomy and wheelchair cushion type on tissue deformation. *Journal of Tissue Viability*, 27(1):42–53, 2018. ISSN 18764746. doi: 10.1016/j.jtv.2017.04.001. URL <https://doi.org/10.1016/j.jtv.2017.04.001>.
- [170] Carol Bartley and Melanie Stephens. Development of pressure ulcers when sitting. *Wounds UK*, 15(1):34–39, 2019. ISSN 17466814. doi: 10.17866/rd.salford.7958873.
- [171] Jacqui Fletcher, Helen Crook, and Ceri Harris. Monitoring pressure ulcer prevalence: A precise methodology. *Wounds UK*, 9(4):48–53, 2013. ISSN 17466814.
- [172] Dafna Schwartz and Amit Gefen. The biomechanical protective effects of a treatment dressing on the soft tissues surrounding a non-offloaded sacral pressure ulcer. *International Wound Journal*, 16(3):684–695, 2019. ISSN 1742481X. doi: 10.1111/iwj.13082.
- [173] Joyce M. Black, Christopher T. Brindle, and Jeremy S. Honaker. Differential diagnosis of suspected deep tissue injury. *International Wound Journal*, 13(4): 531–539, 2016. ISSN 1742481X. doi: 10.1111/iwj.12471.

- [174] Jacqui Fletcher, Dan Bader, Fiona Downie, Caroline Dowsett, Jeanette Milne, Karen Ousey, and Lisette Schoonhoven. Recognising, managing and preventing deep tissue injury ( DTI ). Technical report, 2017. URL [www.wounds-uk.com](http://www.wounds-uk.com).
- [175] Maggie J. Westby, Jo C. Dumville, Marta O. Soares, Nikki Stubbs, and Gill Norman. Dressings and topical agents for treating pressure ulcers. *Cochrane Database of Systematic Reviews*, 2017(6), 2017. ISSN 1469493X. doi: 10.1002/14651858.CD011947.pub2.
- [176] C. W.J. Oomens, O. F.J.T. Bressers, E. M.H. Bosboom, C. V.C. Bouten, and D. L. Bader. Can loaded interface characteristics influence strain distributions in muscle adjacent to bony prominences? *Computer Methods in Biomechanics and Biomedical Engineering*, 6(3):171–180, 2003. ISSN 10255842. doi: 10.1080/1025584031000121034.
- [177] Joshua S. Mervis and Tania J. Phillips. Pressure ulcers: Prevention and management. *Journal of the American Academy of Dermatology*, 81(4): 893–902, 2019. ISSN 10976787. doi: 10.1016/j.jaad.2018.12.068. URL <https://doi.org/10.1016/j.jaad.2018.12.068>.
- [178] Carlijn V. Bouten, Cees W. Oomens, Frank P. Baaijens, and Daniel L. Bader. The etiology of pressure ulcers: Skin deep or muscle bound? *Archives of Physical Medicine and Rehabilitation*, 84(4):616–619, 2003. ISSN 00039993. doi: 10.1053/apmr.2003.50038.
- [179] Jules L. Nelissen, Willeke A. Traa, Hans H. de Boer, Larry De Graaf, Valentina Mazzoli, C. Dilara Savci-Heijink, Klaas Nicolay, Martijn Froeling, Dan L. Bader, Aart J. Nederveen, Cees W.J. Oomens, and Gustav J. Strijkers. An advanced magnetic resonance imaging perspective on the etiology of deep tissue injury. *Journal of Applied Physiology*, 124(6):1580–1596, 2018. ISSN 15221601. doi: 10.1152/jappphysiol.00891.2017.
- [180] Vincent Luboz, Mathieu Bailet, Christelle Boichon Grivot, Michel Rochette, Bruno Diot, Marek Bucki, and Yohan Payan. Personalized modeling for real-time pressure ulcer prevention in sitting posture. *Journal of Tissue Viability*, 27(1):54–58, 2018. ISSN 18764746. doi: 10.1016/j.jtv.2017.06.002. URL <https://doi.org/10.1016/j.jtv.2017.06.002>.
- [181] Rami M.A. Al-Dirini, Matthew P. Reed, Jingwen Hu, and Dominic Thewlis. Development and Validation of a High Anatomical Fidelity FE Model for the Buttock and Thigh of a Seated Individual. *Annals of Biomedical Engineering*, 44 (9):2805–2816, 2016. ISSN 15739686. doi: 10.1007/s10439-016-1560-3.
- [182] Stéphane Avril, Sam Evans, and Karol Miller. Inverse problems and material identification in tissue biomechanics. *Journal of the Mechanical Behavior of Biomedical Materials*, 27:129–131, 2013. ISSN 17516161. doi: 10.1016/j.jmbbm.2013.07.001.

- [183] Aurélien Macron, Hélène Pillet, Jennifer Doridam, Isabelle Rivals, Mohammad Javad Sadeghinia, Alexandre Verney, and Pierre Yves Rohan. Is a simplified Finite Element model of the gluteus region able to capture the mechanical response of the internal soft tissues under compression? *Clinical Biomechanics*, 71 (October 2019):92–100, 2020. ISSN 18791271. doi: 10.1016/j.clinbiomech.2019.10.005. URL <https://doi.org/10.1016/j.clinbiomech.2019.10.005>.
- [184] Sharon Eve Sonenblum, Stephen H. Sprigle, John Mc Kay Cathcart, and Robert John Winder. 3D anatomy and deformation of the seated buttocks. *Journal of Tissue Viability*, 24(2):51–61, 2015. ISSN 18764746. doi: 10.1016/j.jtv.2015.03.003. URL <http://dx.doi.org/10.1016/j.jtv.2015.03.003>.
- [185] Rami M.A. Al-Dirini, Matthew P. Reed, and Dominic Thewlis. Deformation of the gluteal soft tissues during sitting. *Clinical Biomechanics*, 30(7):662–668, 2015. ISSN 18791271. doi: 10.1016/j.clinbiomech.2015.05.008. URL <http://dx.doi.org/10.1016/j.clinbiomech.2015.05.008>.
- [186] Eran Linder-Ganz, Noga Shabshin, Yacov Itzhak, Ziva Yizhar, Itzhak Siev-Ner, and Amit Gefen. Strains and stresses in sub-dermal tissues of the buttocks are greater in paraplegics than in healthy during sitting. *Journal of Biomechanics*, 41 (3):567–580, 2008. ISSN 00219290. doi: 10.1016/j.jbiomech.2007.10.011.
- [187] Sheng Chen, Justin Scott, Tamara Reid Bush, and Sara Roccabianca. Inverse finite element characterization of the human thigh soft tissue in the seated position. *Biomechanics and Modeling in Mechanobiology*, 19(1):305–316, 2020. ISSN 16177940. doi: 10.1007/s10237-019-01212-7. URL <https://doi.org/10.1007/s10237-019-01212-7>.
- [188] Michael Harry, Russell Marshall, and Michael Fray. Quantification of buttock deformation on a rigid seat. *Advances in Intelligent Systems and Computing*, 975 (July):471–483, 2020. ISSN 21945365. doi: 10.1007/978-3-030-20216-3\_44.
- [189] J. Doridam, A. Macron, C. Vergari, A. Verney, P. Y. Rohan, and H. Pillet. Feasibility of sub-dermal soft tissue deformation assessment using B-mode ultrasound for pressure ulcer prevention. *Journal of Tissue Viability*, 27(4): 238–243, 2018. ISSN 18764746. doi: 10.1016/j.jtv.2018.08.002. URL <https://doi.org/10.1016/j.jtv.2018.08.002>.
- [190] Michael Ebner, Guotai Wang, Wenqi Li, Michael Aertsen, Premal A. Patel, Rosalind Aughwane, Andrew Melbourne, Tom Doel, Steven Dymarkowski, Paolo De Coppi, Anna L. David, Jan Deprest, Sébastien Ourselin, and Tom Vercauteren. An automated framework for localization, segmentation and super-resolution reconstruction of fetal brain MRI. *NeuroImage*, 206(September 2019), 2020. ISSN 10959572. doi: 10.1016/j.neuroimage.2019.116324.



- [191] Stefan Klein and Marius Staring. *elastix: The Manual*. *October*, 2011(6):1–42, 2011. URL [http://www.dante.de/tex-archive/systems/e-tex/v2/doc/etex\\_man.pdf](http://www.dante.de/tex-archive/systems/e-tex/v2/doc/etex_man.pdf).
- [192] Marek Bucki, Vincent Luboz, Antoine Perrier, F Cannard, Bruno Diot, Nichola Vuillerme, and Yohan Payan. Body numerical phantoms for estimating soft tissue pains or injuries when interacting with shoes, seats and mattresses. *HAL, archives-ouvertes.fr*, 2019. URL <https://www.researchgate.net/publication/337480355>.
- [193] Simon Baker and Takeo Kanade. Limits on super-resolution and how to break them. *IEEE Transactions on Pattern Analysis and Machine Intelligence*, 24(9):1167–1183, 2002. ISSN 01628828. doi: 10.1109/TPAMI.2002.1033210.
- [194] Jianchao Yang and Thomas Huang. Image super-resolution: Historical overview and future challenges. *Super-Resolution Imaging*, pages 1–33, 2017. doi: 10.1201/9781439819319.
- [195] Eric Van Reeth, Ivan W.K. Tham, Cher Heng Tan, and Chueh Loo Poh. Super-resolution in magnetic resonance imaging: A review. *Concepts in Magnetic Resonance Part A: Bridging Education and Research*, 40 A(6):306–325, 2012. ISSN 15466086. doi: 10.1002/cmr.a.21249.
- [196] M Unser. Finding a General Mechanism for Switching Between the Continuous and Discrete Signal Domains Is One Of the Fundamental Issues in Signal Processing. *IEEE Signal Processing Magazine*, (NOVEMBER):22–38, 1999.
- [197] Mohsen Makhsous, Dohyung Lim, Ronald Hendrix, James Bankard, William Z. Rymer, and Fang Lin. Finite element analysis for evaluation of pressure ulcer on the buttock: Development and validation. *IEEE Transactions on Neural Systems and Rehabilitation Engineering*, 15(4):517–525, 2007. ISSN 15344320. doi: 10.1109/TNSRE.2007.906967.
- [198] Zachary Sadler, Justin Scott, Joshua Drost, Sheng Chen, Sara Roccabianca, and Tamara Reid Bush. Initial estimation of the in vivo material properties of the seated human buttocks and thighs. *International Journal of Non-Linear Mechanics*, 107(October):77–85, 2018. ISSN 00207462. doi: 10.1016/j.ijnonlinmec.2018.09.007. URL <https://doi.org/10.1016/j.ijnonlinmec.2018.09.007>.
- [199] Kevin M. Moerman, Marc van Vijven, Leandro R. Solis, Eline E. van Haften, Arjan C.Y. Loenen, Vivian K. Mushahwar, and Cees W.J. Oomens. On the importance of 3D, geometrically accurate, and subject-specific finite element analysis for evaluation of in-vivo soft tissue loads. *Computer Methods in Biomechanics and Biomedical Engineering*, 20(5):483–491, 2017. ISSN 14768259. doi: 10.1080/10255842.2016.1250259. URL <http://dx.doi.org/10.1080/10255842.2016.1250259>.

- [200] Ayelet Levy and Amit Gefen. Assessment of the Biomechanical Effects of Prophylactic Sacral Dressings on Tissue Loads: A Computational Modeling Analysis. *Ostomy Wound Management*, 63(10):48–55, 2017. ISSN 19432720. doi: 10.25270/owm.10.4855.
- [201] Ran Sopher, Jane Nixon, Claudia Gorecki, and Amit Gefen. Effects of intramuscular fat infiltration, scarring, and spasticity on the risk for sitting-acquired deep tissue injury in spinal cord injury patients. *Journal of Biomechanical Engineering*, 133(2), 2011. ISSN 01480731. doi: 10.1115/1.4003325.
- [202] C. W.J. Oomens, W. Zenhorst, M. Broek, B. Hemmes, M. Poeze, P. R.G. Brink, and D. L. Bader. A numerical study to analyse the risk for pressure ulcer development on a spine board. *Clinical Biomechanics*, 28(7):736–742, 2013. ISSN 02680033. doi: 10.1016/j.clinbiomech.2013.07.005. URL <http://dx.doi.org/10.1016/j.clinbiomech.2013.07.005>.
- [203] K. K. Ceelen, A. Stekelenburg, S. Loerakker, G. J. Strijkers, D. L. Bader, K. Nicolay, F. P.T. Baaijens, and C. W.J. Oomens. Compression-induced damage and internal tissue strains are related. *Journal of Biomechanics*, 41(16):3399–3404, 2008. ISSN 00219290. doi: 10.1016/j.jbiomech.2008.09.016.
- [204] C. Then, J. Menger, G. Benderoth, M. Alizadeh, T. J. Vogl, F. Hübner, and G. Silber. A method for a mechanical characterisation of human gluteal tissue. *Technology and Health Care*, 15(6):385–398, 2007. ISSN 09287329. doi: 10.3233/thc-2007-15601.
- [205] Mohsen Makhsous, Ganapriya Venkatasubramanian, Aditya Chawla, Yagna Pathak, Michael Priebe, William Z. Rymer, and Fang Lin. Investigation of soft-tissue stiffness alteration in denervated human tissue using an ultrasound indentation system. *Journal of Spinal Cord Medicine*, 31(1):88–96, 2008. ISSN 10790268. doi: 10.1080/10790268.2008.11753987.
- [206] Marc Modat, Gerard R. Ridgway, Zeike A. Taylor, Manja Lehmann, Josephine Barnes, David J. Hawkes, Nick C. Fox, and Sébastien Ourselin. Fast free-form deformation using graphics processing units. *Computer Methods and Programs in Biomedicine*, 98(3):278–284, jun 2010. ISSN 01692607. doi: 10.1016/j.cmpb.2009.09.002.
- [207] Ingolf Sack, Kaspar Josche Streitberger, Dagmar Krefting, Friedemann Paul, and Jürgen Braun. The influence of physiological aging and atrophy on brain viscoelastic properties in humans. *PLoS ONE*, 6(9), 2011. ISSN 19326203. doi: 10.1371/journal.pone.0023451.
- [208] Lucy V. Hiscox, Curtis L. Johnson, Matthew D.J. McGarry, Michael Perrins, Aimee Littlejohn, Edwin J.R. van Beek, Neil Roberts, and John M. Starr. High-resolution magnetic resonance elastography reveals differences in subcortical

- gray matter viscoelasticity between young and healthy older adults. *Neurobiology of Aging*, 65:158–167, 2018. ISSN 15581497. doi: 10.1016/j.neurobiolaging.2018.01.010. URL <https://doi.org/10.1016/j.neurobiolaging.2018.01.010>.
- [209] J. Donald Tournier, Fernando Calamante, David G. Gadian, and Alan Connelly. Direct estimation of the fiber orientation density function from diffusion-weighted MRI data using spherical deconvolution. *NeuroImage*, 23(3):1176–1185, 2004. ISSN 10538119. doi: 10.1016/j.neuroimage.2004.07.037.
- [210] Daniel C. Alexander, Tim B. Dyrby, Markus Nilsson, and Hui Zhang. Imaging brain microstructure with diffusion MRI: practicality and applications. *NMR in Biomedicine*, 32(4):1–26, 2019. ISSN 10991492. doi: 10.1002/nbm.3841.